August 2021

Developing Effective Theories: A Case Study in Monolayer Iron Selenide

Joseph O'Halloran
University of Wisconsin-Milwaukee

DEVELOPING EFFECTIVE THEORIES: A CASE STUDY IN MONOLAYER IRON SELENIDE

by

Joseph O'Halloran

A Dissertation Submitted in
Partial Fulfillment of the
Requirements for the Degree of

Doctor of Philosophy
in Physics

at
The University of Wisconsin-Milwaukee
August 2021

ABSTRACT

DEVELOPING EFFECTIVE THEORIES:
A CASE STUDY IN MONOLAYER IRON SELENIDE
by
Joseph O'Halloran
The University of Wisconsin-Milwaukee, 2021
Under the Supervision of Professor Daniel Agterberg

In this work, we outline the development of a series of models which have allowed us to investigate the low-temperature phases of monolayer FeSe. These models are built using group theoretic arguments to ensure the constraints provided by the crystal symmetry are satisfied. We investigate the interplay between stripe antiferromagnetism and spin-vortex crystal order in the framework of the Landau theory of phase transitions. By considering inversion symmetry breaking terms in the Landau free-energy, we show that the spin-vortex crystal is preferred when the non-symmorphic parent symmetry group $P4/nmm$ is reduced to a symmorphic subgroup.

We also consider symmetry constraints to develop a ten-orbital tight-binding model for monolayer FeSe. We observe that, following a renormalization of the d_{XY} bands, an inversion of the states near the M-point gives rise to a well-separated pair of electron pockets—in accordance with experiment—and allows a simplified two-band model to capture the dynamics of the bands which cross the Fermi energy. Such a model is constructed by considering the irreducible representations for the states identified in the tight binding model.

Finally, we classify the superconducting orders according to their symmetry character. We find that gaps belonging to the A_{1g} and B_{2g} representations each support nodeless superconductivity, despite the latter being a d-wave order. Using a model for antiferromagnetic spin interactions, we also show that the leading order (without spin-orbit coupling) is the B_{2g} order. Additionally, our model for the B_{2g} order produces a nodeless, anisotropic gap, with multiple coherence peaks in the density of states, in accordance to what is observed in experiment.

TABLE OF CONTENTS

LIST OF FIGURES

LIST OF TABLES

Chapter 1

INTRODUCTION

Superconductivity was first recognized by Onnes [1] by the precipitous drop in resistivity for Mercury when cooled to 4.2 K—known as the superconducting critical temperature. Subsequent investigation by Meissner and Oschenfeld [2] determined that the superconducting transition was also accompanied by a diamagnetic response (the expulsion of magnetic field). The diamagnetic response of superconductors differentiates them from an ideal (or perfect) conductor; an ideal conductor provides a diamagnetic response to oppose a changing magnetic field, while a superconductor will expel even a static magnetic field.

A microscopic description of superconductivity was put forward by Bardeen, Cooper, and Schrieffer (BCS) [3, 4], which describes superconductivity as arising from pairs of electrons, known as Cooper pairs [5], that are bound together by a weakly-attractive phonon-mediated interaction. This pairing interaction forms Cooper pairs from electron states which are time-reversed partners of one another and is unstable to magnetic interactions, as magnetic interactions lift the Kramers degeneracy between time-reversed partners. The phonon interaction described by Bardeen, Cooper, and Schrieffer is isotropic in momentum space and opens a constant gap above the normal state Fermi-surface, which is observed in measurements of the density-of-states as a characteristic 'U' shape. The superconducting gap also exhibits backbending—the superconducting bands approach the normal state Fermi surface before bending away from it. The conventional theory of superconductivity by Bardeen, Cooper, and Schrieffer also makes specific predictions about the size of the superconducting gap in relation to the critical temperature: $\Delta(T = 0) = 1.764 k_b T_c$, when the gap is measured at zero temperature.

There has long been interest in other, unconventional, pairing mechanisms for superconductivity. Kohn and Luttinger [6] showed that the screened Coulomb interaction can have an attractive component when decomposed into spherical harmonics on the Fermi surface. For this reason, the pairing symmetry is often categorized with the same labels as atomic orbitals, with s-wave describing an isotropic pairing interaction, as in the conventional case from phonon-mediated pairing, p-wave describing a pairing interaction which changes sign under a two-fold rotation, d-wave describing a pairing interaction which changes sign under a four-fold rotation, etc.. It is well known that the higher-order spherical harmonics contain nodes, which in turn results in "gapless" superconductivity, which has a characteristic 'V' shape in the density-of-states. The spherical harmonics provide a good basis for a free electron with an unconstrained spin, but if further constraints are imposed by a crystal field or spin-orbit coupling, separate spherical harmonics can no longer be distinguished, which can permit a pairing interaction which contains many components [7].

The theoretical interest in unconventional superconductivity was strengthened by the discovery of superconductivity in the cuprates [8]. A standout feature for the cuprates is a higher-than-expected superconducting critical temperature. Measurements of the density-of-states in the cuprates the characteristic 'V' shape of gapless superconductivity. Later, it was shown that the cuprates are d-wave superconductors [9, 10, 11] via flux quantization measurements in superconducting rings; phase differences in the superconducting gap function around a ring can manifest as spontaneously generated flux. Curiously, the normal state for the cuprates is a Mott insulator, rather than metallic. Thus, the cuprates exhibit a Fermi surface which can be unstable to superconductivity, but also feature antiferromagnetic interactions which generally compete with superconductivity. It is thought that these antiferromagnetic interactions could provide the pairing interaction for cuprates, although this has not been shown to be the case.

The iron-based superconductors that we study here appear to have much in common with the cuprate superconductors—including proximity to a Mott insulating phase—but also carry a distinguishing feature. Conventional superconductors, and even some unconventional superconductors such as the cuprates, have a single Fermi surface in the Brillouin zone. Even the simplest iron-based superconductors, however, have multiple Fermi surfaces. This allows for a superconducting interaction between not only electrons on the same Fermi surface—intraband pairing—but between electrons on different Fermi surfaces as well—interband pairing. The superconducting

gap, in contrast with the cuprates, appears to be nodeless [12, 13, 14, 15, 16, 17, 18], and multiple features in the superconducting density of states have been observed as well [19, 20, 21]. In this work, we show that, as a consequence of this additional interband pairing, a nodeless gap and multiple features in the density-of-states are supported by both s-wave and d-wave symmetries, contrary to what is expected for single-band superconductors.

1.1 IRON-BASED SUPERCONDUCTORS

Superconductivity has been observed in a number of iron-based systems, including the ferropnictides such as the '1111' family (*e.g.* LaOFeAs, SmOFeAs, PrOFeAs), the '122' family (*e.g* $BaFe_2As_2$, $SrFe_2As_2$, $CaFe_2As_2$), the '111' family (*e.g.* LiFeAs, NaFeAs, PFeAs) [22, 23]; typically, these systems require some level of doping to exhibit superconductivity, which is accomplished via chemical substitution such as $Ba_{1-x}K_xFe_2As_2$. In this work we are focused primarily on FeSe, which is an iron-chalcogenide. The common feature among the iron-based superconductors is the structural unit consisting of iron and either a pnictogen (group XV elements, *e.g.* As) or chalcogen (group XVI elements, *e.g.* Se); FeSe forms in stacks of essentially two-dimensional sheets (monolayers) while, in ferropnictides, the FeAs layers are intercalated by the various other elements in the compound. Our primary interest is in substrate-supported monolayer FeSe, particularly because when compared to bulk FeSe, the monolayer exhibits a marked and unexpected increase in superconducting critical temperature from $\sim 27\,\mathrm{K}$ in the bulk to over $63\,\mathrm{K}$ for the monolayer [24, 25, 26, 27].

As with the cuprates, the iron-based superconductors exhibit a rich phase diagram in temperature, doping, and pressure [28, 29, 22, 30, 23], although we shall focus on ambient pressures (which includes high-vacuum). Here, doping refers to the number of excess electrons per iron atom. With little to no doping, many of the iron-based superconductors exhibit an antiferromagnetic spin-density wave (SDW) ground state. This spin-density wave can be viewed as having magnetic moments on the iron atoms which align ferromagnetically along one direction, but antiferromagnetically along the perpendicular direction, which forms a series of magnetic "stripes". We will discuss magnetism in the iron-based superconductors more in chapter 3, although we should mention that for FeSe, which we study, there does not appear to be any magnetic order at low temperatures.

In addition to the antiferromagnetic order observed in many iron-based superconductors, super-

conductivity is also observed at low temperatures for a range of doping. In some systems, there appears to be an overlap between the superconducting region and the antiferromagnetic order. As magnetic interactions typically suppress superconductivity, these regions of overlap are viewed as evidence that the antiferromagnetic interaction plays a role in the pairing interaction, although this is not conclusive.

There are, additionally, structural transitions that occur in many iron-based superconductors which occur in proximity to the spin-density wave. The nature of these different phases remains contested, but it is speculated that these phases are interrelated. Our work does not investigate the structural transition.

1.2 SPACE GROUP SYMMETRY

Monolayer FeSe consists of a single plane of iron atoms arranged in a square lattice with a nearest neighbor iron-iron distance of $\sim 2.668\,\text{Å}$; in the middle of each square of iron atoms a selenium atom sits offset above or below the iron plane; the selenium height above (or below) the iron plane is $0.2672(1)\,\text{Å}$. The selenium alternate above and below the iron plane, forming an egg-crate pattern. Due to this alternating pattern of inequivalent selenium sites, the overall chemical unit cell has two iron sites and two selenium sites and is tetragonal with side lengths $a = 3.7734(1)\,\text{Å}$ and $c = 5.5258(1)\,\text{Å}$ [31]. Figure 1.1 depicts the crystal structure and the unit cell for FeSe. Also used throughout this work is the coordinate system laid out in fig. 1.1. The $\widehat{\boldsymbol{x}}$ and $\widehat{\boldsymbol{y}}$ (primary) directions align with the periodicity of the lattice, so that a lattice vector can be written $(m\,n) = a(m\widehat{\boldsymbol{x}} + n\widehat{\boldsymbol{y}})$. For the remainder of this work, we (mostly) use non-dimensional coordinates where $a = 1\,\text{unit}$. The iron-iron nearest neighbor directions, which run diagonal to the x- and y- axes, are also prominent and we specify them as well: $\widehat{\boldsymbol{X}} = (\widehat{\boldsymbol{x}} + \widehat{\boldsymbol{y}})/\sqrt{2}$ and $\widehat{\boldsymbol{Y}} = (-\widehat{\boldsymbol{x}} + \widehat{\boldsymbol{y}})/\sqrt{2}$. The two-dimensional Brillouin zone for FeSe, with points and lines of high-symmetry, is also depicted. Some authors will work with a one-iron unit cell, which is rotated 45° compared to our choice of axes; the primary axes in that case are equivalent to what we take as the $\widehat{\boldsymbol{X}}$ and $\widehat{\boldsymbol{Y}}$ directions.

FeSe belongs to the space group $P4/nmm$, which we will also simply call $\mathcal{G}$. The parent point group for $P4/nmm$ is D_{4h}, which can be generated by three elements. We take these to be inversion (denoted $\overline{1}$) a mirror plane perpendicular to $\widehat{\boldsymbol{Y}}$ (denoted $m_{\overline{1}10}$) and a mirror plane perpendicular to

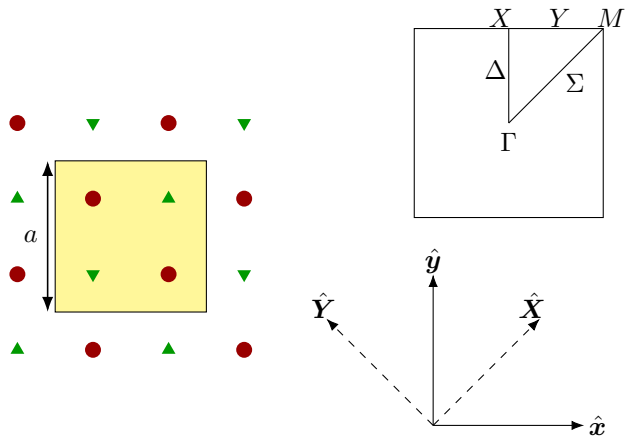

Figure 1.1: The two dimensional crystal structure of FeSe (viewed from above). The "egg-crate" structure consists of a central plane of Fe (red, circles) atoms, puckered by Se above (green, upward triangles) and below (green, downward triangles). The lattice constant for the 2-Fe unit cell is $a = 3.7734(1)\,\text{Å}$. In this work, we take our unit cell (highlighted) to be centered on an inversion site, with the iron atoms located at $(\pm\frac{a}{4}, \mp\frac{a}{4}, 0)$ (that is, the origin is the center of the unit cell). In the upper-right is the two-dimensional Brillouin zone highlighting points and lines of high symmetry; in the lower-right we define the directions of our coordinate system.

$\widehat{\boldsymbol{y}}$ (denoted m_{010}). The full space group $\mathcal{G}$ is generated by specific instances of these point group operations as applied to the crystal structure, which is shown in fig. 1.2.

Space groups are subgroups of the semidirect product $P \ltimes \mathcal{T}$, where P is some point group—D_{4h} for the case of $P4/nmm$—and $\mathcal{T}$ is the set of translations in $\mathbb{R}^3$. Seitz notation is used to reflect this relationship, where we write the ordered pair $\{g|\boldsymbol{u}\}$ where $g \in P$ is a point group operation and $\boldsymbol{u} \in \mathcal{T}$ is a translation in real space. The multiplication rule for two elements of $P \ltimes \mathcal{T}$ follows from the standard definition of a semidirect product space,

$$\{g|\boldsymbol{u}\} \cdot \{h|\boldsymbol{v}\} = \{gh|\boldsymbol{u} + g\boldsymbol{v}\}\,,$$

where $g\boldsymbol{v}$ is a shorthand for the action of the element g applied to the translation vector $\boldsymbol{v}$. Because we are describing a physical object and not an abstract space, the action of g is given by our intuitive understanding of how symmetry operations transform Euclidean space, which the vectors $\boldsymbol{v}$ are elements of.

Using Seitz notation, we can express the generators for $P4/nmm$ as $\{\bar{1}|0\,0\}$, $\{m_{1\bar{1}0}|0\,0\}$, and $\{m_{010}|0\,\frac{1}{2}\}$. Conventionally, the translation is written in component form, so that $(0\,\frac{1}{2})$ here means no translation along the $\widehat{\boldsymbol{x}}$ direction and a translation through half the unit cell along the $\widehat{\boldsymbol{y}}$ direction.

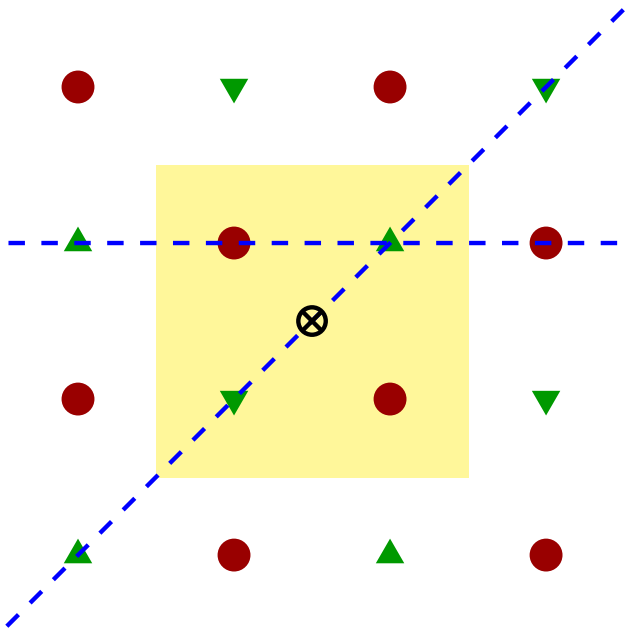

Figure 1.2: Three symmetry operations are all that are required to generate $P4/nmm$. We have the freedom to choose these to be a mirror plane perpendicular to $\widehat{\boldsymbol{y}}$, a mirror plane perpendicular to $\widehat{\boldsymbol{Y}}$, and an inversion through a point half-way between two iron atoms (marked by $\otimes$).

For this set of generators, $\{m_{010}|0\,\frac{1}{2}\}$ contains a fractional translation element. This is a result of our choice of origin, which we take to coincide with the center of inversion. Symmetry transformations such as rotations and reflections leave a point or set of points fixed. In a point group, the intersection of the set of fixed points for all of the transformations of the group is non-empty, which gives a natural choice for the origin of a point group; this is the "point" in point groups. For space groups, this is no longer the case.

Space groups can be divided into symmorphic or non-symmorphic varieties. A symmorphic space group is one where the representatives for every element of the parent point group P can be chosen to all share a common fixed point. Symmorphic space groups take the form $P \ltimes T$, where T is the set of lattice translations (as opposed to $\mathcal{T}$, the set of all translations). When this cannot be done, the space group is non-symmorphic. The space group which describes the crystal structure for FeSe, $P4/nmm$, is non-symmorphic. As such, there is no natural choice of origin, and different sources make different choices for their origin. We choose our origin to coincide with the center of inversion, and so elements, such as the mirror plane m_{010}, which do not contain the origin acquire fractional translation elements.

Because the selenium atoms alternate above and below the iron plane, there is additionally the

$\{1\|0\,0\}$	$\{m_{100}\|\frac{1}{2}\,0\}$	$\{m_{010}\|0\,\frac{1}{2}\}$	$\{m_{001}\|\frac{1}{2}\,\frac{1}{2}\}$
$\{\bar{1}\|0\,0\}$	$\{2_{100}\|\frac{1}{2}\,0\}$	$\{2_{010}\|0\,\frac{1}{2}\}$	$\{2_{001}\|\frac{1}{2}\,\frac{1}{2}\}$
$\{m_{1\bar{1}0}\|0\,0\}$	$\{4^+_{001}\|\frac{1}{2}\,0\}$	$\{4^-_{001}\|0\,\frac{1}{2}\}$	$\{m_{110}\|\frac{1}{2}\,\frac{1}{2}\}$
$\{2_{1\bar{1}0}\|0\,0\}$	$\{\bar{4}^+_{001}\|\frac{1}{2}\,0\}$	$\{\bar{4}^-_{001}\|0\,\frac{1}{2}\}$	$\{2_{110}\|\frac{1}{2}\,\frac{1}{2}\}$

Table 1.1: Coset representatives for $P4/nmm$ with the choice of origin at the inversion center.

symmetry element $\{m_{001}|\frac{1}{2}\,\frac{1}{2}\}$, which is known as a glide plane. This mirror plane is different to $\{m_{010}|0\,\frac{1}{2}\}$ because the translation element for the latter is perpendicular to the mirror plane, while for $\{m_{001}|\frac{1}{2}\,\frac{1}{2}\}$ the translation is in the mirror plane, so that $\{m_{001}|\frac{1}{2}\,\frac{1}{2}\}$ leaves no fixed points. Because of this, the translational element in this case is not due to our choice of origin, but is instead an essential feature of $P4/nmm$. We do not include it as a generator because this glide plane is generated by the elements chosen, but some authors will take $\{m_{001}|\frac{1}{2}\,\frac{1}{2}\}$ as a generator, typically replacing inversion.

The space group $\mathcal{G}$ also includes translation elements of the form $\{1|\boldsymbol{t}\} \in T$, where $\boldsymbol{t}$ is some lattice vector. The translation group is a normal subgroup of the space group, $T \triangleleft \mathcal{G}$, which allows us to decompose $\mathcal{G}$ into cosets. We can write

$$\mathcal{G} = \bigcup_i \{g_i|\boldsymbol{u}_i\}T\,,$$

where $\{g_i|\boldsymbol{u}_i\}$ is a particular coset representative. For concreteness, the particular coset representatives given our choice of origin are given in table 1.1. For any space group, the quotient group $\mathcal{G}/T \simeq P$ is isomorphic to the parent space group. However, another distinguishing feature for symmorphic groups is that the set of the coset representatives $\{\{g_i|\boldsymbol{u}_i\}\}$ is itself a subgroup of $\mathcal{G}$, which is isomorphic to P. However, this is not the case for non-symmorphic groups. Consider for example, the elements $\{\bar{1}|0\,0\}$ and $\{m_{010}|0\,\frac{1}{2}\}$. We observe

$$\begin{aligned}\{m_{010}|0\,\tfrac{1}{2}\}\{\bar{1}|0\,0\} &= \{2_{010}|0\,\tfrac{1}{2}\}\\ \{\bar{1}|0\,0\}\{m_{010}|0\,\tfrac{1}{2}\} &= \{2_{010}|0\,\overline{\tfrac{1}{2}}\}\,.\end{aligned}$$

Because $\{2_{010}|0\,\overline{\frac{1}{2}}\}$ is not in the set of coset representatives, it is clear that the coset representatives do not form a group. However, in the quotient $\mathcal{G}/T$, $\{2_{010}|0\,\overline{\frac{1}{2}}\} \sim \{2_{010}|0\,\frac{1}{2}\}$ because they differ by

only an element of T, namely $\{1|0\,1\}$. As a final note about notation, the overline, $\overline{}$, is somewhat overloaded, but generally indicates some sort of inversion. In $\{\overline{1}|0\,0\}$, $\overline{1}$ refers specifically to inversion as a symmetry operation. In $\{2_{010}|0\,\frac{\overline{1}}{2}\}$, $\frac{\overline{1}}{2}$ refers to the additive inverse, $-\frac{1}{2}$. For an abstract group element g, $\overline{g}$ is the inverse of g.

1.3 OUTLINE

In the next few chapters, we will present the work that has been done in developing and evaluating models to describe various aspects of interest in FeSe. We begin with a discussion of the global properties of FeSe in chapter 2. We develop a tight-binding model using the crystal symmetries outlined above and following the work of Eschrig and Koepernik [32]. The band structure for monolayer FeSe differs from the bulk particularly near the Fermi energy, where the bands for d_{XY} orbitals and d_{Xz}/d_{Yz} orbitals are renormalized from their bulk values. The tight-binding model which we develop for the monolayer was developed to investigate this renormalization.

One consequence of this renormalization is a band inversion near the M-point, which hints at a possible topological transition. The remainder of chapter 2 is therefore devoted to exploring this possibility. We discuss the method of topological quantum chemistry [33] as it applies to the particular case of FeSe and give an intuitive description of the elementary band representations developed for this method. Using elementary band representations, we argue that the band inversion observed in the transition from the bulk to the monolayer is, in fact, topological, and that the band structure for monolayer FeSe is topologically non-trivial, while the band structure for the bulk is trivial.

In chapter 3 we turn our attention to antiferromagnetism in iron-based superconductors. As part of earlier work [34], we investigated the role that breaking inversion symmetry plays in antiferromagnetic ordering. This investigation is motivated by the fact that inversion symmetry is broken for substrate supported monolayer FeSe. We show, using group theoretic arguments, that the stripe phases which are present in many iron-based superconductors become unstable when the symmetry of $P4/nmm$ is reduced to a symmorphic subgroup, and that, instead, a spin-vortex crystal is favored. We proceed then to use Landau theory to examine the phase diagram.

Finally, we focus on superconductivity in chapters 4 and 5. First, in chapter 4, we present a

development of a low-energy effective Hamiltonian which is meant to approximate the normal state near the Fermi energy. As a consequence of the band-inversion which we discuss in chapter 2, we derive a continuum model which arises from a single representation at the M-point. We present two different approaches to the derivation which mutually agree. This model for the normal state is necessary for the description of superconductivity which follows.

Chapter 5 presents the actual consideration of the superconducting pairing interaction. We begin by categorizing the symmetries of different pairing interactions. Owing to the multiband nature of FeSe, we observe that the momentum space dependence of the gap function becomes much richer than in the single band case. We then present an analysis of an antiferromagnetic pairing interaction, which we find is attractive for a d-wave pairing channel but also for an s-wave pairing channel, again as a consequence of the multiband physics. Finally, we consider the quasiparticle dispersion for the s-wave and the d-wave states. In both instances we are able to replicate a fully-gapped superconducting state which exhibits multiple gap features in the density-of-states.

Also included are a pair of appendices meant to introduce the unfamiliar reader with group theory and representation theory. Appendix A deals with finite groups, with a focus on the point group D_{4h}, while appendix B deals with space groups, with a focus on $P4/nmm$.

Chapter 2

BAND STRUCTURE

Electronic properties in crystalline solids are understood in terms of the band structure, which provides a natural starting point for discussion. The band structure provides a global description of electronic behavior which we approximate with a tight-binding model developed following the work of Eschrig and Koepernik[32]. While the tight-binding model provides reasonable accuracy, it is at the expense of a considerably larger parameter space. For this reason, when we look at superconductivity, which involves primarily states near the Fermi energy, we will use instead an effective Hamiltonian which provides reasonable agreement in the vicinity of the Fermi energy.

Some previous tight-binding models [35, 36] have been developed using only five d-orbitals by considering a reduced unit cell that contains only one iron atom. While this makes calculations simpler, such models must employ Brillouin zone folding to reproduce results seen from the stoichiometric unit cell containing two iron atoms. However, these models do make clear that all five iron d-orbitals must be considered due to the proximity of their bands to the Fermi energy, as well as the degree of interaction between each band. Contributions from the p-orbitals of selenium are typically far from the Fermi energy and therefore do not need to be directly considered. Rather than using a five-orbital model, we choose instead to follow other authors [32, 37, 35, 38] in using a ten-orbital model which respects the stoichiometry of the unit cell. Equivalence between these two approaches is guaranteed[39] by the glide plane $\{m_{001}|\frac{1}{2}\,\frac{1}{2}\}$, but we find the latter better suited to symmetry analysis in terms of representations of $P4/nmm$. The tight-binding model we employ also does not take spin-orbit coupling into consideration. We are able to get reasonable agreement with observed band structures without including spin-orbit coupling at this stage, although it shall

later become important.

The tight-binding model developed by Eschrig and Koepernik attempts to replicate the band structure observed in bulk FeSe. The key features that are of interest for superconductivity are the hole pockets near the Γ-point and the electron pockets near the M–point, which their model replicates well. However, in monolayer FeSe a renormalization of the d_{XY}, d_{Xz} and d_{Yz} bands reduces their overall bandwidth, lowering the hole pockets near the Γ-point below the Fermi energy, and raising the electron pockets near the M-point. This renormalization is strongly orbital-selective, affecting the d_{XY} band to a greater extent; this inverts the order of the bands comprising the electron pockets near the M-point[40, 41]. In section 2.1, we discuss the development of the tight-binding model, and modify the model to capture the renormalization observed in monolayer FeSe.

Because the monolayer has a band inversion compared to the bulk near the M-point, we are also interested in possible topological properties that might result—band inversion is a necessary, but not sufficient, condition for topological transitions. Topological states were first identified with the discovery of the quantum Hall effect[42], whereby the Hall resistance in a two-dimensional electron gas becomes quantized; it was later shown that this quantization is a type of topological invariant resulting from gauge symmetry[43, 44].

Topological systems are classified by various topological invariants, which can be identified and calculated in various ways[45, 46]. Unfortunately, this method of classification is only able to identify topologically non-trivial systems which fit into one of the previously determined categories. To identify topological materials which do not belong to existing classifications, typically a new invariant must first be determined, because a material which is trivial according to established categories may yet be non-trivial. In contrast, the approach of topological quantum chemistry [33, 47], provides a method to determine whether a given band structure is topologically non-trivial, without first needing to identify the topological invariant to look for. By using this approach, we are able to identify topological band structures for further study and avoid searching for topological invariants in trivial systems.

In section 2.2, we shall apply the method of topological quantum chemistry to the case of monolayer FeSe, using our tight-binding model for the band structure. We demonstrate the derivation of the elementary band representations for $P4/nmm$, and show that the tight binding model for bulk FeSe from [32] provides a topologically trivial band structure while the tight-binding

model for the monolayer provides a topologically non-trivial band structure.

2.1 TIGHT-BINDING MODEL

For our tight binding model, we begin by assuming that the electrons inhabit Wannier functions which are localized to some degree at the iron-sites—the degree of localization is determined by the extent of the overlap between n^{th} nearest neighbors. We shall first expand the Hamiltonian in a basis of definite orbital symmetry; because there are two iron-sites per unit cell and five d-orbitals contributed by the valence shell of each iron, we have ten orbitals per unit cell in our basis. Following Eschrig and Koepernik[32], we take our basis to be the following:

$$\begin{aligned}
1 &: d^A_{XY} & 6 &: d^B_{XY} \\
2 &: d^A_{X^2-Y^2} & 7 &: d^B_{X^2-Y^2} \\
3 &: -id^A_{Yz} & 8 &: +id^B_{Yz} \\
4 &: +id^A_{Xz} & 9 &: -id^B_{Xz} \\
5 &: d^A_{3z^2-r^2} & 10 &: d^B_{3z^2-r^2}
\end{aligned} \tag{2.1}$$

That is, a basis vector such as $\boldsymbol{e}_7$, having a 1 in the seventh position and zeros everywhere else, corresponds to an orbital with $X^2 - Y^2$ symmetry at the 'B' site in the unit cell. We shall again note the difference of basis from some of the literature, particularly work done using a one-iron unit cell. Typically in a one-iron unit cell, the x and y axes are chosen to align with the Fe-Fe nearest neighbor directions, which is also done in [32]. In works with the two-iron unit cell, the x and y axes are chosen to align with the nearest neighbor direction between lattice points (*e.g.* the center of the unit cell), which we have done here. However, to aid comparison between this work and others, we are expressing the orbital symmetry in terms of the X and Y axes which coincide with the Fe-Fe nearest neighbor directions. In eq. (2.1) we write d_{XY}, but this is equivalent to $d_{x^2-y^2}$ by the definitions we are using here.

Expanded in the orbital basis, the tight-binding Hamiltonian, in second quantized form, is written

$$H = \sum_{\boldsymbol{R}\boldsymbol{R}'} \sum_{ll'} t_{ll'}(\boldsymbol{\delta}) c^\dagger_{\boldsymbol{R}l} c_{\boldsymbol{R}'l'} \,,$$

where $t_{ll'}(\boldsymbol{\delta})$ is the energy cost for an electron to hop from the l' orbital at the site $\boldsymbol{R}'$ to the l orbital at the site $\boldsymbol{R}$, and the $c^{(\dagger)}$ are the annihilation (creation) operators for electrons. Here, $\boldsymbol{\delta} = \boldsymbol{R} - \boldsymbol{R}'$; a consequence of the translational symmetry of the system is that t depends only on $\boldsymbol{\delta}$. The hopping integrals $t_{ll'}(\boldsymbol{\delta})$ are further constrained by crystal symmetries. Additionally, the Hamiltonian must be Hermitian and time-reversal symmetric. We use Θ for the time-reversal operator. These conditions can be written

$$\begin{aligned} H &= H^\dagger \\ H &= \Theta^{-1} H \Theta \\ H &= \{g|\boldsymbol{\tau}\}^{-1} H \{g|\boldsymbol{\tau}\}\,. \end{aligned} \tag{2.2}$$

The tight-binding Hamiltonian can be solved by translating the problem to reciprocal (momentum) space. Expressed in this basis, the Hamiltonian becomes

$$H = \sum_{\boldsymbol{k}\boldsymbol{\delta}} \sum_{ll'} e^{i\boldsymbol{k}\cdot\boldsymbol{\delta}} t_{ll'}(\boldsymbol{\delta}) c^\dagger_{\boldsymbol{k}l} c_{\boldsymbol{k}l'}\,.$$

and furthermore, we note that the electron operators transform as

$$\begin{aligned} \Theta^{-1} c^{(\dagger)}_{\boldsymbol{k}l} \Theta &= \sum_m U^{(*)}_{lm}(\Theta) c^{(\dagger)}_{-\boldsymbol{k}m} \\ \{g|\boldsymbol{\tau}\}^{-1} c^{(\dagger)}_{\boldsymbol{k}l} \{g|\boldsymbol{\tau}\} &= \sum_m e^{\mp i(g\boldsymbol{k}-\boldsymbol{k})\cdot\boldsymbol{\tau}} U^{(*)}_{lm}(g) c^{(\dagger)}_{g\boldsymbol{k}m}\,. \end{aligned} \tag{2.3}$$

Without spin, $U(\Theta)$ would ordinarily be the identity, but here it is not because we have chosen a complex basis; for $l = 1, 2, 5$ (and $l+5$) $c^*_{\boldsymbol{R}l} = c_{\boldsymbol{R}l}$, while for $l = 3, 4$ (and $l+5$), $c^*_{\boldsymbol{R}l} = -c_{\boldsymbol{R}l}$. The remaining $U(g)$ are determined by orbital symmetries, which will be enumerated momentarily. Applying eq. (2.3) to the symmetry conditions in eq. (2.2) constrains the hopping integrals as

$$\begin{aligned} t(-\boldsymbol{\delta}) &= t^\dagger(\boldsymbol{\delta}) \\ t^*(\boldsymbol{\delta}) &= U(\Theta) t(\boldsymbol{\delta}) U^\dagger(\Theta) \\ t(\overline{g}\boldsymbol{\delta}) &= U(g) t(\boldsymbol{\delta}) U^\dagger(g)\,. \end{aligned} \tag{2.4}$$

Given the basis enumerated in eq. (2.1), we can express the symmetry transformations U as:

$$\begin{aligned} U(\Theta) &= \mathrm{diag}(1,1,-\tau_0,1)\otimes\lambda_0 & U(\bar{1}) &= \mathrm{diag}(1,1,-\tau_0,1)\otimes\lambda_x \\ U(m_{010}) &= \mathrm{diag}(1,-1,\tau_x,1)\otimes\lambda_0 & U(m_{\bar{1}10}) &= \mathrm{diag}(-1,1,\tau_z,1)\otimes\lambda_x \end{aligned} \tag{2.5}$$

where τ_i are Pauli matrices describing the orbital components for d_{Xz} and d_{Yz}, and λ_j are Pauli matrices corresponding to the sub-lattice symmetry of the system; λ_0 if the operation transforms orbitals at an iron-site to orbitals at the same site (up to a lattice vector), λ_x if the operation transforms orbitals at an iron-site to orbitals at the other site in the unit cell (again, up to a lattice vector). Using the τ_i orbital matrices allows us to write the orbital component of the transformation matrix in block diagonal form.

The glide plane symmetry $\{m_{001}|\frac{1}{2}\,\frac{1}{2}\}$ is particularly interesting; since $m_{001}\boldsymbol{\delta} = \boldsymbol{\delta}$, we have $t(\boldsymbol{\delta}) = U(m_{001})t(\boldsymbol{\delta})U(m_{001})$. Expressed in terms of the generators, we find

$$\{m_{001}|\tfrac{1}{2}\,\tfrac{1}{2}\} = \{m_{1\bar{1}0}|0\,0\}\{m_{010}|0\,\tfrac{1}{2}\}\{m_{1\bar{1}0}|0\,0\}\{m_{010}|0\,\tfrac{1}{2}\}\{\bar{1}|0\,0\}\,;$$

it is readily seen, therefore, that $U(m_{001}) = \mathbb{1}\otimes\lambda_x$. If we write $t(\boldsymbol{\delta})$ in block form as

$$t(\boldsymbol{\delta}) = \begin{pmatrix} T_{AA}(\boldsymbol{\delta}) & T_{AB}(\boldsymbol{\delta}) \\ T_{BA}(\boldsymbol{\delta}) & T_{BB}(\boldsymbol{\delta}) \end{pmatrix},$$

then the constraint provided by $\{m_{001}|\frac{1}{2}\,\frac{1}{2}\}$ gives us

$$\begin{aligned} T_{BB}(\boldsymbol{\delta}) =& T_{AA}(\boldsymbol{\delta}) \\ T_{BA}(\boldsymbol{\delta}) =& T_{AB}(\boldsymbol{\delta})\,. \end{aligned}$$

It follows that we can write $t(\boldsymbol{\delta}) = T_{AA}(\boldsymbol{\delta})\otimes\lambda_0 + T_{AB}(\boldsymbol{\delta})\otimes\lambda_x$. While this expression is generally true, note that for a given $\boldsymbol{\delta} = \boldsymbol{R} - \boldsymbol{R}'$ only one or the other of $T_{AA}(\boldsymbol{\delta})$ and $T_{AB}(\boldsymbol{\delta})$ are non-zero. If $\boldsymbol{\delta}$ is a lattice vector, then hopping only occurs within each sublattice and so only the $T_{AA}(\boldsymbol{\delta})$ submatrix is non-zero. However, if $\boldsymbol{\delta}$ is not a lattice vector, then hopping only occurs between each sublattice, and so only the $T_{AB}(\boldsymbol{\delta})$ submatrix is non-zero.

We also note from eq. (2.5) that $U(\Theta)U(\bar{1}) = \mathbb{1} \otimes \lambda_x$ as well, and therefore $t^*(-\boldsymbol{\delta}) = t(\boldsymbol{\delta})$; but from eq. (2.4) we observe that $t^*(-\boldsymbol{\delta}) = t^{\mathrm{T}}(\boldsymbol{\delta})$. This implies not only that $t(\boldsymbol{\delta})$ is symmetric, but that the submatrices $T_{AA}(\boldsymbol{\delta})$ and $T_{AB}(\boldsymbol{\delta})$ are themselves symmetric as well. Then, because $t(\boldsymbol{\delta})$ is symmetric, we also find that $t(-\boldsymbol{\delta}) = t^*(\boldsymbol{\delta})$. If we now consider the effect of time-reversal alone, $t^*(\boldsymbol{\delta}) = U(\Theta)t(\boldsymbol{\delta})U(\Theta)$, we find that each submatrix T has the form

$$T = \begin{pmatrix} t_{11}^{\boldsymbol{\delta}} & t_{12}^{\boldsymbol{\delta}} & it_{13}^{\boldsymbol{\delta}} & it_{14}^{\boldsymbol{\delta}} & t_{15}^{\boldsymbol{\delta}} \\ t_{12}^{\boldsymbol{\delta}} & t_{22}^{\boldsymbol{\delta}} & it_{23}^{\boldsymbol{\delta}} & it_{24}^{\boldsymbol{\delta}} & t_{25}^{\boldsymbol{\delta}} \\ it_{13}^{\boldsymbol{\delta}} & it_{23}^{\boldsymbol{\delta}} & t_{33}^{\boldsymbol{\delta}} & t_{34}^{\boldsymbol{\delta}} & it_{35}^{\boldsymbol{\delta}} \\ it_{14}^{\boldsymbol{\delta}} & it_{24}^{\boldsymbol{\delta}} & t_{34}^{\boldsymbol{\delta}} & t_{44}^{\boldsymbol{\delta}} & it_{45}^{\boldsymbol{\delta}} \\ t_{15}^{\boldsymbol{\delta}} & t_{25}^{\boldsymbol{\delta}} & it_{35}^{\boldsymbol{\delta}} & it_{45}^{\boldsymbol{\delta}} & t_{55}^{\boldsymbol{\delta}} \end{pmatrix},$$

where each t_{ij} is real. This general form obtains when we can place no additional symmetry constraints, as is the case for fourth-nearest-neighbor hopping, where $\boldsymbol{\delta} = \widehat{\boldsymbol{x}} + \widehat{\boldsymbol{X}}$ (and all other such $g\boldsymbol{\delta}$ for $g \in D_{4h}$). Since $\widehat{\boldsymbol{x}} + \widehat{\boldsymbol{X}}$ is not a lattice vector, fourth-nearest-neighbor hopping occurs between sublattices.

We can obtain further restrictions to the general form when $\boldsymbol{\delta} = \boldsymbol{R} - \boldsymbol{R}'$ satisfies certain conditions. We consider three cases:

Case I: $m_{\bar{1}10}\boldsymbol{\delta} = \boldsymbol{\delta}$.
In this case, we have $t(m_{\bar{1}10}\boldsymbol{\delta}) = t(\boldsymbol{\delta})$, or $t(\boldsymbol{\delta}) = U(m_{\bar{1}10})t(\boldsymbol{\delta})U(m_{\bar{1}10})$. Given the block structure of both $t(\boldsymbol{\delta})$ and $U(m_{\bar{1}10})$, we know that the submatrix therefore takes the form

$$T = \begin{pmatrix} t_{11}^{\boldsymbol{\delta}} & & & it_{14}^{\boldsymbol{\delta}} & \\ & t_{22}^{\boldsymbol{\delta}} & it_{23}^{\boldsymbol{\delta}} & & t_{25}^{\boldsymbol{\delta}} \\ & it_{23}^{\boldsymbol{\delta}} & t_{33}^{\boldsymbol{\delta}} & & it_{35}^{\boldsymbol{\delta}} \\ it_{14}^{\boldsymbol{\delta}} & & & t_{44}^{\boldsymbol{\delta}} & \\ & t_{25}^{\boldsymbol{\delta}} & it_{35}^{\boldsymbol{\delta}} & & t_{55}^{\boldsymbol{\delta}} \end{pmatrix}.$$

This case obtains for $\boldsymbol{\delta} = n\widehat{\boldsymbol{X}}$, where n is an integer. For our purposes, this is the case for first-nearest-neighbor hopping ($n = 1$) and third-nearest-neighbor hopping ($n = 2$). Since $\widehat{\boldsymbol{X}}$ is not a lattice vector, nearest-neighbor hopping occurs between sublattices, as might be expected.

Meanwhile, third-nearest neighbor hopping occurs within each sublattice since $2\widehat{\boldsymbol{X}}$ is a lattice vector.

Case II: $m_{010}\boldsymbol{\delta} = \boldsymbol{\delta}$.

In this case, we have $t(m_{010}\boldsymbol{\delta}) = t(\boldsymbol{\delta})$, or $t(\boldsymbol{\delta}) = U(m_{010})t(\boldsymbol{\delta})U(m_{010})$. Given the block structure of both $t(\boldsymbol{\delta})$ and $U(m_{010})$, we know that the submatrix therefore takes the form

$$T = \begin{pmatrix} t^{\boldsymbol{\delta}}_{11} & & it^{\boldsymbol{\delta}}_{13} & it^{\boldsymbol{\delta}}_{13} & t^{\boldsymbol{\delta}}_{15} \\ & t^{\boldsymbol{\delta}}_{22} & it^{\boldsymbol{\delta}}_{23} & -it^{\boldsymbol{\delta}}_{23} & \\ it^{\boldsymbol{\delta}}_{13} & it^{\boldsymbol{\delta}}_{23} & t^{\boldsymbol{\delta}}_{33} & t^{\boldsymbol{\delta}}_{34} & it^{\boldsymbol{\delta}}_{35} \\ it^{\boldsymbol{\delta}}_{13} & -it^{\boldsymbol{\delta}}_{23} & t^{\boldsymbol{\delta}}_{34} & t^{\boldsymbol{\delta}}_{33} & it^{\boldsymbol{\delta}}_{35} \\ t^{\boldsymbol{\delta}}_{15} & & it^{\boldsymbol{\delta}}_{35} & it^{\boldsymbol{\delta}}_{35} & t^{\boldsymbol{\delta}}_{55} \end{pmatrix}.$$

This case obtains for $\boldsymbol{\delta} = m\widehat{\boldsymbol{x}}$, where m is an integer. For our purpose, this is the case for second-nearest-neighbor hopping ($m = 1$) and for fifth-nearest neighbor hopping ($m = 2$). Since $\widehat{\boldsymbol{x}}$ is a lattice vector, $m\widehat{\boldsymbol{x}}$ is also a lattice vector, and so both second-nearest-neighbor hopping and fifth-nearest-neighbor hopping occur within each sublattice.

Case III: $m_{010}\boldsymbol{\delta} = m_{\bar{1}10}\boldsymbol{\delta} = \boldsymbol{\delta}$.

In this case, we have $t(\boldsymbol{\delta}) = U(m_{\bar{1}10})t(\boldsymbol{\delta})U(m_{\bar{1}10}) = U(m_{010})t(\boldsymbol{\delta})U(m_{010})$, and therefore we find that the submatrix takes the form

$$T = \begin{pmatrix} \epsilon_1 & & & & \\ & \epsilon_2 & & & \\ & & \epsilon_3 & & \\ & & & \epsilon_3 & \\ & & & & \epsilon_5 \end{pmatrix}.$$

This case only obtains for $\boldsymbol{\delta} = 0$, that is, on-site "hopping". It is no surprise that the on-site contributions should occur within each sublattice, and indeed 0 is a lattice vector. Case III is of course just a special case of cases I and II when $m = n = 0$.

With the general form and the three cases considered[a], we can construct the model Hamiltonian.

[a] A fourth case not considered occurs for larger hopping distances, which results from the consideration of Pythagorean triples. The first occurrence of this is at thirteenth-nearest-neighbors, and we only go out to fifth-nearest-neighbors in the present work. As such, the consequences of this consideration are left to the interested reader.

This has the form

$$H = (H_0 + H_2 + H_3 + H_5) + (H_1 + H_4)\,,$$

where H_n is the contribution from the n^{th}-nearest-neighbor. As we have demonstrated, H_1 and H_4 only involve hopping between sublattices, while the remaining H_n only involve hopping within sublattices. These H_n are found to be

$$\begin{aligned}
H_0 =& t(0) \\
H_1 =& t(\widehat{\boldsymbol{X}})e^{i(k_x+k_y)/2} + t^*(\widehat{\boldsymbol{X}})e^{-i(k_x+k_y)/2} + U(m_{010})\left[t(\widehat{\boldsymbol{X}})e^{i(k_x-k_y)/2} + t^*(\widehat{\boldsymbol{X}})e^{-i(k_x-k_y)/2}\right]U(m_{010}) \\
H_2 =& t(\widehat{\boldsymbol{x}})e^{ik_x} + t^*(\widehat{\boldsymbol{x}})e^{-ik_x} + U(m_{\bar{1}10})\left[t(\widehat{\boldsymbol{x}})e^{ik_y} + t^*(\widehat{\boldsymbol{x}})e^{-ik_y}\right]U(m_{\bar{1}10}) \\
H_3 =& t(2\widehat{\boldsymbol{X}})e^{i(k_x+k_y)} + t^*(2\widehat{\boldsymbol{X}})e^{-i(k_x+k_y)} + U(m_{010})\left[t(2\widehat{\boldsymbol{X}})e^{i(k_x-k_y)} + t^*(2\widehat{\boldsymbol{X}})e^{-i(k_x-k_y)}\right]U(m_{010}) \\
H_4 =& t(\widehat{\boldsymbol{x}}+\widehat{\boldsymbol{X}})e^{i(3k_x+k_y)/2} + t^*(\widehat{\boldsymbol{x}}+\widehat{\boldsymbol{X}})e^{-i(3k_x+k_y)/2} \\
&+ U(m_{010})\left[t(\widehat{\boldsymbol{x}}+\widehat{\boldsymbol{X}})e^{i(3k_x-k_y)/2} + t^*(\widehat{\boldsymbol{x}}+\widehat{\boldsymbol{X}})e^{-i(3k_x-k_y)/2}\right]U(m_{010}) \\
&+ U(m_{\bar{1}10})\left[t(\widehat{\boldsymbol{x}}+\widehat{\boldsymbol{X}})e^{i(3k_y+k_x)/2} + t^*(\widehat{\boldsymbol{x}}+\widehat{\boldsymbol{X}})e^{-i(3k_y+k_x)/2}\right]U(m_{\bar{1}10}) \\
&+ U(m_{\bar{1}10})U(m_{010})\left[t(\widehat{\boldsymbol{x}}+\widehat{\boldsymbol{X}})e^{i(3k_y-k_x)/2} + t^*(\widehat{\boldsymbol{x}}+\widehat{\boldsymbol{X}})e^{-i(3k_y-k_x)/2}\right]U(m_{010})U(m_{\bar{1}10}) \\
H_5 =& t(2\widehat{\boldsymbol{x}})e^{2ik_x} + t^*(2\widehat{\boldsymbol{x}})e^{-2ik_x} + U(m_{\bar{1}10})\left[t(2\widehat{\boldsymbol{x}})e^{2ik_y} + t^*(2\widehat{\boldsymbol{x}})e^{-2ik_y}\right]U(m_{\bar{1}10})
\end{aligned}$$

The band structure from this model for bulk FeSe is shown in fig. 2.1, which uses the non-zero parameters (adapted from Eschrig and Koepernik [32]):

$$\begin{array}{cccc}
\epsilon_1 = 0.014\,\text{eV} & \epsilon_2 = -0.539\,\text{eV} & \epsilon_3 = 0.020\,\text{eV} & \epsilon_5 = -0.581\,\text{eV} \\
t_{11}^{\widehat{\boldsymbol{X}}} = -0.063\,\text{eV} & t_{14}^{\widehat{\boldsymbol{X}}} = 0.305\,\text{eV} & t_{22}^{\widehat{\boldsymbol{X}}} = -0.412\,\text{eV} & t_{23}^{\widehat{\boldsymbol{X}}} = 0.364\,\text{eV} \\
t_{25}^{\widehat{\boldsymbol{X}}} = -0.338\,\text{eV} & t_{33}^{\widehat{\boldsymbol{X}}} = 0.311\,\text{eV} & t_{35}^{\widehat{\boldsymbol{X}}} = 0.180\,\text{eV} & t_{44}^{\widehat{\boldsymbol{X}}} = 0.080\,\text{eV} \\
t_{11}^{\widehat{\boldsymbol{x}}} = 0.086\,\text{eV} & t_{13}^{\widehat{\boldsymbol{x}}} = 0.056\,\text{eV} & t_{15}^{\widehat{\boldsymbol{x}}} = -0.109\,\text{eV} & t_{22}^{\widehat{\boldsymbol{x}}} = -0.066\,\text{eV} \\
t_{23}^{\widehat{\boldsymbol{x}}} = 0.089\,\text{eV} & t_{33}^{\widehat{\boldsymbol{x}}} = 0.232\,\text{eV} & t_{34}^{\widehat{\boldsymbol{x}}} = 0.099\,\text{eV} & t_{35}^{\widehat{\boldsymbol{x}}} = 0.146\,\text{eV} \\
t_{11}^{2\widehat{\boldsymbol{X}}} = -0.028\,\text{eV} & t_{33}^{2\widehat{\boldsymbol{X}}} = -0.045\,\text{eV} & t_{44}^{2\widehat{\boldsymbol{X}}} = 0.009\,\text{eV} & \\
t_{11}^{\widehat{\boldsymbol{x}}+\widehat{\boldsymbol{X}}} = 0.017\,\text{eV} & t_{33}^{\widehat{\boldsymbol{x}}+\widehat{\boldsymbol{X}}} = -0.019\,\text{eV} & t_{44}^{\widehat{\boldsymbol{x}}+\widehat{\boldsymbol{X}}} = 0.016\,\text{eV} & t_{33}^{2\widehat{\boldsymbol{x}}} = 0.027\,\text{eV}
\end{array}$$

For further hopping distances, some of the allowed terms are taken to be zero. We observe that

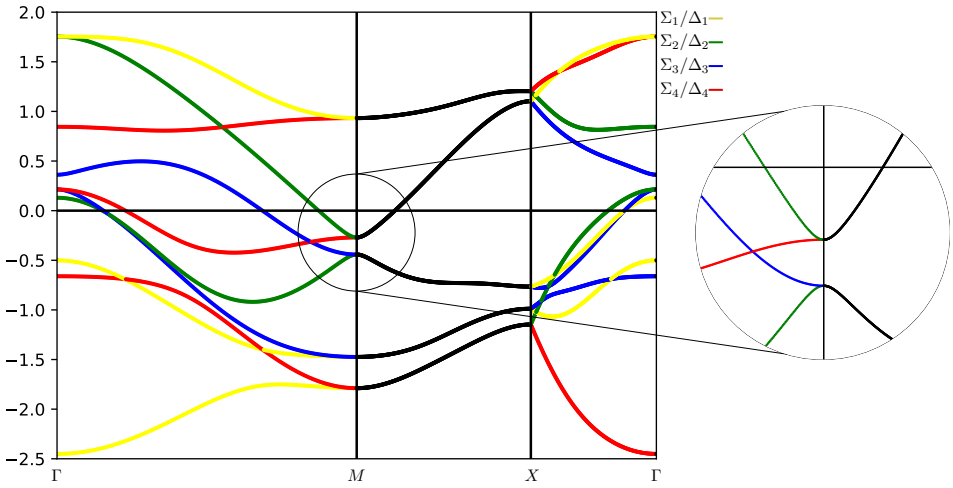

Figure 2.1: Band structure from the tight-binding model using parameters from [32]. This model reflects the band structure of bulk FeSe. Bands along the Σ- and Δ-line are colored according to their symmetry character. Inset, on the right, detail of the states near the Fermi energy around the M-point.

the d_{XY} and d_{Xz}/d_{Yz} orbitals give rise to three hole pockets near the Γ-point as well as two electron pockets near the M-point. In the monolayer, no hole pockets are observed and the electron pockets near the M-point are shallower. Additionally, the d_{XY} bands exhibit stronger renormalization. We capture this by taking $\epsilon_1 = .103\,\text{eV}$, $\epsilon_3 = -0.030\,\text{eV}$, $t^{\widehat{x}}_{11} = 0.012\,\text{eV}$, and $t^{\widehat{x}}_{33} = 0.176\,\text{eV}$. After making these adjustments, we get the band structure in fig. 2.2.

We also note that the band inversion near the M-point opens a gap across the entire Brillouin zone (see inset on fig. 2.2), creating two separated sets of bands. This results because the d_{XY} band and the d_{Yz} band have the same symmetry along the Σ-line. After the band inversion, these two bands exhibit an avoided crossing which creates the band gap. In the next section, we shall show that this gap is, in fact, topologically protected, and that monolayer FeSe has a non-trivial band topology.

2.2 BAND TOPOLOGY

We shall use topological quantum chemistry to analyze the two bands structures from fig. 2.1 and fig. 2.2. This approach compares the band connectivity to that of the so-called elementary band

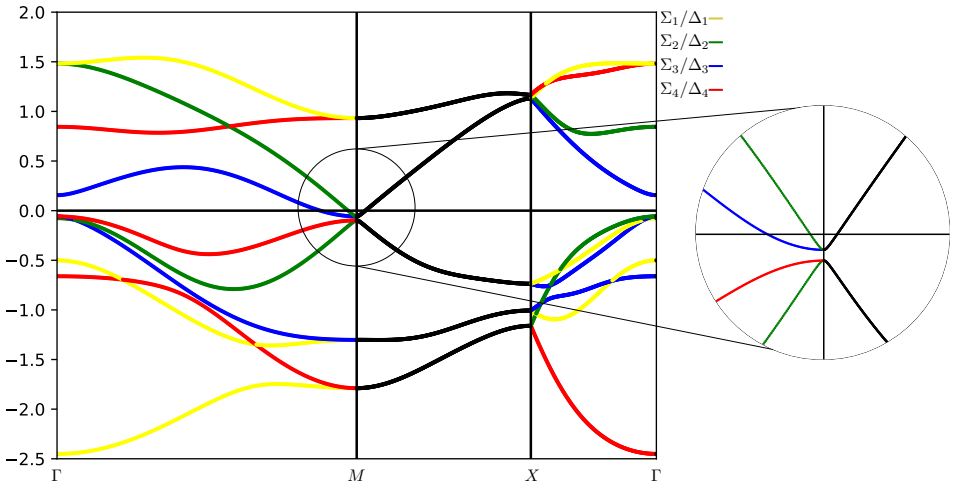

Figure 2.2: Band structure from the tight-binding model for monolayer FeSe. The hole pockets near the Γ-point has been pushed below the Fermi level and the bands near the Fermi level at the M-point have been inverted. Inset, on the right, detail of the states near the Fermi energy around the M-point.

representations. The underlying principle of topological quantum chemistry is to determine all possible band structures which can be continuously deformed to the atomic limit. Once identified, any band structure which is not described by a sum of elementary band representations must have a topological obstruction separating the band structure from the trivial phase.

A general explanation of the construction of elementary band representations is provided in [33]. In this section, we shall provide an intuitive, but less rigorous, explanation of the process for $P4/nmm$. As a general outline of the process, we identify the site-symmetry of various Wyckoff positions for $P4/nmm$. At each Wyckoff position, we can determine which representations the atomic orbitals belong to. These representations are then mapped to induced representations at each $\boldsymbol{k}$-point to describe an elementary band arising from the atomic orbitals. Because topology is a global property, the particular dispersion of the band does not matter, only the symmetry at each $\boldsymbol{k}$-point across the Brillouin zone.

We shall look at the elementary band representations of $P4/nmm$ in particular. To build intuitive understanding, we being by constructing a pictorial representation of the band arising from d_{XY} orbitals. Figure 2.3 depicts the allowable configurations for the d_{XY} orbitals corresponding to momenta at the Γ-, M-, and X-points. This diagram is constructed by first placing at any iron

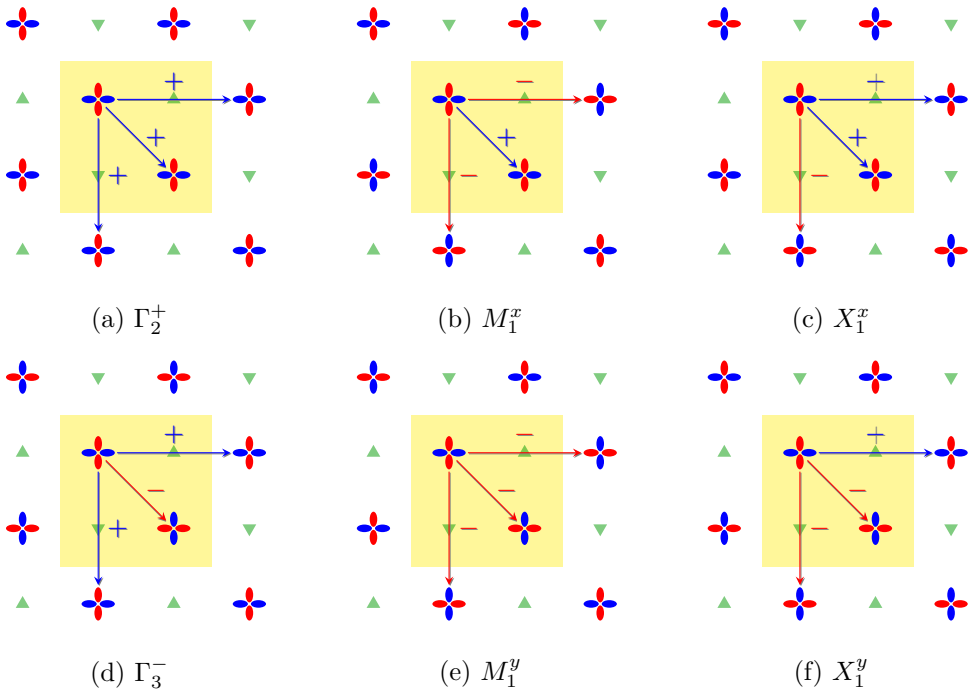

(a) Γ_2^+ (b) M_1^x (c) X_1^x

(d) Γ_3^- (e) M_1^y (f) X_1^y

Figure 2.3: Configurations for the d_{XY} orbitals at the iron-sites corresponding to momenta at the Γ-, M-, and X-points. Top row: orbital configurations with the same phase for each orbital in the highlighted unit cell, at the Γ-, M-, and X-points. Bottom row: orbital configurations with opposite phase on each orbital in the highlighted unit cell, at the Γ-, M-, and X-points.

site an orbital with any arbitrary phase. The crystal symmetry then restricts the orbital placed at the opposing site within the same unit cell to either have the same arbitrary phase, or for the two orbitals to be 180° out of phase. For any momentum $\boldsymbol{k}$, translation by a lattice vector $\boldsymbol{t}$ results in an overall change of phase by $\boldsymbol{k} \cdot \boldsymbol{t}$. So at the Γ-point there is no change of phase from one unit cell to the next. However, at the M-point translation by one unit cell in either the x-direction or y-direction results in a phase change of 180°. Also, at the X-point, which is usually taken to be $(0, \pi)$, there is no phase change when translating along the x-direction, but a 180° phase change when translating along the y-direction.

The pictures in fig. 2.3 are a depiction of the orbital configuration in an elementary band representation, arising from d_{XY} orbitals located at the iron sites. We can determine the induced representation which each configuration corresponds to simply by applying the group operations to the image and observing the result. We find that at the Γ-point, each configuration corresponds to a one-dimensional representation, so the elementary band representation at the Γ-point has symmetry character $\Gamma_2^+ \oplus \Gamma_3^-$. Meanwhile, both the M-point representation and the X-point representation

	$\{1\|0\,0\}$	$\{m_{001}\|\frac{1}{2}\,\frac{1}{2}\}$	$\{m_{1\bar{1}0}\|0\,0\}$	$\{2_{110}\|\frac{1}{2}\,\frac{1}{2}\}$	
$\Gamma_2^+ \downarrow \mathcal{G}_\Sigma$	1	1	-1	-1	Σ_2
$\Gamma_3^- \downarrow \mathcal{G}_\Sigma$	1	-1	1	-1	Σ_3
$M_1 \downarrow \mathcal{G}_\Sigma$	2	0	0	2	$\Sigma_2 \oplus \Sigma_3$

Table 2.1: Representations subduced from the Γ- and M-point representations for the elementary band representation arising from the d_{XY} orbitals, along the Σ-line. In the rightmost column is the decomposition into irreducible representations along the Σ-line. The Γ-point representations remain irreducible, while the M-point representation reduces to a direct sum of two Σ-line representations.

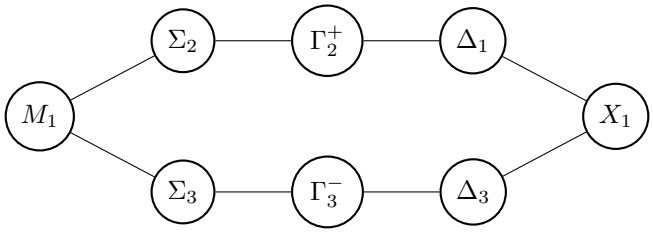

Figure 2.4: Graph depiction of the elementary band representation that results from considering d_{XY} orbitals at the iron-sites. The M_1 and X_1 representations are joined by the single Y representation along the Y-line (not depicted)

are two-dimensional, as expected. The d_{XY} orbitals produce an M_1 representation and an X_1 representation.

The manner in which representations at the Γ-, M-, and X-points reduce into representations along the Σ-, Δ-, and Y-lines determines the compatibility relations. Continuing our example, we consider how representation at the Γ-point and the M-point subduce to representations along the Σ-line. Given a representation ρ at the Γ-point, we define $\rho \downarrow \mathcal{G}_\Sigma(g) = \rho(g)$ for elements $g \in \mathcal{G}_\Sigma$. This subduced representation is a representation of $\mathcal{G}_\Sigma$ in the limit $\boldsymbol{k} \to \Gamma$, expressible as a direct sum of some irreducible representations on the Σ-line. The same procedure yields the subduction of representations at the M-point to the Σ-line, in the limit $\boldsymbol{k} \to M$. This is shown in table 2.1 for Γ_3^+, Γ_2^- and M_1, which are induced by the d_{XY} orbitals at the $2a$ Wyckoff position. The character tables for each $\boldsymbol{k}$-point are listed in appendix B.

The elementary band representation induced by the d_{XY} orbitals can be depicted as a graph which is reminiscent of an actual band structure, shown in fig. 2.4. For this graph, each node is labeled by a representation at a $\boldsymbol{k}$-point, and edges connect two nodes following the compatibility relations. There are four additional d-orbitals, but only three additional elementary band representations which arise from the d-orbitals, because the d_{Xz} and d_{Yz} orbitals belong to a two-dimensional

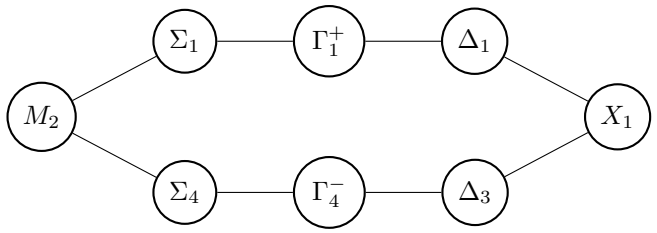

(a) A_1

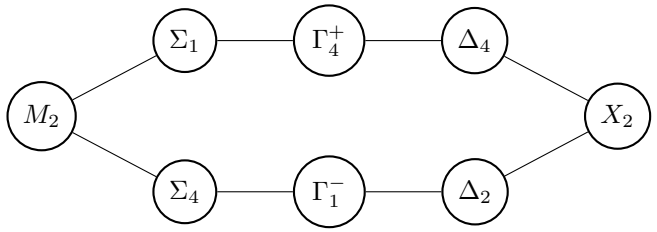

(b) B_2

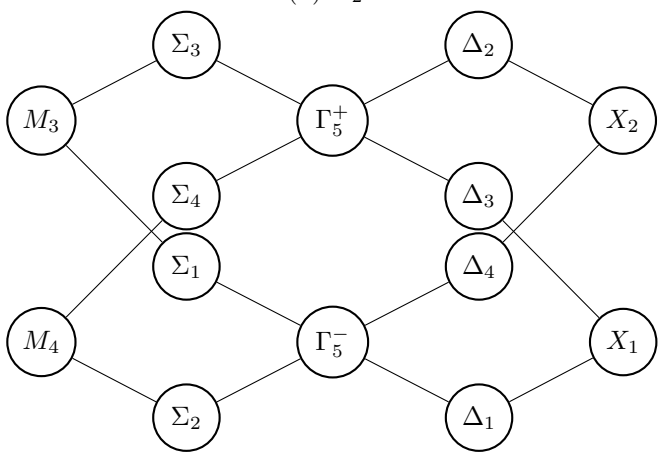

(c) E

Figure 2.5: The elementary band representations induced from the $d_{z^2-3r^2}$ (A_1), $d_{X^2-Y^2}$ (B_2), and (d_{Xz}, d_{Yz}) (E) orbitals placed at the iron sites.

representation and together induce only one elementary band representation. We could use the same pictorial method to determine these, however it is cumbersome to do so. Having served its purpose, we instead use the more general procedure which is outlined in [33]. The remaining elementary band representations which are induced from d-orbitals placed at the iron sites are shown in fig. 2.5. In each graph, the representations at the X- and M-points are connected by a Y-line which is not depicted; because there is only one two-dimensional representation on the Y-line, there are no crossings in this direction.

To compare the band structure from our tight binding model to the elementary band representations, we translate the band structures in figs. 2.1 and 2.2 to band graphs by identifying the

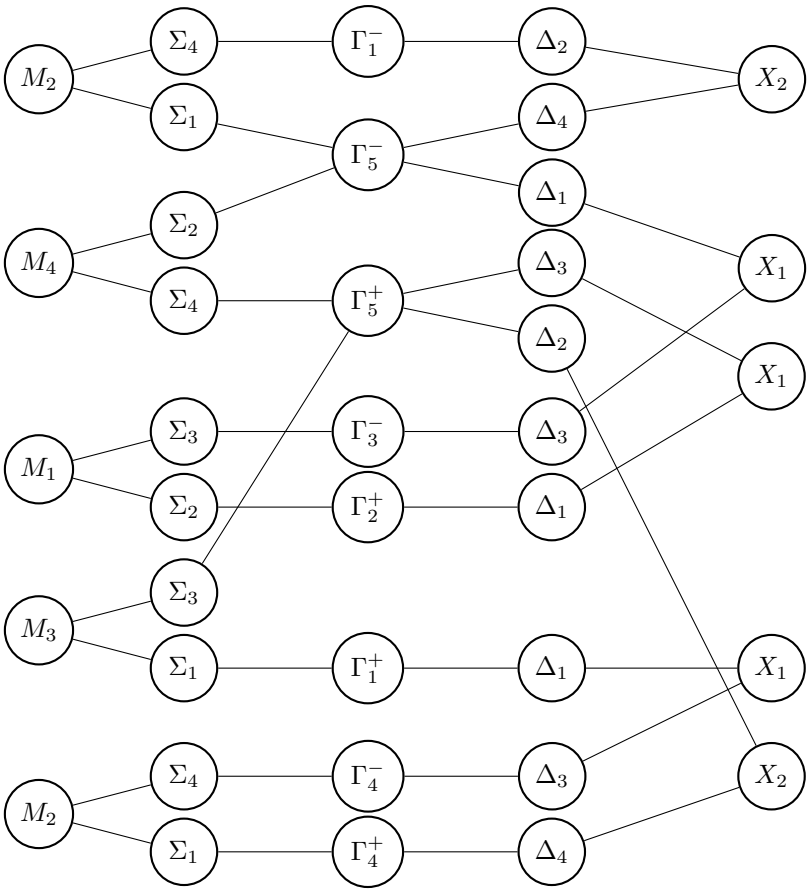

Figure 2.6: Band graph for bulk FeSe from the tight binding model. The nodes containing the representations at each high symmetry point are ordered according to their energy in the band structure, which are connected to the nodes for the high symmetry lines according to each band. Not shown are the nodes along the Y-line connecting the M and X points; there are no crossings in this direction.

symmetry of the eigenvectors at each $\boldsymbol{k}$-point. In fig. 2.6 we show the band graph that results from the band structure for bulk FeSe. The band graph consists of a single connected component and contains each of the elementary band representations so far discussed. One might expect to find four connected components instead of just one, but if any two elementary band representations are joined to form a single connected component, the resulting band structure remains topologically trivial. Because bulk FeSe has a single connected component consisting of elementary band representations, we are able to conclude that it is topologically trivial.

In comparison, the band graph for monolayer FeSe is shown in fig. 2.7, which clearly has two connected components. Should either of the two connected components be topologically non-trivial, then the band structure is topological (in this case, one non-trivial component implies both

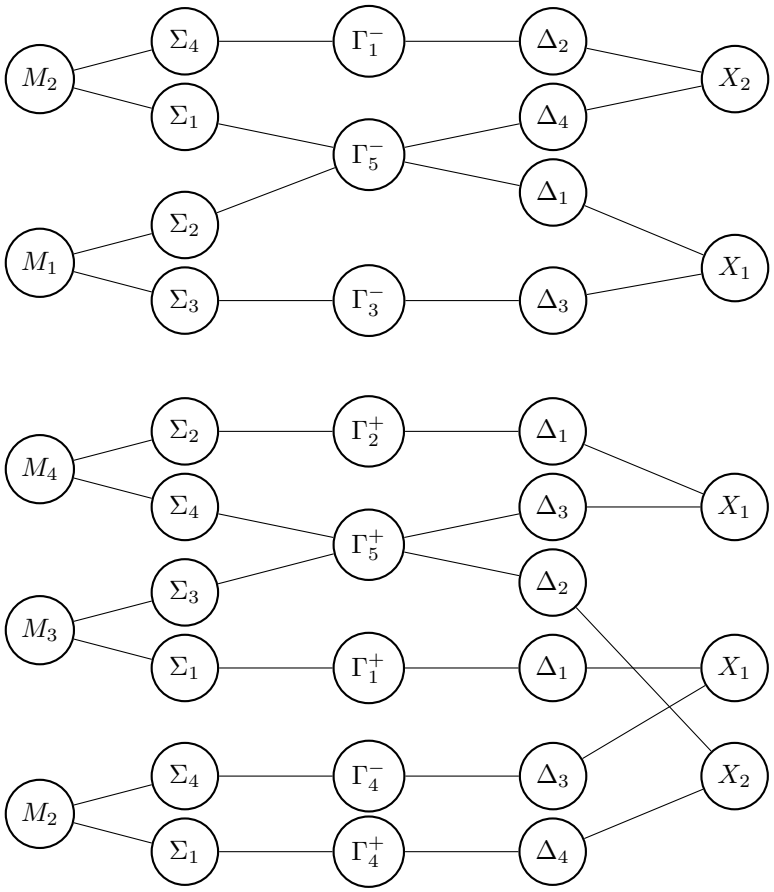

Figure 2.7: Band graph for monolayer FeSe from the tight binding model. The nodes containing the representations at each high symmetry point are ordered according to their energy in the band structure, which are connected to the nodes for the high symmetry lines according to each band. Not shown are the nodes along the Y-line connecting the M and X points; there are no crossings in this direction.

components are non-trivial). If we consider the upper set of bands, then at the Γ-point there are three representations: Γ_1^-, Γ_3^-, and Γ_5^-. From this alone we are able to conclude that for these bands to be topologically trivial, they can not arise from elementary band representations induced at the iron sites. We have already shown that the elementary band representations arising from the iron sites have an equal number of inversion symmetric representations as inversion antisymmetric representations, a consequence of the fact that the iron sites are not located at an inversion center. However, this alone is not sufficient to show that the band structure is topologically non-trivial.

So far, we have only considered the elementary band representations which arise from considering orbitals located at the iron sites. However, it could be the case that as the electrons interact, the localized Wannier functions which best describe the eigenstates of the Hamiltonian shift from being centered at the iron sites to being centered at a different Wyckoff position, such as the inversion center $4d$. As such, we must compare the band graph for monolayer FeSe in fig. 2.7 to all of the elementary band representations for $P4/nmm$ to make a determination of whether monolayer FeSe is topologically non-trivial. The remaining elementary band representations are generated in the same fashion according to each maximal Wyckoff position for $P4/nmm$. A full account of the elementary band representations for $P4/nmm$ can be found on the Bilbao Crystallographic Server; we can verify that the upper set of bands in fig. 2.7 is a non-trivial representation, and so FeSe is topologically non-trivial.

2.3 DISCUSSION

The orbital-selective renormalization of the d_{XY} bands from bulk FeSe to the monolayer drives the topological transition. This renormalization increases the electron-pocket minimum for the d_{XY} bands above the minimum for the d_{Xz}/d_{Yz} bands, providing the band inversion necessary for a topological transition. However, as band inversion alone is not sufficient for a topological transition, we compared the resulting band structure to the elementary band representations for $P4/nmm$. In doing so, we were able to determine that monolayer FeSe is indeed topologically non-trivial.

One important feature about the band structure for the monolayer which we observe in our tight-binding model is that the band structure is fully gapped. Furthermore, this gap is topologically protected and therefore robust. In this tight-biding model, we find that the only bands crossing

the Fermi energy arise from a single M-point representation (M_1), and it is on this basis that we develop the effective model in chapter 4 for the electron-pockets.

Having identified that monolayer FeSe is topological, it still remains to determine the topological invariant. We also expect there to be topologically protected edge states which arise from the non-trivial topology of the band structure, but we have not determined their nature at this time. Topological protection is ensured by some symmetry, or combination of symmetries—for instance, a topological insulator is protected by time-reversal, while a topological crystalline insulator is protected by time-reversal and some mirror plane. One avenue for further research, then, would be to identify which symmetries protect the topology of monolayer FeSe.

We also observe that among the two connected components of the band structure for FeSe, the $d_{3z^2-r^2}$ orbitals still form an elementary band representation. A toy model for studying the topology of monolayer FeSe could be constructed following the tight-binding model, with these bands removed. Similar toy models have been useful for studying the essential topology, such as the Haldane model for Dirac cones in graphene or the Kitaev chain.

Chapter 3

THE SPIN VORTEX CRYSTAL

While our primary interest in FeSe is in the unconventional nature of its superconductivity, we give some attention here to magnetic ordering, as magnetic fluctuations are generally understood to compete with superconductivity. Understanding the superconducting pairing mechanism also requires, therefore, understanding of the magnetic fluctuations present[48]. Most of the iron-based superconductors exhibit a C_2 antiferromagnetic stripe order[22], although bulk FeSe appears to be paramagnetic[49]. This has led to the investigation of various magnetic configurations to compete with the C_2 stripe order—sometimes also called collinear or single-$\boldsymbol{q}$ orders. In particular, there has been much interest in C_4 orders—alternatively, tetragonal or double-$\boldsymbol{q}$ orders—which have been given various labels; orthomagnetic (OM) and spin charge order (SCO)[50, 51, 52, 53], C_4 spin density wave (SDW)[54], spin vortex crystal (SVC) and charge-spin density wave (CSDW)[55, 56, 57]. The labels "orthomagnetic" and "spin vortex crystal" both describe the same ordered state, while "spin charge order" and "charge-spin density wave" also both describe the same ordered state, albeit a different state from the orthomagnetic/spin vortex crystal. In this work, which draws heavily from previously published work [34], we shall use spin vortex crystal and charge-spin density wave. We identify two types of spin vortex crystal, which are now generally referred to as "hedgehog" and "loop".

Substrate supported monolayer FeSe breaks the glide-plane symmetry of the bulk. While the effects of breaking this symmetry have not been observed at the Fermi surface, we consider its consequences on the stripe antiferromagnetic orders. We find that the stripe orders are unstable without the glide-plane. This suggests that the spin vortex crystal could be the magnetic ground

state for iron-based superconductors that lack inversion symmetry. Subsequent to our previous work, hole-doped $CaKFe_4As_4$ (belonging to $P4/mmm$) was found to support a hedgehog spin vortex crystal order [58, 59, 60]. We should note that bulk FeSe appears to be paramagnetic to low temperatures—it has been suggested that FeSe is in fact a quantum paramagnet [53, 61]—and so while this investigation was inspired by monolayer FeSe, it is not a good candidate to realize the spin vortex crystal.

We begin in section 3.1 by describing the magnetic orders that we consider; there are three energetically distinct, doubly-degenerate single-$\boldsymbol{q}$ orders—two with moments perpendicular to the c-axis, one with moments parallel to the c-axis—and for each degenerate pair of single-$\boldsymbol{q}$ orders, there is a corresponding pair of double-$\boldsymbol{q}$ orders which are superpositions of the single-$\boldsymbol{q}$ orders. These orders are categorized by their symmetry according to the representations of $P4/nmm$ introduced in chapter 1. In this section, we also show that breaking the glide-plane symmetry also breaks inversion symmetry and lifts the degeneracy between some of the described orders.

We then investigate a Landau model for the magnetic ground state in section 3.2, and demonstrate that lifting the degeneracy for the magnetic orders splits the transition temperature and favors the spin vortex crystal over stripe antiferromagnetism. Various other works[62, 51, 55, 63] have done similar mean field calculations for bulk crystals possessing the glide-plane.

3.1 MAGNETIC STRUCTURES

Single electron spin-orbit coupling in iron-based superconductors has been observed on a scale of $\sim 10\,\text{meV}$ [64], and neutron scattering experiments suggest that this single electron spin-orbit coupling is observed in the magnetic excitation spectrum, where a spin-space anisotropy exists to around 6–8 meV [65, 66]. Additionally, density-functional-theory calculations indicate a preferred spin direction [34]. In light of this, we consider a theory of magnetism in which the SU(2) spin rotation symmetry is not present, and instead where spin rotations are coupled to lattice symmetries.

The single- and double-$\boldsymbol{q}$ structures are so called because the moments on the iron sites can be described by a plane wave of spin density with one or two non-zero magnetic ordering vectors, respectively. Both types of magnetic structures can be described by writing the magnetic moment

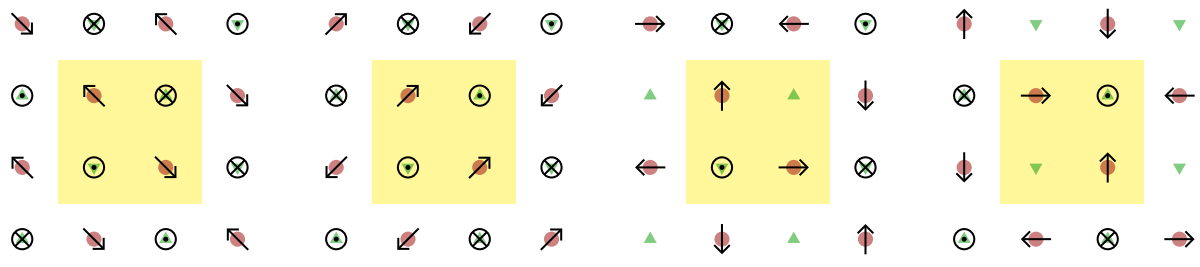

(a) M_4^X (b) M_4^Y (c) B_1 (d) A_2

Figure 3.1: The perpendicular stripe phases, a and b, and the related hedgehog spin vortex phases, c and d. The spin vortex can be seen as a superposition of the two stripe phases. The M_4 symmetry also permits moments on the selenium atoms (green triangles) directed perpendicular to the plane.

on the iron atoms $\boldsymbol{M}(\boldsymbol{r})$ as a function of position:

$$\boldsymbol{M}(\boldsymbol{r}) = \boldsymbol{M}_1 e^{i\boldsymbol{q}_1\cdot(\boldsymbol{r}-\widehat{\boldsymbol{Y}}/2)} + \boldsymbol{M}_2 e^{i\boldsymbol{q}_2\cdot(\boldsymbol{r}-\widehat{\boldsymbol{Y}}/2)}\,. \tag{3.1}$$

Here, $\boldsymbol{M}_i$ is a magnetic moment and $\boldsymbol{q}_i$ is the associated wave-vector describing a spin-density wave; the iron atoms are located at $\pm\widehat{\boldsymbol{Y}}/2$. Single-$\boldsymbol{q}$ orders can arise from this by taking $\boldsymbol{q}_2 = \boldsymbol{q}_1$, or by allowing $\boldsymbol{M}_2 \to 0$. For our purposes, we shall be considering $\boldsymbol{q}_1$ and $\boldsymbol{q}_2$ to be fixed, while allowing $\boldsymbol{M}_1$ and $\boldsymbol{M}_2$ to vary. In particular, we are interested in the ordering vectors $\boldsymbol{q}_1 = (\pi, \pi)$ and $\boldsymbol{q}_2 = (\pi, \overline{\pi})$, which are equivalent (but unequal) M-points in the Brillouin zone. In addition to the single-$\boldsymbol{q}$ stripe phases (having $\boldsymbol{M}_2 = 0$), the spin-vortex crystal is characterized by having $|\boldsymbol{M}_1| = |\boldsymbol{M}_2|$ and $\boldsymbol{M}_1 \cdot \boldsymbol{M}_2 = 0$, while the charge-spin density wave is characterized by having $\boldsymbol{M}_1 = \pm\boldsymbol{M}_2$. These orders all transform as components of some representation at the M-point, which for $P4/nmm$ are all two-dimensional.

There are twelve magnetic configurations which we consider. Six are single-$\boldsymbol{q}$ antiferromagnetic stripe states corresponding to moments aligned along one of three orthogonal directions (two in-plane directions, corresponding to the iron-iron directions, one out of plane along the c-axis), which provides a ferromagnetic stripe along one of the two iron-iron directions. These states come in degenerate pairs owing to the M-point symmetry that they inherit, and the remaining six magnetic configurations can be described as a change of basis from the single-$\boldsymbol{q}$ pairs. We show these states in figs. 3.1 to 3.3. Some of the magnetic configurations also allow for magnetic moments at the selenium sites, which are depicted as well.

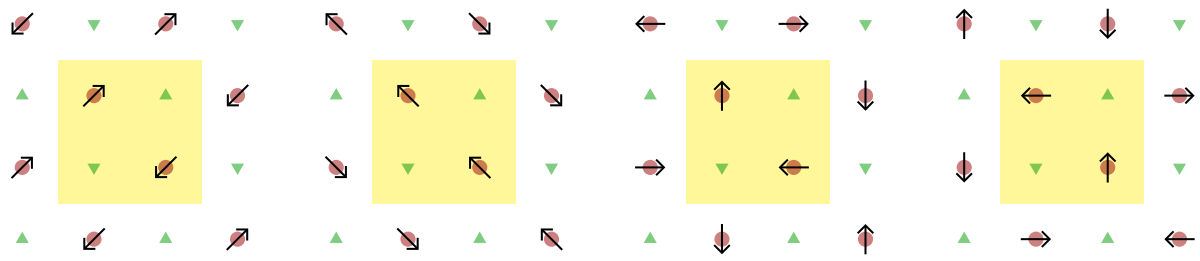

(a) M_3^X (b) M_3^Y (c) A_1 (d) B_2

Figure 3.2: The parallel stripe phases, a and b, and the related spin vortex loop phases, c and d. The spin vortex can be seen as a superposition of the two stripe phases. There are no moments on the selenium atoms permitted by the M_3 symmetry.

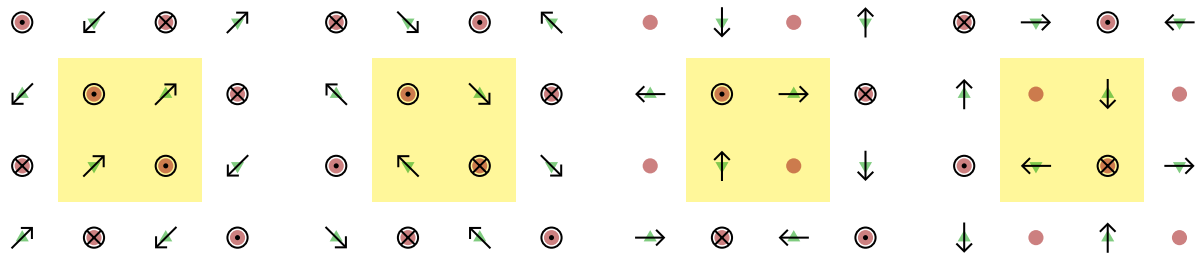

(a) M_1^X (b) M_1^Y (c) E^y (d) E^x

Figure 3.3: The c-axis stripe phases, a and b, and the related charge-spin density wave phases, c and d. The charge-spin density waves can be seen as a superposition of the two stripe phases. The charge-spin density wave should not be confused with a Néel antiferromagnet; the charge-spin density wave is a double-$\boldsymbol{q}$ spin density wave with $\boldsymbol{q}$ at M, whereas the Néel antiferromagnet (checkerboard order) is a single-$\boldsymbol{q}$ spin density wave with $\boldsymbol{q}$ at Γ.

In fig. 3.1 we have two "perpendicular" antiferromagnetic stripes which belong to the M_4 representation. For these orders the moment on the iron sites are perpendicular to the direction of the stripe. Belonging to the same representation are two hedgehog spin vortex orders; upon glide-plane symmetry breaking, the hedgehogs belong to the B_1 and A_2 representations

In fig. 3.2 we have two "parallel" antiferromagnetic stripes which belong to the M_3 representation. For these orders the moment on the iron sites are parallel to the direction of the stripe. Belonging to the same representation are two spin vortex loop orders; upon glide-plane symmetry breaking, the loops belong to the A_1 and B_2 representations.

Finally, in fig. 3.3 we have two stripe phases with c-axis moments, which belong to the M_1 representation. Belonging to the same representation are two charge-spin density waves[55]; upon glide-plane symmetry breaking, these states remain degenerate and belong to the E representation.

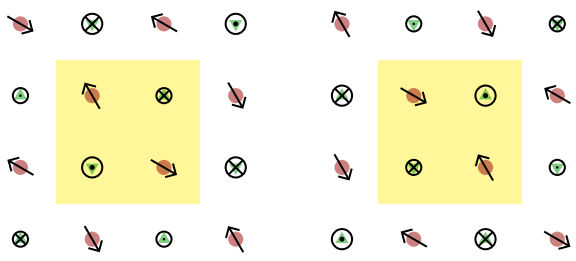

(a) M_1^1 (b) M_1^2

Figure 3.4: An example of the in-plane canted moments in a mixed state. The two states represent a pair belonging to the M_4 representation which retains the two-fold rotation symmetry about the c axis.

We also note that upon glide-plane symmetry breaking, the M_4 representation also reduces to the E representation, however we have not included the magnetic order with M_4 symmetry because it does not support moments on the iron sites.

The magnetic orders depicted in figs. 3.1 to 3.3 are demonstrative of only certain bases for the two-dimensional M-point representations. In principle, the low temperature order could result from a different basis. As an example, in fig. 3.4 we depict a different basis pair for M_4 representation, in which the moments tilt away from the normal to the stripe direction in a manner that maintains the two-fold rotation symmetry of the stripe phase. We refer to these general combinations collectively as mixed phases.

We introduced the M-point representations for $P4/nmm$ in chapter 1, but we include table 3.1 for ease of reference here. It is a simple exercise to verify that the magnetic configurations presented in figs. 3.1 to 3.3 transform according to their respective representations, provided one recalls that spin is a pseudo-vector which experiences an additional sign change under an improper rotation.

We can model glide-plane symmetry breaking by simply removing the generator $\{\overline{1}|0\,0\}$, noting that $\{m_{001}|\frac{1}{2}\,\frac{1}{2}\} = \{2_{001}|\frac{1}{2}\,\frac{1}{2}\}\{\overline{1}|0\,0\}$. When we do this, we observe that both the M_3 and M_4 representations become reducible. The transformation

$$U = \frac{1}{\sqrt{2}} \begin{pmatrix} 1 & 1 \\ -1 & 1 \end{pmatrix} \tag{3.2}$$

simultaneously diagonalizes the remaining representatives for $\{m_{1\overline{1}0}|0\,0\}$ and $\{m_{010}|0\,\frac{1}{2}\}$. If we

	$\{\bar{1}\|0\,0\}$	$\{m_{1\bar{1}0}\|0\,0\}$	$\{m_{010}\|0\,\frac{1}{2}\}$
M_1	$\begin{pmatrix} 1 & 0 \\ 0 & -1 \end{pmatrix}$	$\begin{pmatrix} -1 & 0 \\ 0 & 1 \end{pmatrix}$	$\begin{pmatrix} 0 & 1 \\ 1 & 0 \end{pmatrix}$
M_2	$\begin{pmatrix} 1 & 0 \\ 0 & -1 \end{pmatrix}$	$\begin{pmatrix} 1 & 0 \\ 0 & -1 \end{pmatrix}$	$\begin{pmatrix} 0 & 1 \\ 1 & 0 \end{pmatrix}$
M_3	$\begin{pmatrix} 1 & 0 \\ 0 & -1 \end{pmatrix}$	$\begin{pmatrix} 1 & 0 \\ 0 & 1 \end{pmatrix}$	$\begin{pmatrix} 0 & 1 \\ 1 & 0 \end{pmatrix}$
M_4	$\begin{pmatrix} 1 & 0 \\ 0 & -1 \end{pmatrix}$	$\begin{pmatrix} -1 & 0 \\ 0 & -1 \end{pmatrix}$	$\begin{pmatrix} 0 & 1 \\ 1 & 0 \end{pmatrix}$

Table 3.1: Physical irreducible representations at the M-point. The basis chosen here is well adapted to describe the antiferromagnetic stripes following, [67].

recall that $P4/nmm$ is non-symmorphic because the mirror planes $m_{\bar{1}10}$ and m_{010} do not contain an inversion center in their intersection, it is easy to see that by breaking inversion symmetry, the resulting space group must be symmorphic. As a result, representations at the M-point are not required to be two-dimensional, and the M_3 and M_4 representations become reducible. However, M_1 and M_2 remain irreducible even in the resulting symmorphic group, although they become equivalent representations. In the next section, we shall demonstrate that the spin vortex crystal becomes preferred as a direct consequence of M_3 and M_4 becoming reducible when inversion symmetry is broken.

3.2 LANDAU THEORY

Now that we have a identified the magnetic structures under discussion, and the group representations to which they belong, we perform a mean-field analysis which respects the symmetries present. Similar analyses have been done by others[55, 63, 57], although these works are concerned chiefly with the competition between the single- and double-$\boldsymbol{q}$ magnetic orders. Instead, we are chiefly concerned with the evolution from an in-plane stripe phase to the spin vortex crystal. Therefore, we have order parameters η_X and η_Y that transform as components of an M_i representation in the basis given in table 3.1. Essentially, we assume that the ground state prior to inversion breaking is one of the stripe phases. Our free energy in the vicinity of the phase transition is given by an

expansion in terms of (η_X, η_Y), and takes the form:

$$f = \alpha(\eta_X^2 + \eta_Y^2) + \beta_1(\eta_X^2 + \eta_Y^2)^2 + \beta_2\eta_X^2\eta_Y^2 \tag{3.3}$$

when inversion symmetry is present. Here η_X and η_Y transform as M_i^X and M_i^Y, respectively, and $\alpha = \alpha_0(t - t_c)$, with $\alpha_0 > 0$ and where t, t_c are dimensionless temperatures. To see the effects of inversion breaking, consider table 3.1. In particular, we note that under $\{\overline{1}|0\,0\}$, $\eta_X \to \eta_X$ while $\eta_Y \to -\eta_Y$. Thus, when inversion symmetry is broken and $\{\overline{1}|0\,0\}$ is no longer present, the free energy describing states with M_1 or M_2 symmetry allows additional terms carrying the product $\eta_X\eta_Y$, which are clearly not permitted when inversion symmetry is present—nor are such terms permitted for states with M_1 or M_2 symmetry, due to $\{m_{1\overline{1}0}|0\,0\}$. Adding these additional terms give the resulting free energy:

$$\widetilde{f} = \alpha(\eta_X^2 + \eta_Y^2) + \beta_1(\eta_X^2 + \eta_Y^2)^2 + \beta_2\eta_X^2\eta_Y^2 + \widetilde{\alpha}\eta_X\eta_Y + \beta_3\eta_X\eta_Y(\eta_X^2 + \eta_Y^2) \tag{3.4}$$

Compared to eq. (3.3), we have $\widetilde{f} = f + \widetilde{\alpha}\eta_X\eta_Y + \beta_3\eta_X\eta_Y(\eta_X^2 + \eta_Y^2)$. Since the transformation in eq. (3.2) diagonalizes both M_1 and M_2, we make the substitution $\eta_\pm = \frac{1}{\sqrt{2}}(\eta_X \pm \eta_Y)$. Under this substitution, we note that $\eta_X^2 + \eta_Y^2 \to \eta_+^2 + \eta_-^2$, while $\eta_X\eta_Y \to (\eta_+^2 - \eta_-^2)/2$. Equation (3.4) therefore becomes:

$$\begin{aligned}
\widetilde{f} =& \alpha(\eta_+^2 + \eta_-^2) + \beta_1(\eta_+^2 + \eta_-^2)^2 + \frac{\beta_2}{4}(\eta_+^2 - \eta_-^2)^2 + \frac{\widetilde{\alpha}}{2}(\eta_+^2 - \eta_-^2) + \frac{\beta_3}{2}(\eta_+^2 - \eta_-^2)(\eta_+^2 + \eta_-^2) \\
=& \left(\alpha + \frac{\widetilde{\alpha}}{2}\right)\eta_+^2 + \left(\alpha - \frac{\widetilde{\alpha}}{2}\right)\eta_-^2 + \left(\beta_1 + \frac{\beta_2}{4} + \frac{\beta_3}{2}\right)\eta_+^4 + \left(\beta_1 - \frac{\beta_3}{2} + \frac{\beta_2}{4}\right)\eta_-^4 \\
&+ \left(2\beta_1 - \frac{\beta_2}{2}\right)\eta_+^2\eta_-^2 \\
=& \alpha_+\eta_+^2 + \alpha_-\eta_-^2 + \beta_+\eta_+^4 + \beta_-\eta_-^4 + \beta_m\eta_+^2\eta_-^2\,.
\end{aligned} \tag{3.5}$$

We can take $\alpha_+ = \alpha_0(t - 1)$ and $\alpha_- = \alpha_0(t - 1 + \delta)$, and we have scaled temperature so that $t_{c+} = 1$. Requiring that the free energy be bounded below introduces the restrictions $\beta_\pm > 0$ and $\beta_m > -2\sqrt{\beta_+\beta_-}$. It can be shown that $\delta \equiv 1 - t_{c-} = -\widetilde{\alpha}/\alpha_0$; without loss of generality, we assume $T_{c+} > T_{c-}$; that is, $1 > t_{c-}$, giving $\delta > 0$ and $\widetilde{\alpha} < 0$. Manifestly, we have observed a splitting in the critical temperatures for the two phases described by η_+ and η_-.

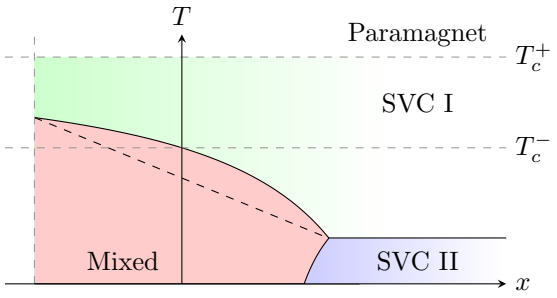

Figure 3.5: t-x phase diagram representative of $\xi < 1 - \delta$. The system initially undergoes a second order transition (at $t = 1$) into a spin vortex crystal state, for example, the B_1 hedgehog. For $\xi < 1 - \delta$, upon lowering temperature there is always a second transition, however for $\xi > 1 - \delta$ the first order transition to the alternate spin vortex phase, e.g., the A_2 hedgehog is suppressed.

It is useful to introduce the parameters

$$x = \frac{\beta_m}{2\beta_+}$$
$$\xi = \sqrt{\frac{\beta_-}{\beta_+}}\,.$$

In terms of these parameters, requiring that the free energy be bounded below gives the restrictions $\xi > 0$ and $x > -\xi$. We observe an initial second order transition from the paramagnetic state into a spin vortex crystal state—suppose this is the A_2 hedgehog state—below $t = 1$. We also find a further second order transition into the mixed state, which breaks the C_4 symmetry of the vortex, at

$$t_m = 1 - \left(\frac{1}{1-x}\right)\delta \tag{3.6}$$

provided $x < \xi$. In the mixed state the order parameters grow at different rates and we find that the magnitude of each order parameter is equal only along the line

$$t_s = 1 - \left(\frac{1+x}{1-\xi^2}\right)\delta\,,$$

Since this intersects with the transition t_m at $x = \pm\xi$, for $\xi \geq 1 - \delta$ the η_- state is suppressed and the stripe phase is absent from a region of the mixed state. For $\xi < 1 - \delta$, there can also be a transition from η_+ to η_-. Depending on the value of x, this is second order from the mixed state, or first order from the initial spin vortex crystal; e.g., if the first transition is into the A_2 hedgehog

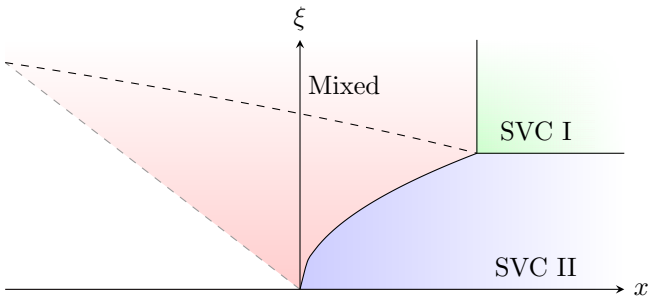

Figure 3.6: Zero temperature phase diagram in the x-ξ plane, for $\delta = 0.4$. At large values of ξ the conjugate vortex state is suppressed and the primary vortex state orders to zero temperature.

spin vortex crystal, the second transition is into the B_1 hedgehog spin vortex crystal. We show a representative diagram for $\xi = 0.5$, $\delta = 0.4$ ($\xi < 1 - \delta$) in the x-t plane in fig. 3.5, while fig. 3.6 shows a $t = 0$ diagram in the x-ξ plane with $\delta = 0.4$.

The parameter ξ can in some sense be thought as describing the strength of the mixed state; treating ξ as a free parameter, in the limit $\xi \to 0$ we see that the mixed state vanishes and that η_- orders at $t_{c-} = 1 - \delta$. Notably, we see that the stripe phase, which occupies a region of measure zero, is almost never going to be the ground state. Furthermore, for a large region of the phase diagram, two transitions are present.

As noted previously, when the ground state magnetic structure of the inversion symmetric parent compound belongs to the M_1 representation, breaking inversion symmetry does not lift the degeneracy of this magnetic state. However, it does allow for additional mixing terms which modify the transition temperature because the representations M_1 and M_2 become equivalent. If we assume without loss of generality that M_1 orders, then when inversion symmetry is present, we can write the free energy as

$$f_1 = \alpha(\eta_{X_1}^2 + \eta_{Y_1}^2) + \beta_1(\eta_{X_1}^2 + \eta_{Y_1}^2)^2 + \beta_2\eta_{X_1}^2\eta_{Y_1}^2\,, \tag{3.7}$$

where η_{X_1} and η_{Y_1} transform as the upper and lower components of M_1, respectively. We note then, that a term of the form $\eta_{X_1}\eta_{Y_2} + \eta_{X_2}\eta_{Y_1}$ is forbidden by $\{\bar{1}|0\,0\}$, but not by the other generators. So, upon breaking inversion symmetry, we get the modified free energy:

$$\widetilde{f_3} = f_3 + \alpha_m(\eta_{X_1}\eta_{Y_2} + \eta_{X_2}\eta_{Y_1}) + \widetilde{\alpha}(\eta_{X_2}^2 + \eta_{Y_2}^2)\,.$$

Minimizing this free energy with respect to η_{X_2} and η_{Y_2} modifies the term α; the result is

$$f_1 = \left(\alpha - \frac{\alpha_m^2}{4\widetilde{\alpha}}\right)(\eta_{X_1}^2 + \eta_{Y_1}^2) + \beta_1(\eta_{X_1}^2 + \eta_{Y_1}^2)^2 + \beta_2\eta_{X_1}^2\eta_{Y_1}^2 \,.$$

The critical temperature for the transition is found by setting the quadratic coefficient to zero. For $\widetilde{\alpha} < 0$, the transition temperature is lowered by the mixing.

3.3 DISCUSSION

In summary, we have studied the symmetry properties of various single- and double-$\boldsymbol{q}$ spin density waves. We observed that when inversion symmetry is broken for $P4/nmm$, the resulting subgroup is symmorphic and the irreducible representations at the M-point are no longer all two-dimensional. Rather than the stripe orders, the spin vortex crystal transforms as the irreducible representations in this lower symmetry system.

Inspired by the splitting of these representations, we used a mean-field analysis in the manner of Landau's theory of phase transitions to demonstrate the splitting of the critical temperature and the emergence of a second phase transition. These results suggest that the spin vortex crystal may be observable in systems which do not have the glide symmetry.

Our analysis uses monolayer FeSe on a $SrTiO_3$ substrate as our model system, however, we acknowledge that it is not a strong candidate to observe the spin vortex crystal, due to the paramagnetic behavior of the bulk material. However, a hedgehog spin vortex crystal phase has been found in $CaKFe_4As_4$ [58]. $CaKFe_4As_4$ belongs to $P4/mmm$, which does have inversion symmetry, but which lacks the glide plane that makes $P4/nmm$ non-symmorphic. While there have been no reports of a second transition, there is perhaps evidence of a quantum critical point [59].

It is perhaps interesting to note that a number of experiments have found evidence of the C_4 symmetric charge-spin density wave in hole doped Ba122 compounds[68, 69, 70, 71, 72, 73]. The space group of $BaFe_2As_2$, and indeed the 122 family, is I4/mmm, which is symmorphic and contains inversion symmetry. It is possible that a similar result would maintain and that the transition temperature would change when inversion symmetry is broken, such as by applying a c-axis electric field. However, further investigation would be needed to determine if this is indeed the case.

Chapter 4

NORMAL STATE LOW-ENERGY HAMILTONIAN

In this chapter we develop a low-energy effective model for the electron pockets near the M-point, which we showed in chapter 2 are well separated from the rest of the bands in the vicinity of the Fermi level. The model developed here was used by Agterberg *et al.* [74] in forwarding a nodeless d-wave superconducting gap function, the details of which are the subject of chapter 5.

In contrast to the tight-binding models discussed in chapter 2, the continuum model developed here is only valid near the M-point. The separation of the electron pockets from the rest of the band structure allows us to construct a model from a single M-point representation. In their previous work, Cvetkovic and Vafek [35] produce a similar model which is built by considering two M-point representations. That work based its model on FeAs, which does not exhibit the band inversion—and subsequent separation of the electron pockets from the rest of the band structure—observed in monolayer FeSe.

Similar to what was done in chapter 2, we will use group theoretic arguments to derive the general form of the low-energy Hamiltonian which can describe the bands which cross the Fermi level. The Hamiltonian describing the normal state should be invariant under the symmetry transformations of the space group; that is, the Hamiltonian belongs to the completely symmetric representation. However, the factors which contribute to the Hamiltonian obey certain orbital and spin symmetries which are not required to separately transform trivially.

We begin in section 4.1, which follows the method of invariants used by Cvetkovic and Vafek [67]. For this method, we consider individually the transformation properties of the linear, spin, and orbital momenta, and include in the Hamiltonian only products of these which are invariant. Then,

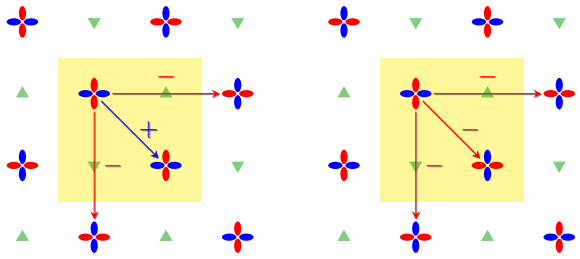

(a) M_1^X (b) M_1^Y

Figure 4.1: Two-component orbital configuration with d_{XY} orbitals. This orbital configuration belongs to the M_1 representation. The physical orbitals which contribute to the electron pockets are best described by some combination of d_{XY} and d_{Yz} orbitals.

	$\{\bar{1}\|0\,0\}$	$\{m_{1\bar{1}0}\|0\,0\}$	$\{m_{010}\|0\,\frac{1}{2}\}$
M_1	$\begin{pmatrix} 1 & 0 \\ 0 & -1 \end{pmatrix}$	$\begin{pmatrix} -1 & 0 \\ 0 & 1 \end{pmatrix}$	$\begin{pmatrix} 0 & 1 \\ 1 & 0 \end{pmatrix}$

Table 4.1: The M_1 representation, reprinted for clarity. A full derivation is given in appendix B.

in section 4.2, we use a double-group representation to consider the spin and orbital components in a unified manner. Double groups are extensions of space groups which are built to account for the double cover of $SU(2)$ on $SO(3)$, which properly treat spin symmetries.

4.1 METHOD OF INVARIANTS

As we discussed in chapter 2, the symmetry of the bands we are describing comes the M_1 representation, which we can view as arising from the d_{XY} orbitals, as shown in fig. 4.1, we present a schematic diagram for an orbital arrangement which demonstrates this symmetry; note that odd-integer translations introduce a π-phase change, which was a constraint imposed in constructing the physical irreducible representations at the M-point. We have also included a reproduction of the M-point representatives for the group generators in table 4.1 for ease of reference. The diagram in fig. 4.1 is only meant to be illustrative; the M_1 bands at this point consist of hybridized d_{XY} and d_{Yz} orbitals.

To build the M-point Hamiltonian, we begin by noting that because we have two bands (not including spin) which belong to an M_1 representation, we can express the orbital component in

P_Γ	$f(\boldsymbol{k})$	τ	σ	P_Γ	$f(\boldsymbol{k})$	τ
Γ_1^+	$c, k_x^2+k_y^2$	τ_0	σ_0	Γ_1^-	$\cdots$	τ_y
Γ_2^+	$k_x^2-k_y^2$	$\cdots$	$\cdots$	Γ_2^-	$\cdots$	$\cdots$
Γ_3^+	$\cdots$	$\cdots$	σ_z	Γ_3^-	$\cdots$	$\cdots$
Γ_4^+	k_xk_y	τ_z	$\cdots$	Γ_4^-	$\cdots$	τ_x
Γ_5^+	$\cdots$	$\cdots$	(σ_x,σ_y)	Γ_5^-	(k_x,k_y)	$\cdots$

Table 4.2: Symmetry adapted basis functions for the reciprocal, orbital, and spin spaces, to second order in $\boldsymbol{k}$. By taking appropriate products of these basis functions, we can determine a general form for the effective Hamiltonian. Because iron-selenide is a highly 2D material, we restrict $k_z = 0$.

terms of a set of Pauli matrices $\{\tau_x, \tau_y, \tau_z\}$. The action of a group element $g \in \mathcal{G}$ on τ_α is given by

$$g\tau_\alpha = D_{M_1}(\overline{g})\tau_\alpha D_{M_1}(g)\,,$$

where $D_{M_1}(g)$ is the matrix representation of g in the M_1 representation. According to this transformation rule, we are able to determine the representations which each orbital matrix belongs to, summarized in table 4.2. This table also includes spin by considering another set of Pauli matrices $\{\sigma_x, \sigma_y, \sigma_z\}$, which obeys the transformation property that $\boldsymbol{\sigma} = \sigma_x\widehat{\boldsymbol{x}} + \sigma_y\widehat{\boldsymbol{y}} + \sigma_z\widehat{\boldsymbol{z}}$ transforms as an axial vector. Likewise are included functions of momentum $\boldsymbol{k}$, which transforms as a polar vector. To go to quadratic order in $\boldsymbol{k}$, we also consider products arising from $\Gamma_5^- \otimes \Gamma_5^- = \Gamma_1^+ \oplus \Gamma_2^+ \oplus \Gamma_3^+ \oplus \Gamma_4^+$, and can identify $k_x^2+k_y^2$ as Γ_1^+, $k_x^2-k_y^2$ as Γ_2^+, and k_xk_y as Γ_4^+. Near the Fermi level, the quadratic approximation is reasonable, so we do not consider higher orders in $\boldsymbol{k}$.

The Hamiltonian must be symmetric under all group operations, so we must identify products of the orbital operators, spin operators, and functions of momentum which belong to the Γ_1^+ representation. In table 4.3, we list the product table of the representations at the Γ-point. For example, we see that the product $\Gamma_2^+ \otimes \Gamma_3^- = \Gamma_4^-$. Importantly, a product only contains Γ_1^+ if the two elements in the product are the same. The four τ matrices (including τ_0, the identity) for the orbital space belong to a vector space transforming as $\Gamma_1^+ \oplus \Gamma_4^- \oplus \Gamma_1^- \oplus \Gamma_4^+$; the four σ matrices for the spin space belong to a vector space transforming as $\Gamma_1^+ \oplus \Gamma_5^+ \oplus \Gamma_3^+$. Going to quadratic order, the functions of momentum belong to a vector space transforming as $\Gamma_1^+ \oplus (\Gamma_5^- \oplus \Gamma_3^-) \oplus [(\Gamma_5^- \oplus \Gamma_3^-) \otimes (\Gamma_5^- \oplus \Gamma_3^-)]$. The product space is then:

$$\{\Gamma_1^+ \oplus \Gamma_4^- \oplus \Gamma_1^- \oplus \Gamma_4^+\} \otimes \{\Gamma_1^+ \oplus \Gamma_5^+ \oplus \Gamma_3^+\} \otimes \{\Gamma_1^+ \oplus \Gamma_5^- \oplus \Gamma_3^- \oplus [(\Gamma_5^- \oplus \Gamma_3^-) \otimes (\Gamma_5^- \oplus \Gamma_3^-)]\}\,.$$

$\otimes$	Γ_1^a	Γ_2^a	Γ_3^a	Γ_4^a	Γ_5^a
Γ_1^b	Γ_1^c	Γ_2^c	Γ_3^c	Γ_4^c	Γ_5^c
Γ_2^b	Γ_2^c	Γ_1^c	Γ_4^c	Γ_3^c	Γ_5^c
Γ_3^b	Γ_3^c	Γ_4^c	Γ_1^c	Γ_2^c	Γ_5^c
Γ_4^b	Γ_4^c	Γ_3^c	Γ_2^c	Γ_1^c	Γ_5^c
Γ_5^b	Γ_5^c	Γ_5^c	Γ_5^c	Γ_5^c	$\Gamma_1^c \oplus \Gamma_2^c \oplus \Gamma_3^c \oplus \Gamma_4^c$

Table 4.3: Product table for the representations. Products of two representations having the same parity ($a = b$) are even parity ($c = +$), products of two representations having different parities ($a \neq b$) are odd parity ($c = -$).

Owing to the two-dimensional nature of FeSe, we constrain ourselves to $k_z = 0$, which transforms as the Γ_3^- representation for the momentum space functions. Removing these Γ_3^- terms gives a somewhat simpler expression:

$$\{\Gamma_1^+ \oplus \Gamma_4^- \oplus \Gamma_1^- \oplus \Gamma_4^+\} \otimes \{\Gamma_1^+ \oplus \Gamma_5^+ \oplus \Gamma_3^+\} \otimes \{\Gamma_1^+ \oplus \Gamma_5^- \oplus [\Gamma_5^- \otimes \Gamma_5^-]\}\,.$$

Next, we note that $\Gamma_5^+ \oplus \Gamma_3^+$ from the spin sector is odd under time-reversal, as is Γ_5^-, representing the terms linear in $\boldsymbol{k}$. The Hamiltonian is time-reversal invariant, so only terms which are quadratic in $\boldsymbol{k}$ or which contain products of $\boldsymbol{k}$ and $\boldsymbol{\sigma}$ survive. In the orbital space, Γ_1^- is also odd under time-reversal, but there are no Γ_1^- terms in the momentum-spin sector which could couple to this factor of the orbital space[a]. Therefore, the only terms which can contribute to the Hamiltonian come from the subspace given by:

$$\{\Gamma_1^+ \oplus \Gamma_4^- \oplus \Gamma_4^+\} \otimes \{(\Gamma_1^+ \otimes \Gamma_1^+) \oplus (\Gamma_5^+ \otimes \Gamma_5^-) \oplus (\Gamma_3^+ \otimes \Gamma_5^-) \oplus (\Gamma_1^+ \otimes [\Gamma_5^- \otimes \Gamma_5^-])\}\,.$$

The only terms in this expression which transform according to the Γ_1^+ representation are

$$(\Gamma_1^+ \otimes \Gamma_1^+ \otimes \Gamma_1^+) \oplus (\Gamma_1^+ \otimes \Gamma_1^+ \otimes \Gamma_5^- \otimes \Gamma_5^-) \oplus (\Gamma_4^- \otimes \Gamma_5^+ \otimes \Gamma_5^-) \oplus (\Gamma_4^+ \otimes \Gamma_1^+ \otimes \Gamma_5^- \otimes \Gamma_5^-)$$

We see that our space admits only four invariants. The $\Gamma_1^+ \otimes \Gamma_1^+ \otimes \Gamma_1^+$ is constant in each subspace, so we identify it with the chemical potential, μ. The terms involving $\Gamma_5^- \otimes \Gamma_5^- = \Gamma_1^+ \oplus \Gamma_2^+ \oplus \Gamma_3^+ \oplus \Gamma_4^+$ are quadratic in $\boldsymbol{k}$; as shown in table 4.2, $k_x^2 + k_y^2$ has Γ_1^+ symmetry, while $k_x k_y$ has Γ_4^+ symmetry.

[a]There is a Γ_1^- factor in the product $\Gamma_5^+ \otimes \Gamma_5^-$, but as this involves a product linear in spin and momentum, this factor is time-reversal invariant and so $\Gamma_1^- \otimes \Gamma_5^+ \otimes \Gamma_5^-$ is odd under time-reversal.

The invariant we assign to $\Gamma_1^+ \otimes \Gamma_1^+ \otimes \Gamma_5^- \otimes \Gamma_5^-$ is $1/2m$, as this behaves like a kinetic energy term. The invariant we assign to $\Gamma_4^+ \otimes \Gamma_1^+ \otimes \Gamma_5^- \otimes \Gamma_5^-$ is simply a and has units meV Å^2. Finally, the term $\Gamma_4^- \otimes \Gamma_5^+ \otimes \Gamma_5^-$ is linear in $\boldsymbol{k}$ and spin; the Γ_4^- component of the product $\Gamma_5^+ \otimes \Gamma_5^-$ is $k_y\sigma_x + k_x\sigma_y$. Dimensionally, this invariant is a speed (momentum per unit mass) and characterizes the only spin-orbit coupling in the model, so we assign v_{so} to the invariant. Taking the remaining orbital components from table 4.2 gives us the most general form of the Hamiltonian which still respects the group symmetries and which is time-reversal invariant:

$$H(\boldsymbol{k}) = \left(\frac{k_x^2 + k_y^2}{2m} - \mu\right) + ak_xk_y\tau_z + v_{\text{so}}\tau_x(k_y\sigma_x + k_x\sigma_y)\,. \tag{4.1}$$

In this final expression, the product between the orbital and spin Pauli matrices is understood as a Kronecker product, and we have suppressed τ_0 and σ_0 which are simply the identity in their respective spaces.

4.2 DOUBLE GROUP METHOD

The usual procedure to add spin degrees of freedom to a space group is to construct the so-called "double" group. Double groups introduce a "spin flip" element to the group structure; the resulting group is doubled in size as a spin flip is a second-order element (a spin-flip followed by a second spin-flip returns to the identity). In this section we will construct a general Hamiltonian using a double group representation as presented on the Bilbao Crystallographic Server [75]. Considering both spin and orbital degrees-of-freedom, the bands at the M-point are four-fold degenerate, which transforms as the $\overline{M}_5$ representation of the double group. The representatives for $\overline{M}_5$ are written in table 4.4, which we can use as an alternate means to determine the Hamiltonian. In table 4.4, the elements which involve a spin-flip are written ${}^d g$; so $\{{}^d 1|00\}$ represents purely a spin flip, with no spatial rotations or translations.

We have written the matrix representatives in terms of Pauli matrices τ_μ and σ_ν, but whereas in section 4.1 the τ_μ matrices described orbital degrees of freedom and the σ_ν matrices described spin degrees of freedom, the Bilbao Crystallographic Server uses a different basis and so here τ_μ and σ_ν are merely convenient labels.

We want to determine the most generic Hamiltonian which obeys inversion symmetry and

$\{1\|0\,0\}$	$\tau_0\sigma_0$	$\{^{\mathrm{d}}1\|0\,0\}$	$-\tau_0\sigma_0$
$\{\bar{1}\|0\,0\}$	$\tau_z\sigma_0$	$\{^{\mathrm{d}}\bar{1}\|0\,0\}$	$-\tau_z\sigma_0$
$\{\mathrm{m}_{001}\|\frac{1}{2}\,\frac{1}{2}\}$	$-i\tau_z\sigma_z$	$\{^{\mathrm{d}}\mathrm{m}_{001}\|\frac{1}{2}\,\frac{1}{2}\}$	$i\tau_z\sigma_z$
$\{2_{001}\|\frac{1}{2}\,\frac{1}{2}\}$	$-i\tau_0\sigma_z$	$\{^{\mathrm{d}}2_{001}\|\frac{1}{2}\,\frac{1}{2}\}$	$i\tau_0\sigma_z$
$\{\mathrm{m}_{110}\|\frac{1}{2}\,\frac{1}{2}\}$	$-\frac{i}{2}[(\tau_0-\tau_z)\sigma_x+(\tau_0+\tau_z)\sigma_y]$	$\{^{\mathrm{d}}\mathrm{m}_{110}\|\frac{1}{2}\,\frac{1}{2}\}$	$\frac{i}{2}[(\tau_0-\tau_z)\sigma_x+(\tau_0+\tau_z)\sigma_y]$
$\{2_{110}\|\frac{1}{2}\,\frac{1}{2}\}$	$\frac{i}{2}[(\tau_0-\tau_z)\sigma_x-(\tau_0+\tau_z)\sigma_y]$	$\{^{\mathrm{d}}2_{110}\|\frac{1}{2}\,\frac{1}{2}\}$	$-\frac{i}{2}[(\tau_0-\tau_z)\sigma_x-(\tau_0+\tau_z)\sigma_y]$
$\{\mathrm{m}_{1\bar{1}0}\|0\,0\}$	$\frac{i}{2}[(\tau_0+\tau_z)\sigma_x-(\tau_0-\tau_z)\sigma_y]$	$\{^{\mathrm{d}}\mathrm{m}_{1\bar{1}0}\|0\,0\}$	$-\frac{i}{2}[(\tau_0+\tau_z)\sigma_x-(\tau_0-\tau_z)\sigma_y]$
$\{2_{1\bar{1}0}\|0\,0\}$	$\frac{i}{2}[(\tau_0+\tau_z)\sigma_x+(\tau_0-\tau_z)\sigma_y]$	$\{^{\mathrm{d}}2_{1\bar{1}0}\|0\,0\}$	$-\frac{i}{2}[(\tau_0+\tau_z)\sigma_x+(\tau_0-\tau_z)\sigma_y]$
$\{\mathrm{m}_{100}\|\frac{1}{2}\,0\}$	$-i\tau_x\sigma_x$	$\{^{\mathrm{d}}\mathrm{m}_{100}\|\frac{1}{2}\,0\}$	$i\tau_x\sigma_x$
$\{2_{100}\|\frac{1}{2}\,0\}$	$-\tau_y\sigma_x$	$\{^{\mathrm{d}}2_{100}\|\frac{1}{2}\,0\}$	$\tau_y\sigma_x$
$\{\mathrm{m}_{010}\|0\,\frac{1}{2}\}$	$-i\tau_x\sigma_y$	$\{^{\mathrm{d}}\mathrm{m}_{010}\|0\,\frac{1}{2}\}$	$i\tau_x\sigma_y$
$\{2_{010}\|0\,\frac{1}{2}\}$	$-\tau_y\sigma_y$	$\{^{\mathrm{d}}2_{010}\|0\,\frac{1}{2}\}$	$\tau_y\sigma_y$
$\{4^+_{001}\|\frac{1}{2}\,0\}$	$\frac{1}{2}[(\tau_x-i\tau_y)\sigma_0-i(\tau_x+i\tau_y)\sigma_z]$	$\{^{\mathrm{d}}4^+_{001}\|\frac{1}{2}\,0\}$	$-\frac{1}{2}[(\tau_x-i\tau_y)\sigma_0-i(\tau_x+i\tau_y)\sigma_z]$
$\{\bar{4}^+_{001}\|\frac{1}{2}\,0\}$	$\frac{1}{2}[(\tau_x-i\tau_y)\sigma_0+i(\tau_x+i\tau_y)\sigma_z]$	$\{^{\mathrm{d}}\bar{4}^+_{001}\|\frac{1}{2}\,0\}$	$-\frac{1}{2}[(\tau_x-i\tau_y)\sigma_0+i(\tau_x+i\tau_y)\sigma_z]$
$\{4^-_{001}\|0\,\frac{1}{2}\}$	$\frac{1}{2}[(\tau_x+i\tau_y)\sigma_0+i(\tau_x-i\tau_y)\sigma_z]$	$\{^{\mathrm{d}}4^-_{001}\|0\,\frac{1}{2}\}$	$-\frac{1}{2}[(\tau_x+i\tau_y)\sigma_0+i(\tau_x-i\tau_y)\sigma_z]$
$\{\bar{4}^-_{001}\|0\,\frac{1}{2}\}$	$-\frac{1}{2}[(\tau_x+i\tau_y)\sigma_0-i(\tau_x-i\tau_y)\sigma_z]$	$\{^{\mathrm{d}}\bar{4}^-_{001}\|0\,\frac{1}{2}\}$	$\frac{1}{2}[(\tau_x+i\tau_y)\sigma_0-i(\tau_x-i\tau_y)\sigma_z]$

Table 4.4: Representations over $\mathbb{C}$ for the double group of $P4/nmm$ around the M-point. Here τ_μ and σ_ν are convenient labels to express the four-dimensional representation in terms of Kronecker products; this labeling does not reflect the underlying spin or orbital bases.

time-reversal symmetry. However, in order to impose the constraints from time-reversal (Θ) and inversion ($\mathcal{P}$), we must determine the form of these operators in the basis that was chosen to express the representatives in table 4.4 from the Bilbao server. This basis is unknown, but $\mathcal{P}$ is given in the form of $\{\bar{1}|0\,0\}$, so we have only to construct Θ. Following the work of Yang and Nagaosa [76], we can construct the proper expression of Θ by satisfying the following four conditions:

$$\begin{aligned} &\text{I.} && \Theta\Theta^\dagger = -1 \\ &\text{II.} && \Theta^2 = -1 \\ &\text{III.} && (\Theta\mathcal{P})^2 = -1 \\ &\text{IV.} && [\Theta, \{g|\boldsymbol{\tau}\}] = 0 \end{aligned}$$

Condition I implies that we can write $\Theta = UK$, where U is unitary and K is complex conjugation. Condition II then gives that U is antisymmetric. From condition III, we observe that $U = e^{i\phi}(\cos\alpha + i\sin\alpha\tau_z)\sigma_y$; in the case of the usual expression of the time-reversal operator, we would have $\phi = \pi/2$ and $\alpha = 0$, but this turns out not to be the case in this basis. Writing $\cos\alpha + i\sin\alpha\tau_z = e^{i\alpha\tau_z}$, we have $\Theta = e^{i(\alpha\tau_z+\phi)}K$.

Condition IV implies $\Theta\{g|\boldsymbol{\tau}\}\Theta^{-1} = \{g|\boldsymbol{\tau}\}$, however when this is expressed in terms of the $\overline{M}_5$ representation, we observe

$$\Gamma^5_M(\Theta)\Gamma^5_M(\{g|\boldsymbol{\tau}\})\Gamma^5_M(\Theta^{-1}) = \Gamma^5_{-M}(\{g|\boldsymbol{\tau}\})\,.$$

Recalling that $\Gamma^5_{-M}(\{g|\boldsymbol{\tau}\}) = \Gamma^5_M(\{g|-\boldsymbol{\tau}\}) = \Gamma^5_M(\{g|\boldsymbol{\tau}-2\boldsymbol{\tau}\})$, where $2\boldsymbol{\tau}$ is a lattice translation for $P4/nmm$, allows us to conclude that

$$\Gamma^5_M(\Theta)\Gamma^5_M(\{g|\boldsymbol{\tau}\})\Gamma^5_M(\Theta^{-1}) = e^{-2iM\cdot\boldsymbol{\tau}}\Gamma^5_M(\{g|\boldsymbol{\tau}\})\,.$$

In particular, we see that the representative for Θ in this basis should in fact *anti*commute with the representative for $\{m_{100}|\frac{1}{2}\,0\}$. From this it follows that $\alpha = \pi/2$; since the phase is undetermined, we choose $\phi = 0$ to make the unitary part of Θ real. Thus, we find $\mathcal{P}$ is given by τ_z and Θ is given by $i\tau_z\sigma_y K$.

We can express the Hamiltonian in the form

$$\widetilde{H}(\boldsymbol{k}) = \sum_{\mu\nu} c_{\mu\nu}(\boldsymbol{k})\tau_\mu\sigma_\nu \,.$$

Because $H(\boldsymbol{k})$ is Hermitian, we find $c_{\mu\nu}(\boldsymbol{k}) = c^*_{\mu\nu}(\boldsymbol{k})$, i.e., our coefficients are real functions of $\boldsymbol{k}$. The constraints from parity and time-reversal are

$$\mathcal{P}H(-\boldsymbol{k})\mathcal{P}^{-1} = H(\boldsymbol{k})$$
$$\Theta H(-\boldsymbol{k})\Theta^{-1} = H(\boldsymbol{k})\,.$$

If we apply both parity and time-reversal, we can relate $H(\boldsymbol{k})$ back to itself, which will allow us to put strong constraints on the functions $c_{\mu\nu}(\boldsymbol{k})$. In doing so, we find

$$c_{\mu\nu}(\boldsymbol{k}) = \begin{cases} c_{\mu\nu}(\boldsymbol{k}) & \mu = y \text{ xor } \nu = 0 \\ -c_{\mu\nu}(\boldsymbol{k}) & \text{otherwise.} \end{cases}$$

This constraint shows that many of the $c_{\mu\nu}(\boldsymbol{k})$ are necessarily zero, and what remains is a Hamiltonian of the form

$$\widetilde{H}(\boldsymbol{k}) = c_{00}(\boldsymbol{k}) + c_{yx}(\boldsymbol{k})\tau_y\sigma_x + c_{yy}(\boldsymbol{k})\tau_y\sigma_y + c_{yz}(\boldsymbol{k})\tau_y\sigma_z + c_{z0}(\boldsymbol{k})\tau_z + c_{x0}(\boldsymbol{k})\tau_x \,.$$

We can further specify the functional form of the remaining $c_{\mu\nu}(\boldsymbol{k})$ by considering the actions of the group on the Hamiltonian, which remains invariant under all group transformations. Using the representatives from table 4.4, we see that $\tau_z\sigma_0$ transforms as a 1D irreducible representation, and the pairs $\tau_y(\sigma_x,\, \sigma_y)$ and $(\tau_y\sigma_z,\, \tau_x)$ transform as 2D representations. While $\tau_y(\sigma_x, \sigma_y)$ belongs to an irreducible 2D representation, $(\tau_y\sigma_z,\, \tau_x)$ actually belongs to a reducible representation. We find that the sum, $\tau_x + \tau_y\sigma_z$, and difference $\tau_x - \tau_y\sigma_z$, transform as 1D irreducible representations. The transformation properties are summarized in table 4.5, along with $\boldsymbol{k}$-dependent basis functions for each representation. From this table we see that $c_{x0}(\boldsymbol{k})$ and $c_{yz}(\boldsymbol{k})$ are each proportional to k_z, which we drop from the Hamiltonian as we are taking $k_z \to 0$ owing to the two-dimensional nature of FeSe.

	$\{\bar{1}\|0\,0\}$	$\{m_{1\bar{1}0}\|0\,0\}$	$\{m_{010}\|0\,\frac{1}{2}\}$	Irrep.	$c_{\mu\nu}(\boldsymbol{k})$
$\tau_0\sigma_0$	1	1	1	Γ_1^+	$c, k_x^2+k_y^2$
$\tau_z\sigma_0$	1	1	-1	Γ_4^+	k_xk_y
$\tau_x+\tau_y\sigma_z$	-1	1	1	Γ_3^-	k_z
$\tau_x-\tau_y\sigma_z$	-1	-1	1	Γ_4^-	$k_z(k_x^2-k_y^2)$
$\tau_y(\sigma_x,\,\sigma_y)$	$\begin{pmatrix}-1 & 0\\ 0 & -1\end{pmatrix}$	$\begin{pmatrix}0 & -1\\ -1 & 0\end{pmatrix}$	$\begin{pmatrix}1 & 0\\ 0 & -1\end{pmatrix}$	Γ_5^-	$(k_x,\,-k_y)$

Table 4.5: Symmetry properties for the component matrices of the Hamiltonian, the associated Γ-point irreducible representation, and the $\boldsymbol{k}$-dependent basis functions. We include k_z components for completeness, but take $k_z \to 0$ in the final expression.

The remaining terms are $c_{00}(\boldsymbol{k}) = (k_x^2+k_y^2)/2m - \mu$, $c_{yx}(\boldsymbol{k}) = v_{\mathrm{so}}k_x$, $c_{yy}(\boldsymbol{k}) = -v_{\mathrm{so}}k_y$, and $c_{z0}(\boldsymbol{k}) = ak_xk_y$, so in this basis the Hamiltonian takes the form:

$$H(\boldsymbol{k}) = \left(\frac{k_x^2+k_y^2}{2m} - \mu\right) + ak_xk_y\tau_z + v_{\mathrm{so}}\tau_y(k_x\sigma_x - k_y\sigma_y)\,. \tag{4.2}$$

The Hamiltonian in eq. (4.2) is brought into agreement with that in eq. (4.1), under the change of basis given by the unitary transformation $U = \frac{1}{2}(\tau_0 + i\tau_z)(\sigma_0 - i\sigma_z)$. Under this same transformation, we see that $\Theta \to i\sigma_yK$ and $\mathcal{P} \to \tau_z$, which accords with the stated basis for section 4.1 where the τ matrices described orbital degrees of freedom while σ matrices described spin degrees of freedom.

4.3 DISCUSSION

The main result for this chapter is the form of the normal state Hamiltonian. We have found the most general Hamiltonian, expanded to second order in $\boldsymbol{k}$ around the M-point, for the bands which cross the Fermi level in FeSe. We find that taking $\mu = 55\,\mathrm{meV}$, $1/2m = 1375\,\mathrm{meV\ \AA}^2$, and $a = 600\,\mathrm{meV\ \AA}^2$ gives good agreement with experiment [16], especially in terms of the size of the Fermi surface. We plot the dispersion and Fermi surface in fig. 4.2 for a moderate spin-orbit coupling strength $v_{\mathrm{so}} = 12\,\mathrm{meV\ \AA}$. Without spin-orbit coupling, the Fermi surface would feature two overlapping (non-interacting) ellipses; spin-orbit coupling hybridizes the bands and separates them at the Fermi level into inner and outer pockets. The ARPES data from [16] has 5 meV resolution, and within that limit there is no discernible hybridization owing to spin-orbit coupling. This provides a limit to the strength of the spin-orbit coupling, $|v_{\mathrm{so}}| \leq 15\,\mathrm{meV\ \AA}$. Despite this

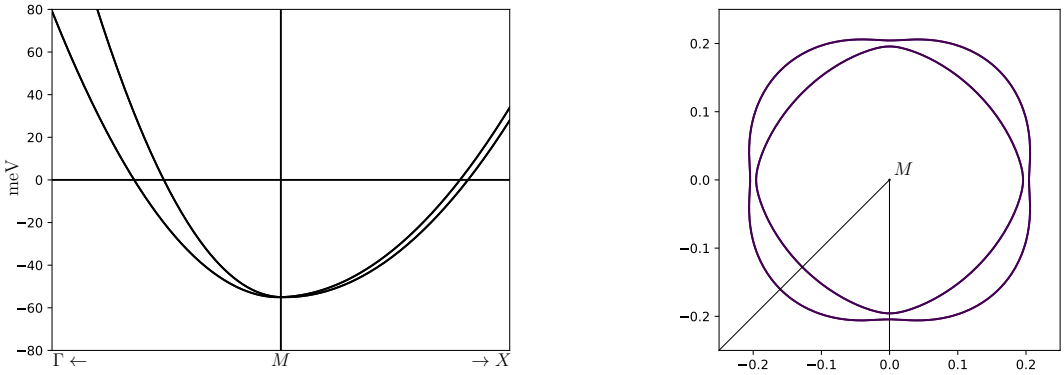

Figure 4.2: Dispersion of bands and Fermi surface near the M-point using the parameters given in the text. We have taken $v_{\mathrm{so}} = 12\,\mathrm{meV\ \AA}$, which gives reasonable agreement.

limitation, many works argue that spin-orbit coupling is an essential part of the description of iron-based superconductors [64, 66, 77, 78].

In chapter 3 we investigated the effect that inversion symmetry breaking had on the magnetic structure. If we allow for inversion breaking, the Hamiltonian given in eq. (4.2) is further modified by the addition of

$$H_I(\boldsymbol{k}) = c\tau_y\sigma_z + d(k_x^2 - k_y^2)\tau_x + \lambda_1(k_y\sigma_x - k_x\sigma_y) + \lambda_2\tau_z(k_x\sigma_x - k_y\sigma_y)\,.$$

These inversion breaking terms hybridize the bands in a similar manner to spin-orbit coupling, but as there is no discernible hybridization in the ARPES data [16], the effect of inversion symmetry breaking appears to be small, so we choose to neglect it at this time.

The model developed here respects the symmetry constraints and includes a spin-orbit coupling term which hybridizes the bands, creating distinct inner and outer pockets; to the resolution limit of available ARPES data, our model reproduces the observed Fermi surface. The lack of clear hybridization in the ARPES data provides an upper limit on the strength of hybridizing terms such as spin-orbit coupling or inversion symmetry breaking. We shall use the model Hamiltonian from eq. (4.1) to describe the normal state for our investigation of superconductivity in the next chapter.

Chapter 5

SUPERCONDUCTIVITY

Monolayer FeSe has an unexpectedly large superconducting critical temperature [79, 24, 29] when grown on a $SrTiO_3(001)$ substrate; the monolayer also forms the foundation for the family of iron-based superconductors. It has been argued that interfacial coupling to phonon modes in the substrate is largely responsible for enhancing an underlying pairing interaction [15, 80], although the evidence of such a coupling has been questioned recently [81, 82]. At present, this work is more concerned with identifying the underlying mechanism rather than the enhancement of the critical temperature.

Owing to the proximity to magnetic order [83, 84], and considering the importance of spin-orbit coupling [64, 20, 66, 85], the pairing interaction in the iron-based superconductors is argued to be the result of electron-electron interactions, rather than the electron-phonon interactions of conventional superconductors. The symmetry of the superconducting gap is determined by the underlying pairing interaction, and therefore determining the symmetry of the superconducting gap would constrain the possible pairing interactions. However, to date, a clear determination of the gap symmetry has not been made.

ARPES measurements typically report a nodeless gap [12, 13, 14, 15, 16, 17, 18], while other probes are argued to indicate a nodal gap [86, 87, 88, 89, 90]. Some of the ARPES results show a clearly anisotropic gap [16, 17, 18], while others report an isotropic (or "nearly isotropic") gap [12, 13, 14, 15, 18]. STM measurements typically show a nodeless gap in the density of states, in agreement with the ARPES data [19, 20, 21, 91, 92]. Also present in some of the STM measurements is evidence of multiple gaps, seen as additional peaks in the $\mathrm{d}I/\mathrm{d}V$ spectrum [19, 20, 21].

In single band superconductors, such as the cuprates, a d-wave gap is nodal. In light of this, the nodeless gap in the iron-based superconductors was initially cited as evidence of s-wave superconductivity. However, studies of multiband systems have shown that the symmetry enforced nodes of a d-wave can migrate off the normal state Fermi surface and annihilate, leading to a completely gapped, or nodeless, d-wave state [93, 94, 95]. Monte Carlo investigations of the pairing interactions which can occur in a two-band model have found that d-wave superconductivity can arise from antiferromagnetic spin exchange[96], such as between nearest-neighbors. Because the crystallographic unit cell for FeSe has two iron-sites, this spin exchange does not carry momentum.

Here, we focus on the symmetry of the gap. We will begin by classifying the symmetry of different gap functions in section 5.1, which is similar to the construction of the normal state Hamiltonian in chapter 4. Then, using a model for a $\boldsymbol{q} = 0$ spin-exchange interaction, we also show that the d-wave state is most stable in the limit of no spin-orbit coupling. However, this limit is not realistic, and so we present the linearized gap equation that results from a finite spin-orbit coupling, although a solution to this gap equation is still lacking.

Despite lacking a determination of the stable superconducting state in the presence of spin-orbit coupling, we are still able to investigate the properties of both the A_{1g} (s-wave) and B_{2g} (d-wave) gaps. In section 5.2, we show that both the A_{1g} and B_{2g} gap functions produce a nodeless, anisotropic gap with multiple peaks in the density of states. Similar work, using a four-band model, has been done by Eugenio and Vafek [97], as well as Böker *et al.* [98].

5.1 CLASSIFICATION OF SUPERCONDUCTING STATES

The normal state Hamiltonian can be written as

$$H = \sum_{\boldsymbol{k}} \Psi^{\dagger}_{\boldsymbol{k}} H(\boldsymbol{k}) \Psi_{\boldsymbol{k}} \,,$$

where $H(\boldsymbol{k})$ was determined in chapter 4 to be

$$H(\boldsymbol{k}) = \epsilon_0(\boldsymbol{k}) + \gamma_{xy}(\boldsymbol{k})\tau_z + \tau_x[\gamma_x(\boldsymbol{k})\sigma_y + \gamma_y(\boldsymbol{k})\sigma_x] \,.$$

P_Γ	$f(\boldsymbol{k})$	τ	σ	P_Γ	$f(\boldsymbol{k})$	τ
A_{1g}	$c, k_x^2 + k_y^2$	τ_0	σ_0	A_{1u}	$\cdots$	τ_y
A_{2g}	$\cdots$	$\cdots$	σ_z	A_{2u}	$\cdots$	$\cdots$
B_{1g}	$k_x^2 - k_y^2$	$\cdots$	$\cdots$	B_{1u}	$\cdots$	$\cdots$
B_{2g}	$k_x k_y$	τ_z	$\cdots$	B_{2u}	$\cdots$	τ_x
E_g	$\cdots$	$\cdots$	(σ_x, σ_y)	E_u	(k_x, k_y)	$\cdots$

Table 5.1: Symmetry adapted basis functions for the reciprocal, orbital, and spin spaces, to second order in $\boldsymbol{k}$.

The τ Pauli matrices describe the orbital degree of freedom while the σ Pauli matrices describe the spin degree of freedom. The superconducting Hamiltonian is typically written in Bogoliubov-de Gennes form as

$$H_{\mathrm{BdG}}(\boldsymbol{k}) = \begin{pmatrix} H(\boldsymbol{k}) & \Delta(\boldsymbol{k}) \\ -\Delta^*(-\boldsymbol{k}) & -H^*(-\boldsymbol{k}) \end{pmatrix},$$

where $H(\boldsymbol{k})$ is the normal state Hamiltonian, and $\Delta(\boldsymbol{k})$ is known as the gap function.

In this section, we construct gap functions that belong to different irreducible representations, using the same method of invariants as section 4.1. While the normal state Hamiltonian is required to belong to the completely symmetric representation, the gap function can belong to a lower symmetry representation. In conventional superconductors, the superconducting phase breaks only a gauge symmetry because of the phase coherence of Cooper pairs in the ground state. As evidenced by the cuprates, however, superconductors that break additional crystal symmetries exist as well.

Continuing to work with a basis of orbital matrices τ and spin matrices σ, we write $\Delta(\boldsymbol{k}) = \sum_{\mu\nu}[c_{\mu\nu}(\boldsymbol{k})\tau_\mu\sigma_\nu]i\sigma_y$. As was showed in chapter 4, the factor $i\sigma_y$ is the unitary component of the time-reversal operator in this basis. Separating out this time-reversal factor allows us to more readily identify the symmetry of the gap function[7]. Pauli exclusion requires fermion wave-functions to be antisymmetric, which in a single band superconductor allows the division of the gap functions into even parity, spin-singlet pairing and odd parity, spin-triplet pairing. In this case, spin-singlet pairing results in even parity factors $c_{\mu\nu}(\boldsymbol{k})$ only for symmetric orbital pairs involving τ_0, τ_z and τ_x. For the antisymmetric orbital pairs involving τ_y it is instead spin-triplet pairing which results in even parity factors $c_{\mu\nu}(\boldsymbol{k})$. Furthermore, the overall symmetry is no longer determined by the $\boldsymbol{k}$-dependence of the gap function alone.

To consider the role of the orbital degree of freedom, we consider table 5.1 to classify the products

Γ	s-like	d-like	p-like
A_{1g}	c	$k_x k_y \tau_z$	$\tau_x(k_y\sigma_x + k_x\sigma_y)$
A_{2g}	$\cdots$	$(k_x^2 - k_y^2)\tau_z$	$\tau_x(k_x\sigma_x - k_y\sigma_y)$
B_{1g}	$\cdots$	$(k_x^2 - k_y^2)$	$\tau_x(k_y\sigma_x - k_x\sigma_y)$
B_{2g}	$c\tau_z$	$k_x k_y$	$\tau_x(k_x\sigma_x + k_y\sigma_y)$
E_g	$\cdots$	$\cdots$	$(k_x, k_y)\tau_y$; $(k_x, k_y)\tau_x\sigma_z$

Table 5.2: Even parity basis gap functions $\Delta(\boldsymbol{k}) = [c_{\mu\nu}(\boldsymbol{k})\tau_\mu\sigma_\nu]i\sigma_y$. The multi-orbital nature of the material, along with spin-orbit coupling, generically mixes s-,p-, and d-like basis functions, and results in both interorbital and intraorbital pairing. The Kronecker product is understood and $\tau_0 = \mathbb{1}$, $\sigma_0 = \mathbb{1}$ are omitted.

Γ	s-like	d-like	p-like
A_{1u}	$\cdots$	$k_x k_y \tau_x$	$(k_x\sigma_x + k_y\sigma_y)$; $\tau_z(k_x\sigma_y + k_y\sigma_x)$
A_{2u}	$c\tau_y\sigma_z$	$(k_x^2 - k_y^2)\tau_x$	$(k_x\sigma_y - k_y\sigma_x)$; $\tau_z(k_x\sigma_x - k_y\sigma_y)$
B_{1u}	$\cdots$	$k_x k_y \tau_y\sigma_z$	$(k_x\sigma_x - k_y\sigma_y)$; $\tau_z(k_x\sigma_y - k_y\sigma_x)$
B_{2u}	$c\tau_x$	$(k_x^2 - k_y^2)\tau_y\sigma_z$	$(k_x\sigma_y + k_y\sigma_x)$; $\tau_z(k_x\sigma_x + k_y\sigma_y)$
E_u	$c\tau_y(\sigma_x, \sigma_y)$	$(k_x^2 - k_y^2)\tau_y(\sigma_x, \sigma_y)$; $k_x k_y \tau_y(\sigma_x, \sigma_y)$	$(k_x, k_y)\sigma_z$; $(k_x, k_y)\tau_z\sigma_z$

Table 5.3: Odd parity basis gap functions $\Delta(\boldsymbol{k}) = [c_{\mu\nu}(\boldsymbol{k})\tau_\mu\sigma_\nu]i\sigma_y$. The multi-orbital nature of the material, along with spin-orbit coupling, generically mixes s-,p-, and d-like basis functions, and results in both interband and intraband pairing. The tensor product is understood and $\tau_0 = \mathbb{1}$, $\sigma_0 = \mathbb{1}$ are omitted.

$c_{\mu\nu}(\boldsymbol{k})\tau_\mu\sigma_\nu$ into pairing channels[a]. The results are tabulated in table 5.2 and table 5.3. We see, for example, that a gap with A_{1g} symmetry, typically associated with s-wave pairing, is described to second order in $\boldsymbol{k}$ by the usual spin-singlet term $\Delta_0 i\sigma_y$, but also allows orbital-selective terms $(\Delta_z/k_0^2)k_x k_y \tau_z i\sigma_y$ and a spin triplet $(\Delta_t/k_0)\tau_x(k_y\sigma_x + k_x\sigma_y)i\sigma_y$.

Tables 5.2 and 5.3 are organized into s-, p-, and d-like momentum space functions; this is a description only for the structure of the gap as a function of $\boldsymbol{k}$, as the overall symmetry is given by the representation in the left-most column of each table. The s-like functional dependence is isotropic, while the p-like functions are linear in $\boldsymbol{k}$ and the d-like functions change sign under a four-fold rotation of $\boldsymbol{k}$. Owing to the orbital symmetry of τ_z, the d-like contribution to the A_{1g} gap function remains invariant under a four-fold rotation, as $\tau_z \to -\tau_z$ and $k_x k_y \to -k_x k_y$ under a four-fold rotation.

In the next section, we shall see how an antiferromagnetic pairing interaction supports both an

[a] In comparison to table 4.2, we have the same characterization but use Mulliken symbols to label the representations. Mulliken symbols are the conventional choice for classifying superconducting gap functions.

A_{1g} gap and a B_{2g} gap.

5.1.1 PAIRING INTERACTION

The linearized gap equation in the weak-coupling limit given some pairing potential V is

$$\Delta_{ss'}(\boldsymbol{k}) = -\frac{1}{\beta}\sum_{\substack{\boldsymbol{k}'\,\omega_n\\ s_3\,s_4}} V_{s's s_3 s_4}(\boldsymbol{k},\boldsymbol{k}')\widetilde{\Delta}_{s_3 s_4}(\boldsymbol{k}')\,, \tag{5.1}$$

where $\widetilde{\Delta}(\boldsymbol{k}) = G^0(\boldsymbol{k},\omega_n)\Delta(\boldsymbol{k})G^0(-\boldsymbol{k},-\omega_n)$, using the normal state Green's function $G^0(\boldsymbol{k},\omega_n) = [i\omega_n - H(\boldsymbol{k})]^{-1}$. Deviating slightly from the notation in section 5.1, here the subscripts s are proper indices which range over the spin and orbital degrees of freedom. In order to find solutions to the gap equation, the form of the pairing potential $V_{s_1 s_2 s_3 s_4}(\boldsymbol{k},\boldsymbol{k}')$ must be specified.

To determine a model pairing potential, we consider an antiferromagnetic exchange interaction given by

$$g\sum_{\boldsymbol{k}\,\boldsymbol{q}} f(\boldsymbol{k})\boldsymbol{S}_{-\boldsymbol{q}}\cdot\Psi^\dagger_{\boldsymbol{k}+\boldsymbol{q}/2}\tau_x\boldsymbol{\sigma}\Psi_{\boldsymbol{k}-\boldsymbol{q}/2}\,, \tag{5.2}$$

where $\boldsymbol{\sigma}$ is the Pauli vector and the form factor $f(\boldsymbol{k}) = 1 + \alpha(\boldsymbol{k}^2/k_0^2)$ is taken to lowest non-vanishing order in $\boldsymbol{k}$. This represents an antiferromagnetic interaction between the spin $\boldsymbol{\sigma}$ with some background spin fluctuation $\boldsymbol{S}_{-\boldsymbol{q}}$. Because FeSe does not exhibit low-temperature magnetic order, we assume a static spin susceptibility, which prevents long-range magnetic order and consider a weak-coupling approximation. We find that the resulting effective interaction becomes

$$-\,g^2\chi_0\xi^2\sum_{\substack{\boldsymbol{k},\boldsymbol{k}'\\ \boldsymbol{q}}} f(\boldsymbol{k})f(\boldsymbol{k}')\Psi^\dagger_{\boldsymbol{k}+\boldsymbol{q}/2}\tau_x\boldsymbol{\sigma}\Psi_{\boldsymbol{k}-\boldsymbol{q}/2}\cdot\Psi^\dagger_{\boldsymbol{k}'-\boldsymbol{q}/2}\tau_x\boldsymbol{\sigma}\Psi_{\boldsymbol{k}'+\boldsymbol{q}/2}\,, \tag{5.3}$$

which results because the spin-fluctuations arise from spins at different sites. In addition, we include a repulsive on-site Hubbard repulsion that competes with the pairing interaction, which can be expressed in the same manner as eq. (5.2); doing so gives:

$$\begin{aligned}\frac{U}{8}\sum_{\substack{\boldsymbol{k},\boldsymbol{k}'\\ \boldsymbol{q}}}\Big[&\Psi^\dagger_{\boldsymbol{k}+\boldsymbol{q}/2}\tau_0\sigma_0\Psi_{\boldsymbol{k}-\boldsymbol{q}/2}\Psi^\dagger_{\boldsymbol{k}'-\boldsymbol{q}/2}\tau_0\sigma_0\Psi_{\boldsymbol{k}'+\boldsymbol{q}/2} + \Psi^\dagger_{\boldsymbol{k}+\boldsymbol{q}/2}\tau_z\sigma_0\Psi_{\boldsymbol{k}-\boldsymbol{q}/2}\Psi^\dagger_{\boldsymbol{k}'-\boldsymbol{q}/2}\tau_z\sigma_0\Psi_{\boldsymbol{k}'+\boldsymbol{q}/2}\\ &-\Psi^\dagger_{\boldsymbol{k}+\boldsymbol{q}/2}\tau_0\sigma_z\Psi_{\boldsymbol{k}-\boldsymbol{q}/2}\Psi^\dagger_{\boldsymbol{k}'-\boldsymbol{q}/2}\tau_0\sigma_z\Psi_{\boldsymbol{k}'+\boldsymbol{q}/2} - \Psi^\dagger_{\boldsymbol{k}+\boldsymbol{q}/2}\tau_z\sigma_z\Psi_{\boldsymbol{k}-\boldsymbol{q}/2}\Psi^\dagger_{\boldsymbol{k}'-\boldsymbol{q}/2}\tau_z\sigma_z\Psi_{\boldsymbol{k}'+\boldsymbol{q}/2}\Big]\end{aligned}$$

If we let $\boldsymbol{k}+\frac{\boldsymbol{q}}{2}=\boldsymbol{p}$, $\boldsymbol{k}'+\frac{\boldsymbol{q}}{2}=-\boldsymbol{p}'$, and $\boldsymbol{k}-\frac{\boldsymbol{q}}{2}=\boldsymbol{p}'$, then we satisfy $\boldsymbol{k}=-\boldsymbol{k}'=\frac{1}{2}(\boldsymbol{p}+\boldsymbol{p}')$ and $\boldsymbol{q}=\boldsymbol{p}-\boldsymbol{p}'$. Noting that $f(\boldsymbol{k}')=f(-\boldsymbol{k}')=f(\boldsymbol{k})$ and taking $g^2\beta\chi_0\xi^2=V$, the combined interaction can be written

$$\sum_{\boldsymbol{p},\boldsymbol{p}'}\sum_{\substack{ij\\kl}}\sum_{\substack{\alpha\beta\\\gamma\delta}}\left\{\frac{U}{8}\left(\tau_0^{ij}\tau_0^{kl}+\tau_z^{ij}\tau_z^{kl}\right)\left(\sigma_0^{\alpha\beta}\sigma_0^{\gamma\delta}-\sigma_z^{\alpha\beta}\sigma_z^{\gamma\delta}\right)-Vf^2\left(\frac{\boldsymbol{p}+\boldsymbol{p}'}{2}\right)\tau_x^{ij}\tau_x^{kl}\boldsymbol{\sigma}^{\alpha\beta}\cdot\boldsymbol{\sigma}^{\gamma\delta}\right\}$$
$$\times\, c^\dagger_{\boldsymbol{p}i\alpha}c_{\boldsymbol{p}'j\beta}c^\dagger_{-\boldsymbol{p}k\gamma}c_{-\boldsymbol{p}'l\delta}\,.$$

This form is not well suited for use in the linearized gap equation (eq. (5.1)), so we express this interaction in pairing channels. We find

$$\begin{aligned}
&\sum_{\boldsymbol{p},\boldsymbol{p}'}\sum_{\substack{ij\\kl}}\sum_{\substack{\alpha\beta\\\gamma\delta}}\left\{\frac{U}{8}\left([\tau_0^{ik}][\tau_0^{jl}]^\dagger+[\tau_z^{ik}][\tau_z^{jl}]^\dagger\right)\left([i\sigma_y^{\alpha\gamma}][i\sigma_y^{\beta\delta}]^\dagger-[(\sigma_z i\sigma_y)^{\alpha\gamma}][(\sigma_z i\sigma_y)^{\beta\delta}]^\dagger\right)\right.\\
&+\frac{V}{4}f^2\left(\frac{\boldsymbol{p}+\boldsymbol{p}'}{2}\right)\left([\tau_0^{ik}][\tau_0^{jl}]^\dagger-[\tau_z^{ik}][\tau_z^{jl}]^\dagger+[\tau_x^{ik}][\tau_x^{jl}]^\dagger+[\tau_y^{ik}][\tau_y^{jl}]^\dagger\right)\\
&\left.\times\left(3[i\sigma_y^{\alpha\gamma}][i\sigma_y^{\beta\delta}]^\dagger+[(\boldsymbol{\sigma}i\sigma_y)^{\alpha\gamma}]\cdot[(\boldsymbol{\sigma}i\sigma_y)^{\beta\delta}]^\dagger\right)\right\}\\
&\times c^\dagger_{\boldsymbol{p}i\alpha}c^\dagger_{-\boldsymbol{p}k\gamma}c_{-\boldsymbol{p}'j\beta}c_{\boldsymbol{p}'l\delta}\,,
\end{aligned}$$

where we have dropped a term $6V\sum_{(\boldsymbol{p}i\alpha)}c^\dagger_{\boldsymbol{p}i\alpha}c_{\boldsymbol{p}i\alpha}$, which shifts the chemical potential.

The effective pairing interaction has spin-singlet channels $[i\sigma_y][i\sigma_y]^\dagger$ as well as spin-triplet pairing channels $[\boldsymbol{\sigma}i\sigma_y]\cdot[\boldsymbol{\sigma}i\sigma_y]^\dagger$, and we observe that the spin-singlet channels have the largest relative strength. As such, we expect spin-singlet interactions to drive superconductivity and we drop the spin-triplet terms here to simplify our analysis. Then, noting the attractive τ_z channel, we focus on the A_{1g} and B_{2g} pairing channels; looking at table 5.2, we see that only these two pairing channels have a spin-singlet gap function with a τ_z orbital component. As both of these channels also couple to a second spin-singlet component, we include this factor in the effective interaction as well. Including these terms, we find an effective pairing potential which can be written as

$$\begin{aligned}
V_{s_1s_2s_3s_4}(\boldsymbol{k},\boldsymbol{k}')=&\left[\frac{3V}{4}f^2\left(\frac{\boldsymbol{k}+\boldsymbol{k}'}{2}\right)+\frac{U}{8}\right][\tau_0 i\sigma_y]_{s_1s_2}[\tau_0 i\sigma_y]^\dagger_{s_3s_4}\\
&-\left[\frac{3V}{4}f^2\left(\frac{\boldsymbol{k}+\boldsymbol{k}'}{2}\right)-\frac{U}{8}\right][\tau_z i\sigma_y]_{s_1s_2}[\tau_z i\sigma_y]^\dagger_{s_3s_4}
\end{aligned}$$

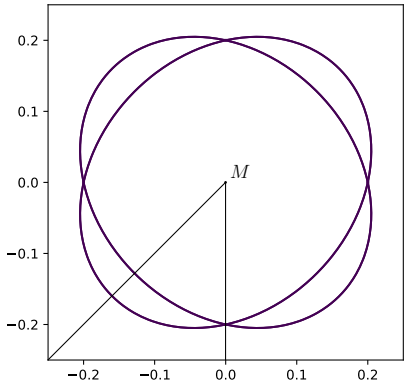

Figure 5.1: Fermi surfaces without spin-orbit coupling. The surfaces form two ellipses, with major axes at right angles to each other. The solution of the gap equation is simplified by circularizing these ellipses.

5.1.2 SOLVING THE GAP EQUATION (NO SOC)

With the linearized gap equation from the previous section, eq. (5.1), we can calculate the critical temperature by finding the temperature at which the solution of the linearized gap equation is zero. We begin by considering the case without spin-orbit coupling, for which $H = \epsilon_0(\boldsymbol{k}) + \gamma_{xy}(\boldsymbol{k})\tau_z$. This Hamiltonian is already diagonal in spin and orbital space, so we write the energies of the bands as $\epsilon_\pm(\boldsymbol{k}) = \epsilon_0(\boldsymbol{k}) \pm \gamma_{xy}(\boldsymbol{k})$. If we then consider the form of the effective interaction, it is clear that the gap function also has the form $\Delta(\boldsymbol{k}) = [\Delta_0(\boldsymbol{k}) + \Delta_z(\boldsymbol{k})\tau_z]i\sigma_y$, so we write $\Delta_\pm(\boldsymbol{k}) = \Delta_0(\boldsymbol{k}) \pm \Delta_z(\boldsymbol{k})$ and can solve for each component of $\Delta(\boldsymbol{k})$ in eq. (5.1). This gives us

$$\Delta_\pm(\boldsymbol{k}) = -\frac{1}{\beta}\sum_{\boldsymbol{k}'\,\omega_n}\left[3Vf^2\left(\frac{\boldsymbol{k}+\boldsymbol{k}'}{2}\right)\frac{\Delta_\mp(\boldsymbol{k}')}{\epsilon_\mp^2(\boldsymbol{k}')+\omega_n^2} + \frac{U}{2}\frac{\Delta_\pm(\boldsymbol{k}')}{\epsilon_\pm^2(\boldsymbol{k}')+\omega_n^2}\right]$$

The sum over ω_n is accomplished in a standard way using contour integration in the complex plane. Having done the sum over ω_n, we are left with

$$\Delta_\pm(\boldsymbol{k}) = -\sum_{\boldsymbol{k}'}\left[3Vf^2\left(\frac{\boldsymbol{k}+\boldsymbol{k}'}{2}\right)\Delta_\mp(\boldsymbol{k}')\frac{\tanh(\beta\epsilon_\mp(\boldsymbol{k}')/2)}{2\epsilon_\mp(\boldsymbol{k}')} + \frac{U}{2}\Delta_\pm(\boldsymbol{k}')\frac{\tanh(\beta\epsilon_\pm(\boldsymbol{k}')/2)}{2\epsilon_\pm(\boldsymbol{k}')}\right],$$

In fig. 5.1, we show the normal state Fermi surfaces, which are elliptical without spin-orbit coupling. In the weak-coupling approximation, only the states near the Fermi energy participate in the

superconducting pairing interaction, which simplifies the solution of the gap equations. We can replace the sum over $\boldsymbol{k}'$ with an integral over $\boldsymbol{k}'$. Then, we can rotate the coordinate system to align its axes with the major axes of each ellipse, and rescale the coordinate systems to circularize the Fermi surfaces. Because the ellipses are at right angles to each other, this scaling takes the form $(k_x, k_y) \to \left(\frac{k_x}{\eta}, \eta k_y\right)$ on one band, with $(k_x, k_y) \to \left(\eta k_x, \frac{k_y}{\eta}\right)$ on the other.

Having circularized the Fermi surfaces, it is appropriate to use the polar coordinates (k, ϕ), for which the integral over the magnitude of the momentum can be converted into an integral over the energy using $\epsilon = k^2/2m - \mu$. As a result, we find

$$\Delta_\pm(\phi_\pm) = -\oint \frac{\mathrm{d}\phi_\mp}{2\pi} \left(3Vf^2(\phi_+, \phi_-)\Delta_\mp(\phi_\mp) + \frac{U}{2}\Delta_\pm(\phi_\mp)\right) \left(N_0 \int_0^{\epsilon_c} \frac{\tanh(\beta_c\epsilon/2)}{2\epsilon}\,\mathrm{d}\epsilon\right) \tag{5.4}$$

In eq. (5.4), we have set $k = k_F$ in Δ and f because the only contributions to this integral come near the circular Fermi surface, owing to the integral over ϵ. The integral over ϵ is a standard form, and gives the result

$$\int_0^{\epsilon_c} \frac{\tanh(\frac{\beta_c\epsilon}{2})}{2\epsilon}\,\mathrm{d}\epsilon = \ln\left(\frac{2\epsilon_c e^\gamma}{\pi k_B T_c}\right),$$

where γ is the Euler-Mascheroni constant ($\gamma \approx 0.577$). We will let $N_0 \ln(2\epsilon_c e^\gamma/\pi k_B T_c) = \frac{1}{\lambda}$ and choose units so that $V = 1/3$ and $\widetilde{U} = U/3V$. Using these definitions, we find

$$\lambda\Delta_\pm(\phi_\pm) = -\oint \frac{\mathrm{d}\phi_\mp}{2\pi} f^2(\phi_+, \phi_-)\Delta_\mp(\phi_\mp) - \frac{\widetilde{U}}{2}\oint \frac{\mathrm{d}\phi_\mp}{2\pi}\Delta_\pm(\phi_\mp)\,. \tag{5.5}$$

Recalling that the form factor was written $f(\boldsymbol{k}) = 1 + \alpha(\boldsymbol{k}^2/k_0^2)$ and following the various transformations to arrive at eq. (5.5), we can write

$$f^2(\phi_+, \phi_-) = A_{00} - A_{02}(\cos 2\phi_+ - \cos 2\phi_-) + A_{22}\cos 2\phi_+ \cos 2\phi_- + A_{04}(\cos 4\phi_+ + \cos 4\phi_-)\,.$$

We can then express the gap function in terms of the harmonics which would survive integration:

$$\Delta_\pm(\phi) = \Delta_{0\pm} + \Delta_{2\pm}\cos(2\phi) + \Delta_{4\pm}\cos(4\phi) \tag{5.6}$$

The resulting gap equations are

$$\begin{aligned}
\lambda\Delta_{0\pm} &= -A_{00}\Delta_{0\mp} \mp \frac{A_{02}}{2}\Delta_{2\mp} - \frac{A_{04}}{2}\Delta_{4\mp} - \frac{\widetilde{U}}{2}\Delta_{0\pm} \\
\lambda\Delta_{2\pm} &= \pm A_{02}\Delta_{0\mp} - \frac{A_{22}}{2}\Delta_{2\mp} \\
\lambda\Delta_{4\pm} &= -A_{04}\Delta_{0\mp}\,.
\end{aligned}$$

Unfortunately, these gap equations are not symmetric, but a regularization procedure can make them symmetric. The issue is that $\int_T \cos^2(n\theta)\,\mathrm{d}\theta = \frac{T}{2}$ unless $n = 0$, so we have expanded the gap functions in an orthogonal but not properly normalized basis. If we properly normalize by letting $\widetilde{\Delta}_{0\pm} = \sqrt{2\pi}\Delta_{0\pm}$, $\widetilde{\Delta}_{2\pm} = \sqrt{\pi}\Delta_{2\pm}$, and $\widetilde{\Delta}_{4\pm} = \sqrt{\pi}\Delta_{4\pm}$, then the gap equations are

$$\begin{aligned}
\lambda\widetilde{\Delta}_{0\pm} &= -A_{00}\widetilde{\Delta}_{0\mp} \mp \frac{A_{02}}{\sqrt{2}}\widetilde{\Delta}_{2\mp} - \frac{A_{04}}{\sqrt{2}}\widetilde{\Delta}_{4\mp} - \frac{\widetilde{U}}{2}\widetilde{\Delta}_{0\pm} \\
\lambda\widetilde{\Delta}_{2\pm} &= \pm\frac{A_{02}}{\sqrt{2}}\widetilde{\Delta}_{0\mp} - \frac{A_{22}}{2}\widetilde{\Delta}_{2\mp} \\
\lambda\widetilde{\Delta}_{4\pm} &= -\frac{A_{04}}{\sqrt{2}}\widetilde{\Delta}_{0\mp}
\end{aligned}$$

We observe that the gap on one band is coupled to the gap on the other band. Looking back to eq. (5.6) in light of table 5.2 (taking care not to forget the $\pi/4$ rotation performed during the circularization of the elliptical Fermi surfaces), we can determine how Δ_{j+} should relate to Δ_{j-} for the A_{1g} (s-wave) and B_{2g} (d-wave) cases. For instance, we observe that $\Delta_{0+} = \Delta_{0-}$ for the s-wave state, while $\Delta_{0+} = -\Delta_{0-}$ for the d-wave state. In light of this, we make the following change of basis:

$$\begin{aligned}
\Delta_{0s} &= \frac{1}{\sqrt{2}}\left(\widetilde{\Delta}_{0+} + \widetilde{\Delta}_{0-}\right) & \Delta_{0d} &= \frac{1}{\sqrt{2}}\left(\widetilde{\Delta}_{0+} - \widetilde{\Delta}_{0-}\right) \\
\Delta_{2s} &= \frac{1}{\sqrt{2}}\left(\widetilde{\Delta}_{2+} - \widetilde{\Delta}_{2-}\right) & \Delta_{2d} &= \frac{1}{\sqrt{2}}\left(\widetilde{\Delta}_{2+} + \widetilde{\Delta}_{2-}\right) \\
\Delta_{4s} &= \frac{1}{\sqrt{2}}\left(\widetilde{\Delta}_{2+} + \widetilde{\Delta}_{2-}\right) & \Delta_{4d} &= \frac{1}{\sqrt{2}}\left(\widetilde{\Delta}_{2+} - \widetilde{\Delta}_{2-}\right)
\end{aligned}$$

This allows us to separate the gap equations for the A_{1g} and B_{2g} orders, finding (in matrix form)

$$\begin{pmatrix} -\left(\frac{\widetilde{U}}{2}+A_{00}\right) & \frac{A_{02}}{\sqrt{2}} & -\frac{A_{04}}{\sqrt{2}} \\ \frac{A_{02}}{\sqrt{2}} & \frac{A_{22}}{2} & 0 \\ -\frac{A_{04}}{\sqrt{2}} & 0 & 0 \end{pmatrix} \begin{pmatrix} \Delta_{0s} \\ \Delta_{2s} \\ \Delta_{4s} \end{pmatrix} = \lambda_s \begin{pmatrix} \Delta_{0s} \\ \Delta_{2s} \\ \Delta_{4s} \end{pmatrix}$$

$$\begin{pmatrix} -\left(\frac{\widetilde{U}}{2}-A_{00}\right) & -\frac{A_{02}}{\sqrt{2}} & \frac{A_{04}}{\sqrt{2}} \\ -\frac{A_{02}}{\sqrt{2}} & -\frac{A_{22}}{2} & 0 \\ \frac{A_{04}}{\sqrt{2}} & 0 & 0 \end{pmatrix} \begin{pmatrix} \Delta_{0d} \\ \Delta_{2d} \\ \Delta_{4d} \end{pmatrix} = \lambda_d \begin{pmatrix} \Delta_{0d} \\ \Delta_{2d} \\ \Delta_{4d} \end{pmatrix}$$

If we assume $A_{04} \ll 1$ (a reasonable assumption given our model), we can reduce this to solving 2×2 blocks. The eigenvalues for these are

$$\lambda_{s\pm} = \frac{-(\widetilde{U} - A_{22} + 2A_{00}) \pm \sqrt{(\widetilde{U} + A_{22} + 2A_{00})^2 + 8A_{02}^2}}{4}$$

$$\lambda_{d\pm} = \frac{-(\widetilde{U} - A_{22} - 2A_{00}) \pm \sqrt{(\widetilde{U} + A_{22} - 2A_{00})^2 + 8A_{02}^2}}{4}$$

The state with the highest critical temperature has the leading instability and will therefore be the superconducting ground state. Recalling that $N_0 \ln(2\epsilon_c e^\gamma/\pi k_B T_c) = 1/\lambda$, we observe that the highest T_c belongs to the state with the largest eigenvalue λ. We find that $\lambda_{d+} > \lambda_{s+}$ provided $A_{00} > 0$ and $|A_{02}| > 0$, which turns out to be the case for our model.

While not allowed for in our model, if we could drive the A_{00} negative the s-wave state would become preferred. This would be similar to having some type of constant, attractive, potential, as in the usual BCS theory for a single band. Furthermore, we observe that if A_{22} can be driven negative, then the tendency is to destroy superconductivity. Finally, we see that in this model the critical temperature for the s-wave and the d-wave become degenerate when $A_{02} \to 0$; since the term A_{02} ultimately arises from the fact that we started with elliptical—rather than circular—Fermi surfaces, this seems to indicate that the shape of the Fermi surface plays a role in determining the symmetry of the order parameter.

5.1.3 SPIN-ORBIT COUPLING

The linearized gap equation, eq. (5.1), is still valid when spin-orbit coupling is included in the Hamiltonian. However, the normal state Hamiltonian is no longer diagonal in either spin or orbital space, and subsequently, neither is $G^0(\boldsymbol{k}, \omega_n) = [i\omega_n - H(\boldsymbol{k})]^{-1}$. Using the same effective interaction, the gap equations in the presence of spin-orbit coupling are

$$\Delta_\pm = -\frac{1}{\beta}\sum_{\boldsymbol{k}'\,\omega_n} 3Vf^2(\boldsymbol{k},\boldsymbol{k}')\frac{(\epsilon_\pm^2+\omega_n^2)\Delta_\mp - (\gamma_x^2-\gamma_y^2)\Delta_\pm}{(E_+^2+\omega_n^2)(E_-^2+\omega_n^2)} + \frac{U}{2}\frac{(\epsilon_\mp^2+\omega_n^2)\Delta_\pm - (\gamma_x^2-\gamma_y^2)\Delta_\mp}{(E_+^2+\omega_n^2)(E_-^2+\omega_n^2)},$$

where $\epsilon_\pm = \epsilon_0 \pm \gamma_{xy}$ (as before), and where $E_\pm = \epsilon_0 \pm \gamma_k$ is the normal state dispersion relation, with $\gamma_k^2 = \gamma_x^2 + \gamma_y^2 + \gamma_{xy}^2$. We can use the same method as before to perform the sum over ω_n to find

$$\begin{aligned}
\Delta_\pm = \sum_{\boldsymbol{k}'}\Bigg[&\Bigg\{\left[3Vf^2(\boldsymbol{k},\boldsymbol{k}')(\epsilon_\pm^2 - E_+^2) - \frac{U}{2}(\gamma_x^2-\gamma_y^2)\right]\Delta_\mp \\
&- \left[3Vf^2(\boldsymbol{k},\boldsymbol{k}')(\gamma_x^2-\gamma_y^2) - \frac{U}{2}(\epsilon_\mp^2 - E_+^2)\right]\Delta_\pm\Bigg\}\frac{\tanh(\beta E_+/2)}{8\epsilon_0\gamma_k E_+} \\
&-\Bigg\{\left[3Vf^2(\boldsymbol{k},\boldsymbol{k}')(\epsilon_\pm^2 - E_-^2) - \frac{U}{2}(\gamma_x^2-\gamma_y^2)\right]\Delta_\mp \\
&- \left[3Vf^2(\boldsymbol{k},\boldsymbol{k}')(\gamma_x^2-\gamma_y^2) - \frac{U}{2}(\epsilon_\mp^2 - E_-^2)\right]\Delta_\pm\Bigg\}\frac{\tanh(\beta E_-/2)}{8\epsilon_0\gamma_k E_-}\Bigg]
\end{aligned}$$

For legibility, the $\boldsymbol{k}$ dependence of each term is suppressed; in the sum over $\boldsymbol{k}'$, only $f(\boldsymbol{k},\boldsymbol{k}')$ depends on $\boldsymbol{k}$ while all other functions depend on $\boldsymbol{k}'$. We can recover the result from the case without spin-orbit coupling by considering the limit $v_{\text{so}} \to 0$; this has the effect of sending $\gamma_x, \gamma_y \to 0$, $\gamma_k \to \gamma_{xy}$ and $E_\pm \to \epsilon_\pm$.

When spin-orbit coupling was not present, we were able to circularize the Fermi surface, which allowed us to find analytic solutions to the gap equations. However, in the presence of spin orbit coupling, the ellipses hybridize and form an inner and outer pocket, as shown in fig. 5.2. At present, the effort to solve the gap equations when spin-orbit coupling is included is ongoing.

5.2 GAP FEATURES

We turn now to look at the features of the A_{1g} and B_{2g} gap functions. Using the normal state Hamiltonian and the gap functions derived in section 5.1, we can find the quasiparticle dispersion

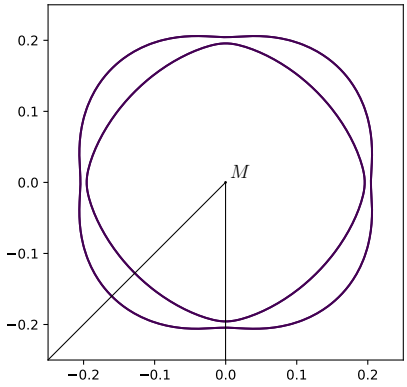

Figure 5.2: Fermi surface with spin-orbit coupling. The Fermi surface without spin-orbit coupling is shown (grey, dashed) as a guide. Hybridization between the two surfaces forms an inner and outer pocket.

from the eigenvalues of the Bogoliubov-de Gennes Hamiltonian,

$$H_{\mathrm{BdG}}(\boldsymbol{k}) = \begin{pmatrix} \epsilon_0 + \gamma_{xy}\tau_z + \tau_x(\gamma_y\sigma_x + \gamma_x\sigma_y) & (\Delta_0 + \Delta_z\tau_z)i\sigma_y \\ -(\Delta_0 + \Delta_z\tau_z)i\sigma_y & -\epsilon_0 - \gamma_{xy}\tau_z + \tau_x(\gamma_y\sigma_x - \gamma_x\sigma_y) \end{pmatrix}.$$

Note that for the A_{1g} gap, $\Delta_0 = \Delta_s$ is a constant, while $\Delta_z = \Delta_d \frac{k_x k_y}{k_0^2}$; whereas for the B_{2g} gap, $\Delta_z = \Delta_s$ is a constant while $\Delta_0 = \Delta_d \frac{k_x k_y}{k_0^2}$. The quasiparticle dispersion is given by

$$E_\pm = \sqrt{\epsilon_0^2 + \gamma_k^2 + \Delta_0^2 + \Delta_z^2 \pm 2\sqrt{(\epsilon_0\gamma_{xy} + \Delta_0\Delta_z)^2 + (\gamma_x^2 + \gamma_y^2)(\epsilon_0^2 + \Delta_z^2)}}\,, \tag{5.7}$$

and given the particle-hole symmetry we also have states at $-E_\pm$.

To better understand the role of spin-orbit coupling, we begin by considering the zero-coupling limit $v_{\mathrm{so}} \to 0$. The quasiparticle dispersion reduces to

$$E_\pm = \sqrt{(\epsilon_0 \pm \gamma_{xy})^2 + (\Delta_0 \pm \Delta_z)^2}\,.$$

In this limit, we see that the dispersion for the A_{1g} gap is indistinguishable from the dispersion for the B_{2g} gap. Furthermore, the gap can be either nodal or nodeless, depending on whether $(\Delta_0 \pm \Delta_z)$ goes to zero on the Fermi surface, where $\epsilon_0 \pm \gamma_{xy} = 0$. We find that the gap will be nodeless only when $-2(1 + am) < \Delta_d/\Delta_s < 2(1 - am)$—recalling that $\epsilon_0 = \frac{k^2}{2m} - \mu$ and $\gamma_{xy} = ak_xk_y$. In the limit

$\Delta_s \to 0$, the gap always has nodes along the $k_x = 0$ and $k_y = 0$ axes, as would be expected for a single band d_{xy}-wave superconductor.

For $\Delta_d/\Delta_s = 2(1 - am)$, we find that nodes appear on the elliptical Fermi surfaces along the major axes of of each ellipse, and as $\Delta_d/\Delta_s \to +\infty$, the nodes split and travel along the Fermi surface toward the $k_x = 0$ and $k_y = 0$ axes. Similarly, for $\Delta_d/\Delta_s = -2(1 + am)$, nodes appear on the elliptical Fermi surfaces along the minor axes of each ellipse, and as $\Delta_d/\Delta_s \to -\infty$, the nodes again split and travel along the Fermi surface toward the $k_x = 0$ and $k_y = 0$ axes.

We also observe that, without spin-orbit coupling, the gap is anisotropic but does not feature multiple peaks in the density-of-states. The E_+ gap is above the $\epsilon + \gamma_{xy}$ Fermi surface, while the E_- gap is above the $\epsilon_0 - \gamma_{xy}$ Fermi surface. These gaps are equal in magnitude upon a four-fold rotation, and so their contribution to the density-of-states occurs at the same energies for each band. In order to account for the gap features observed experimentally, we must therefore include spin-orbit coupling. This allows the normal state bands to interact, which ultimately results in the unconventional interband pairing in the superconducting state.

Including the effects from spin-orbit coupling also enables us to distinguish between the A_{1g} and B_{2g} gaps. For instance, we observe that along the usual nodal direction for a d_{xy}-wave superconductor such as $k_x = 0$, the B_{2g} dispersion becomes

$$E_\pm^{B_{2g}} = \sqrt{\epsilon_0^2 + \Delta_s^2} \pm \gamma_y \,.$$

Along this direction, the Fermi surface occurs at $\epsilon_0 \pm \gamma_y$, so it is clear that there are no nodes on the Fermi surface. However, for large enough $v_{\rm so}$, the gap is nodal. This is clearly the case at $k_y = k_0$ provided $|v_{\rm so}| \geq \frac{\Delta_s}{k_0} = 55\,\text{meV\AA}$. In fact, nodes develop away from k_0 (and between the Fermi surfaces) starting at the slightly smaller value of

$$|v_{\rm so}| \geq \frac{k_0}{m} \left(\frac{\left| 1 - \sqrt{1 + \frac{\Delta_s}{\mu}} \right|}{2} \right)^{1/2} \approx 54.73\,\text{meV\AA}$$

However, along the same direction, the A_{1g} dispersion becomes

$$E_\pm^{A_{1g}} = \sqrt{(\epsilon_0 \pm \gamma_y)^2 + \Delta_s^2} \,,$$

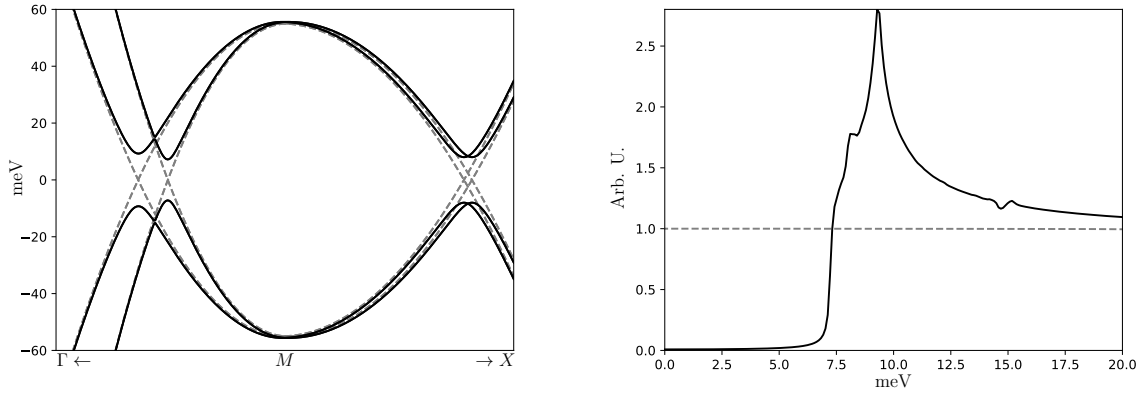

Figure 5.3: The band structure and density of states for the A_{1g} gap, using $\Delta_d = -2\,\text{meV}$, $\Delta_s = 8\,\text{meV}$, and $v_{\text{so}} = 12\,\text{meVÅ}$. On the left, the dashed lines show the particle/hole normal state dispersion from our normal state Hamiltonian. We observer that the gap minimum stays above the Fermi surface. The density of states on the right was calculated using the triangle method for the normal state (grey dashed line) and the superconducting state.

which never exhibits nodes. Experimentally, nodes are not observed so we must have either an A_{1g} gap, or $v_{\text{so}} < 54.73\,\text{meVÅ}$. Because the hybridization demonstrated in fig. 4.2 is not observed, we have $v_{\text{so}} < 15\,\text{meVÅ}$, so the model is in a regime where both the A_{1g} and B_{2g} gaps are nodeless.

The main qualitative distinction between the A_{1g} and B_{2g} gaps in our model is that interband pairing does not occur along the $k_x = 0$ or $k_y = 0$ directions for the A_{1g} gap, but does occur in this direction for the B_{2g} gap. This manifests as backbending for the A_{1g} case, while for the B_{2g} gap, the gap minimum in this direction actually occurs between the hybridized Fermi surfaces. However, since the hybridization from spin-orbit coupling has not been observed, backbending—or the lack thereof—cannot currently be used to distinguish the gap symmetry.

We plot the quasiparticle band structure and the density of states for the A_{1g} and B_{2g} gaps in figs. 5.3 and 5.4. We find that the main features in the density of states for both the A_{1g} and B_{2g} gaps arise from the $k_x = k_y$ (and symmetry equivalent) direction. Due to the d-wave like contribution, $\Delta_d \frac{k_x k_y}{k_0^2}$, the gap is anisotropic and the gap minimum, which is along the $k_x = 0$ direction, has positive curvature locally. As peaks in the density of states arise from saddle-points in the quasiparticle band structure, there is no peak in the density of states corresponding to the gap minimum. However, along the $k_x = k_y$ direction, there occur three saddle-points in the quasiparticle band structure where the curvature of the bands is positive radially, but negative tangentially. Along

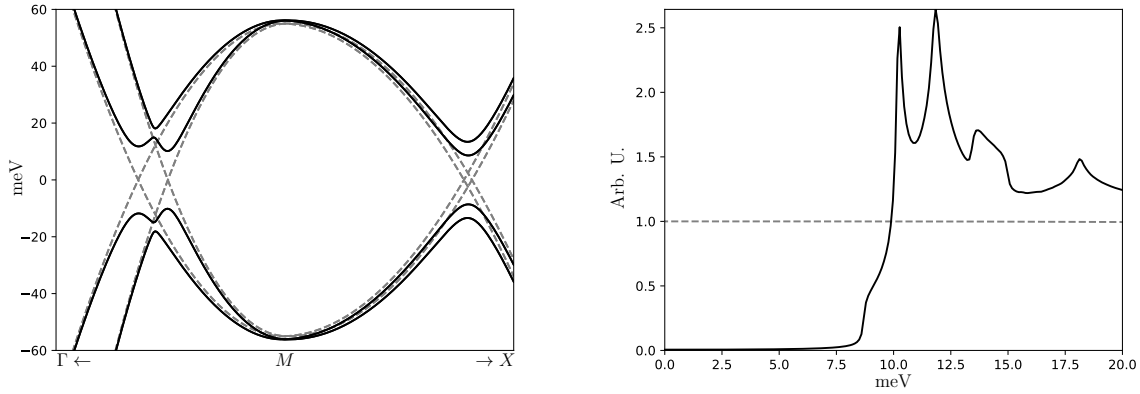

Figure 5.4: The band structure and density of states for the B_{2g} gap, using $\Delta_d = -1.5\,\text{meV}$, $\Delta_s = 11\,\text{meV}$, and $v_{\text{so}} = 12\,\text{meV\AA}$. The intraband pairing precludes identification of the a gap with the inner and outer pockets, despite these being fully separated by spin-orbit coupling induced hybridization.

E_+, the saddle-point occurs at the gap minimum in the $k_x = k_y$ direction, which lies between the two Fermi surfaces and produces a peak at $\sim 15\,\text{eV}$. This peak arises from interband pairing alone and is sensitive to the strength of both v_{so} and Δ_z for both the A_{1g} and B_{2g} gaps.

Along E_-, there are two saddle-points which occur at the gap minimum for each band along the $k_x = k_y$ direction. The relative difference in energy between these two minima is sensitive to the anisotropic gap contribution, which takes the form of intraband pairing for the B_{2g} gap, but which takes the form of interband pairing for the A_{1g} gap. Both features contribute a peak in the $8 - 10\,\text{meV}$ range, but may overlap if the radial anisotropy is not strong.

5.3 DISCUSSION

We were able to construct gap functions using the same group theoretic procedure for constructing the low-energy effective Hamiltonian. In doing so, we found that the only inversion-symmetry preserving gap functions that would support a nodeless gap belonged to the A_{1g} and B_{2g} representations. This broad classification also identified additional pairing modes which include spin-triplet terms; considering the impact of these triplet pairing terms could provide a better understanding of the similarities and differences between the A_{1g} and B_{2g} states in this model.

Furthermore, we developed a spin-fluctuation model for the pairing interaction in the presence

of an on-site Hubbard repulsion. While solving the gap equations with this interaction is an ongoing work, we are able to show that the B_{2g} d-wave state is favored when there is no spin-orbit coupling. This suggests that the B_{2g} state is favored for small spin-orbit coupling as well, but the investigation remains open to determine if this remains the case with increasing spin-orbit coupling strength, or if the A_{1g} state becomes favored. Given the results of Böker *et al.* [98], we expect the latter. Completing the investigation in the presence of spin-orbit coupling would also allow us to consider whether an external magnetic field could similarly drive a transition between the A_{1g} and B_{2g} states.

Finally, we investigated the A_{1g} and B_{2g} gaps to determine if our model replicated the anisotropic, nodeless, double-gap that has been observed in monolayer FeSe. Broadly speaking, our model does replicate the observed peaks, however further work needs to be done to provide a measurable fingerprint to identify the gap symmetry. Additionally, the work of Eugenio and Vafek [97] suggests that we should not neglect the spin-triplet terms. Despite this, we have shown that the non-conventional interband pairing plays an important role in understanding the superconductivity of FeSe and the iron-based superconductors.

BIBLIOGRAPHY

[1] H. Kamerlingh Onnes, "The resistance of pure mercury at helium temperatures," *Commun. Phys. Lab. Univ. Leiden, b*, vol. 120, 1911.

[2] W. Meissner and R. Ochsenfeld, "Ein neuer Effekt bei Eintritt der Supraleitfähigkeit," *Naturwissenschaften*, vol. 21, pp. 787–788, Nov. 1933.

[3] J. Bardeen, L. N. Cooper, and J. R. Schrieffer, "Microscopic Theory of Superconductivity," *Phys. Rev.*, vol. 106, pp. 162–164, Apr. 1957.

[4] J. Bardeen, L. N. Cooper, and J. R. Schrieffer, "Theory of Superconductivity," *Phys. Rev.*, vol. 108, pp. 1175–1204, Dec. 1957.

[5] L. N. Cooper, "Bound Electron Pairs in a Degenerate Fermi Gas," *Phys. Rev.*, vol. 104, pp. 1189–1190, Nov. 1956.

[6] W. Kohn and J. M. Luttinger, "New Mechanism for Superconductivity," *Phys. Rev. Lett.*, vol. 15, pp. 524–526, Sept. 1965.

[7] M. Sigrist and K. Ueda, "Phenomenological theory of unconventional superconductivity," *Reviews of Modern Physics*, vol. 63, pp. 239–311, Apr. 1991.

[8] J. G. Bednorz and K. A. Müller, "Possible high T_c superconductivity in the Ba-La-Cu-O system," *Z. Physik B - Condensed Matter*, vol. 64, pp. 189–193, June 1986.

[9] C. E. Gough, M. S. Colclough, E. M. Forgan, R. G. Jordan, M. Keene, C. M. Muirhead, A. I. M. Rae, N. Thomas, J. S. Abell, and S. Sutton, "Flux quantization in a high-T_c superconductor," *Nature*, vol. 326, no. 6116, pp. 855–855, 1987.

[10] C. C. Tsuei, J. R. Kirtley, C. C. Chi, L. S. Yu-Jahnes, A. Gupta, T. Shaw, J. Z. Sun, and M. B. Ketchen, "Pairing Symmetry and Flux Quantization in a Tricrystal Superconducting Ring of $YBa_2Cu_3O_{7-\delta}$," *Physical Review Letters*, vol. 73, pp. 593–596, July 1994.

[11] C. C. Tsuei, J. R. Kirtley, M. Rupp, J. Z. Sun, A. Gupta, M. B. Ketchen, C. A. Wang, Z. F. Ren, J. H. Wang, and M. Bhushan, "Pairing Symmetry in Single-Layer Tetragonal $Tl_2Ba_2CuO_{\beta+\delta}$ Superconductors," *Science*, vol. 271, pp. 329–332, Jan. 1996.

[12] Y. Zhang, L. X. Yang, M. Xu, Z. R. Ye, F. Chen, C. He, H. C. Xu, J. Jiang, B. P. Xie, J. J. Ying, X. F. Wang, X. H. Chen, J. P. Hu, M. Matsunami, S. Kimura, and D. L. Feng, "Nodeless superconducting gap in $A_xFe_2Se_2$ (A=K,Cs) revealed by angle-resolved photoemission spectroscopy," *Nature Materials*, vol. 10, pp. 273–277, Apr. 2011.

[13] M. Xu, Q. Q. Ge, R. Peng, Z. R. Ye, J. Jiang, F. Chen, X. P. Shen, B. P. Xie, Y. Zhang, A. F. Wang, X. F. Wang, X. H. Chen, and D. L. Feng, "Evidence for an s-wave superconducting gap in $K_xFe_{2-y}Se_2$ from angle-resolved photoemission," *Phys. Rev. B*, vol. 85, p. 220504, June 2012.

[14] D. Liu, W. Zhang, D. Mou, J. He, Y.-B. Ou, Q.-Y. Wang, Z. Li, L. Wang, L. Zhao, S. He, Y. Peng, X. Liu, C. Chen, L. Yu, G. Liu, X. Dong, J. Zhang, C. Chen, Z. Xu, J. Hu, X. Chen, X. Ma, Q. Xue, and X. Zhou, "Electronic origin of high-temperature superconductivity in single-layer FeSe superconductor," *Nature Communications*, vol. 3, p. 931, July 2012.

[15] J. J. Lee, F. T. Schmitt, R. G. Moore, S. Johnston, Y.-T. Cui, W. Li, M. Yi, Z. K. Liu, M. Hashimoto, Y. Zhang, D. H. Lu, T. P. Devereaux, D.-H. Lee, and Z.-X. Shen, "Interfacial mode coupling as the origin of the enhancement of T_c in FeSe films on $SrTiO_3$," *Nature*, vol. 515, pp. 245–248, Nov. 2014.

[16] Y. Zhang, J. J. Lee, R. G. Moore, W. Li, M. Yi, M. Hashimoto, D. H. Lu, T. P. Devereaux, D.-H. Lee, and Z.-X. Shen, "Superconducting Gap Anisotropy in Monolayer FeSe Thin Film," *Phys. Rev. Lett.*, vol. 117, p. 117001, Sept. 2016.

[17] Y. S. Kushnirenko, A. V. Fedorov, E. Haubold, S. Thirupathaiah, T. Wolf, S. Aswartham, I. Morozov, T. K. Kim, B. Büchner, and S. V. Borisenko, "Three-dimensional superconducting gap in FeSe from angle-resolved photoemission spectroscopy," *Physical Review B*, vol. 97, May 2018.

[18] L. C. Rhodes, M. D. Watson, A. A. Haghighirad, D. V. Evtushinsky, M. Eschrig, and T. K. Kim, "Scaling of the superconducting gap with orbital character in FeSe," *Phys. Rev. B*, vol. 98, p. 180503, Nov. 2018.

[19] Q. Fan, W. H. Zhang, X. Liu, Y. J. Yan, M. Q. Ren, R. Peng, H. C. Xu, B. P. Xie, J. P. Hu, T. Zhang, and D. L. Feng, "Plain s-wave superconductivity in single-layer FeSe on $SrTiO_3$ probed by scanning tunnelling microscopy," *Nature Physics*, vol. 11, pp. 946–952, Nov. 2015.

[20] Z. Du, X. Yang, H. Lin, D. Fang, G. Du, J. Xing, H. Yang, X. Zhu, and H.-H. Wen, "Scrutinizing the double superconducting gaps and strong coupling pairing in $(Li_{1-x}Fe_x)$OHFeSe," *Nature Communications*, vol. 7, p. 10565, Jan. 2016.

[21] C. Liu, J. Mao, H. Ding, R. Wu, C. Tang, F. Li, K. He, W. Li, C.-L. Song, X.-C. Ma, Z. Liu, L. Wang, and Q.-K. Xue, "Extensive impurity-scattering study on the pairing symmetry of monolayer FeSe films on $SrTiO_3$," *Physical Review B*, vol. 97, Jan. 2018.

[22] A. Chubukov and P. J. Hirschfeld, "Iron-based superconductors, seven years later," *Phys. Today*, vol. 68, pp. 46–52, June 2015.

[23] Q. Si, R. Yu, and E. Abrahams, "High-temperature superconductivity in iron pnictides and chalcogenides," *Nat. Rev. Mater.*, vol. 1, p. 16017, Mar. 2016.

[24] S. He, J. He, W. Zhang, L. Zhao, D. Liu, X. Liu, D. Mou, Y.-B. Ou, Q.-Y. Wang, Z. Li, L. Wang, Y. Peng, Y. Liu, C. Chen, L. Yu, G. Liu, X. Dong, J. Zhang, C. Chen, Z. Xu, X. Chen, X. Ma, Q. Xue, and X. J. Zhou, "Phase diagram and electronic indication of high-temperature superconductivity at 65 K in single-layer FeSe films," *Nat. Mater.*, vol. 12, pp. 605–610, July 2013.

[25] D.-H. Lee, "What makes the T_c of FeSe/$SrTiO_3$ so high?," *Chinese Phys. B*, vol. 24, p. 117405, Nov. 2015.

[26] Y. Miyata, K. Nakayama, K. Sugawara, T. Sato, and T. Takahashi, "High-temperature superconductivity in potassium-coated multilayer FeSe thin films," *Nature Materials*, vol. 14, pp. 775–779, Aug. 2015.

[27] S. Coh, M. L. Cohen, and S. G. Louie, "Large electron-phonon interactions from FeSe phonons in a monolayer," *New J. Phys.*, vol. 17, p. 073027, July 2015.

[28] G. R. Stewart, "Superconductivity in iron compounds," *Rev. Mod. Phys.*, vol. 83, pp. 1589–1652, Dec. 2011.

[29] J.-F. Ge, Z.-L. Liu, C. Liu, C.-L. Gao, D. Qian, Q.-K. Xue, Y. Liu, and J.-F. Jia, "Superconductivity above 100 K in single-layer FeSe films on doped $SrTiO_3$," *Nat. Mater.*, vol. 14, pp. 285–289, Nov. 2014.

[30] A. Martinelli, F. Bernardini, and S. Massidda, "The phase diagrams of iron-based superconductors: theory and experiments," *Comptes Rendus Physique*, vol. 17, pp. 5–35, Jan. 2016.

[31] T. M. McQueen, Q. Huang, V. Ksenofontov, C. Felser, Q. Xu, H. Zandbergen, Y. S. Hor, J. Allred, A. J. Williams, D. Qu, J. Checkelsky, N. P. Ong, and R. J. Cava, "Extreme sensitivity of superconductivity to stoichiometry in $Fe_{1\delta}Se$," *Phys. Rev. B*, vol. 79, p. 014522, Jan. 2009.

[32] H. Eschrig and K. Koepernik, "Tight-binding models for the iron-based superconductors," *Phys. Rev. B*, vol. 80, p. 104503, Sept. 2009.

[33] B. Bradlyn, L. Elcoro, J. Cano, M. G. Vergniory, Z. Wang, C. Felser, M. I. Aroyo, and B. A. Bernevig, "Topological quantum chemistry," *Nature*, vol. 547, pp. 298–305, July 2017.

[34] J. O'Halloran, D. F. Agterberg, M. X. Chen, and M. Weinert, "Stabilizing the spin vortex crystal phase in two-dimensional iron-based superconductors," *Physical Review B*, vol. 95, Feb. 2017.

[35] V. Cvetkovic and Z. Tesanovic, "Multiband magnetism and superconductivity in Fe-based compounds," *EPL*, vol. 85, no. 3, p. 37002, 2009.

[36] K. Kuroki, S. Onari, R. Arita, H. Usui, Y. Tanaka, H. Kontani, and H. Aoki, "Unconventional Pairing Originating from the Disconnected Fermi Surfaces of Superconducting $LaFeAsO_{1-x}F_x$," *Phys. Rev. Lett.*, vol. 101, p. 087004, Aug. 2008.

[37] F. Ahn, I. Eremin, J. Knolle, V. B. Zabolotnyy, S. V. Borisenko, B. Büchner, and A. V. Chubukov, "Superconductivity from repulsion in LiFeAs: Novel s -wave symmetry and potential time-reversal symmetry breaking," *Physical Review B*, vol. 89, Apr. 2014.

[38] Y. Wang, A. Kreisel, V. B. Zabolotnyy, S. V. Borisenko, B. Büchner, T. A. Maier, P. J. Hirschfeld, and D. J. Scalapino, "Superconducting gap in LiFeAs from three-dimensional spin-fluctuation pairing calculations," *Phys. Rev. B*, vol. 88, p. 174516, Nov. 2013.

[39] E. M. Nica, R. Yu, and Q. Si, "Glide reflection symmetry, Brillouin zone folding, and superconducting pairing for the $P4/nmm$ space group," *Phys. Rev. B*, vol. 92, no. 17, p. 174520, 2015.

[40] M. Yi, D. H. Lu, R. Yu, S. C. Riggs, J.-H. Chu, B. Lv, Z. K. Liu, M. Lu, Y.-T. Cui, M. Hashimoto, S.-K. Mo, Z. Hussain, C. W. Chu, I. R. Fisher, Q. Si, and Z.-X. Shen, "Observation of Temperature-Induced Crossover to an Orbital-Selective Mott Phase in $A_xFe_{2-y}Se_2$ (A=K, Rb) Superconductors," *Phys. Rev. Lett.*, vol. 110, p. 067003, Feb. 2013.

[41] M. Yi, Z.-K. Liu, Y. Zhang, R. Yu, J.-X. Zhu, J. J. Lee, R. G. Moore, F. T. Schmitt, W. Li, S. C. Riggs, J.-H. Chu, B. Lv, J. Hu, M. Hashimoto, S.-K. Mo, Z. Hussain, Z. Q. Mao, C. W. Chu, I. R. Fisher, Q. Si, Z.-X. Shen, and D. H. Lu, "Observation of universal strong orbital-dependent correlation effects in iron chalcogenides," *Nature Communications*, vol. 6, p. 7777, July 2015.

[42] K. v. Klitzing, G. Dorda, and M. Pepper, "New Method for High-Accuracy Determination of the Fine-Structure Constant Based on Quantized Hall Resistance," *Phys. Rev. Lett.*, vol. 45, pp. 494–497, Aug. 1980.

[43] R. B. Laughlin, "Quantized Hall conductivity in two dimensions," *Phys. Rev. B*, vol. 23, pp. 5632–5633, May 1981.

[44] D. J. Thouless, M. Kohmoto, M. P. Nightingale, and M. den Nijs, "Quantized Hall Conductance in a Two-Dimensional Periodic Potential," *Physical Review Letters*, vol. 49, pp. 405–408, Aug. 1982.

[45] M. Z. Hasan and C. L. Kane, "Colloquium: Topological insulators," *Reviews of Modern Physics*, vol. 82, pp. 3045–3067, Nov. 2010.

[46] X.-L. Qi and S.-C. Zhang, "Topological insulators and superconductors," *Rev. Mod. Phys.*, vol. 83, pp. 1057–1110, Oct. 2011.

[47] B. Bradlyn, L. Elcoro, M. G. Vergniory, J. Cano, Z. Wang, C. Felser, M. I. Aroyo, and B. A. Bernevig, "Band connectivity for topological quantum chemistry: Band structures as a graph theory problem," *Physical Review B*, vol. 97, Jan. 2018.

[48] P. Dai, J. Hu, and E. Dagotto, "Magnetism and its microscopic origin in iron-based high-temperature superconductors," *Nature Physics*, vol. 8, pp. 709–718, Oct. 2012.

[49] Q. Wang, Y. Shen, B. Pan, X. Zhang, K. Ikeuchi, K. Iida, A. D. Christianson, H. C. Walker, D. T. Adroja, M. Abdel-Hafiez, X. Chen, D. A. Chareev, A. N. Vasiliev, and J. Zhao, "Magnetic ground state of FeSe," *Nature Communications*, vol. 7, p. 12182, July 2016.

[50] J. Lorenzana, G. Seibold, C. Ortix, and M. Grilli, "Competing Orders in FeAs Layers," *Phys. Rev. Lett.*, vol. 101, p. 186402, Oct. 2008.

[51] P. M. R. Brydon, J. Schmiedt, and C. Timm, "Microscopically derived Ginzburg-Landau theory for magnetic order in the iron pnictides," *Phys. Rev. B*, vol. 84, p. 214510, Dec. 2011.

[52] M. N. Gastiasoro and B. M. Andersen, "Competing magnetic double-Q phases and superconductivity-induced reentrance of C_2 magnetic stripe order in iron pnictides," *Physical Review B*, vol. 92, Oct. 2015.

[53] G. Giovannetti, C. Ortix, M. Marsman, M. Capone, J. van den Brink, and J. Lorenzana, "Proximity of iron pnictide superconductors to a quantum tricritical point," *Nat. Commun.*, vol. 2, p. 398, July 2011.

[54] J. Kang, X. Wang, A. V. Chubukov, and R. M. Fernandes, "Interplay between tetragonal magnetic order, stripe magnetism, and superconductivity in iron-based materials," *Phys. Rev. B*, vol. 91, p. 121104(R), Mar. 2015.

[55] M. Hoyer, R. M. Fernandes, A. Levchenko, and J. Schmalian, "Disorder-promoted C_4-symmetric magnetic order in iron-based superconductors," *Phys. Rev. B*, vol. 93, no. 14, p. 144414, 2016.

[56] R. M. Fernandes, S. A. Kivelson, and E. Berg, "Vestigial chiral and charge orders from bidirectional spin-density waves: Application to the iron-based superconductors," *Phys. Rev. B*, vol. 93, p. 014511, Jan. 2016.

[57] M. H. Christensen, J. Kang, B. M. Andersen, I. Eremin, and R. M. Fernandes, "Spin reorientation driven by the interplay between spin-orbit coupling and Hund's rule coupling in iron pnictides," *Physical Review B*, vol. 92, Dec. 2015.

[58] W. R. Meier, Q.-P. Ding, A. Kreyssig, S. L. Bud'ko, A. Sapkota, K. Kothapalli, V. Borisov, R. Valentí, C. D. Batista, P. P. Orth, R. M. Fernandes, A. I. Goldman, Y. Furukawa, A. E. Böhmer, and P. C. Canfield, "Hedgehog spin-vortex crystal stabilized in a hole-doped iron-based superconductor," *npj Quantum Materials*, vol. 3, p. 5, Feb. 2018.

[59] Q.-P. Ding, W. R. Meier, J. Cui, M. Xu, A. E. Böhmer, S. L. Bud'ko, P. C. Canfield, and Y. Furukawa, "Hedgehog Spin-Vortex Crystal Antiferromagnetic Quantum Criticality in $CaK(Fe_{1-x}Ni_x)_4As_4$ Revealed by NMR," *Physical Review Letters*, vol. 121, Sept. 2018.

[60] Q.-P. Ding, W. R. Meier, A. E. Böhmer, S. L. Bud'ko, P. C. Canfield, and Y. Furukawa, "NMR study of the new magnetic superconductor $CaK(Fe_{0}.951Ni_{0}.049)_4As_4$: Microscopic coexistence of the hedgehog spin-vortex crystal and superconductivity," *Physical Review B*, vol. 96, Dec. 2017.

[61] F. Wang, S. A. Kivelson, and D.-H. Lee, "Nematicity and quantum paramagnetism in FeSe," *Nature Physics*, vol. 11, pp. 959–963, Nov. 2015.

[62] I. Eremin and A. V. Chubukov, "Magnetic degeneracy and hidden metallicity of the spin-density-wave state in ferropnictides," *Phys. Rev. B*, vol. 81, p. 024511, Jan. 2010.

[63] M. H. Christensen, J. Kang, B. M. Andersen, and R. M. Fernandes, "Spin-driven nematic instability of the multiorbital Hubbard model: Application to iron-based superconductors," *Phys. Rev. B*, vol. 93, p. 085136, Feb. 2016.

[64] S. V. Borisenko, D. V. Evtushinsky, Z.-H. Liu, I. Morozov, R. Kappenberger, S. Wurmehl, B. Büchner, A. N. Yaresko, T. K. Kim, M. Hoesch, and others, "Direct observation of spin-orbit coupling in iron-based superconductors," *Nat. Phys.*, vol. 12, no. 4, pp. 311–317, 2016.

[65] P. Steffens, C. H. Lee, N. Qureshi, K. Kihou, A. Iyo, H. Eisaki, and M. Braden, "Splitting of Resonance Excitations in Nearly Optimally Doped $Ba(Fe_{0}.94Co_{0}.06)_2As_2$: An Inelastic Neutron Scattering Study with Polarization Analysis," *Physical Review Letters*, vol. 110, Mar. 2013.

[66] M. Ma, P. Bourges, Y. Sidis, Y. Xu, S. Li, B. Hu, J. Li, F. Wang, and Y. Li, "Prominent Role of Spin-Orbit Coupling in FeSe Revealed by Inelastic Neutron Scattering," *Phys. Rev. X*, vol. 7, p. 021025, May 2017.

[67] V. Cvetkovic and O. Vafek, "Space group symmetry, spin-orbit coupling, and the low-energy effective Hamiltonian for iron-based superconductors," *Phys. Rev. B*, vol. 88, p. 134510, Oct. 2013.

[68] M. G. Kim, A. Kreyssig, A. Thaler, D. K. Pratt, W. Tian, J. L. Zarestky, M. A. Green, S. L. Bud'ko, P. C. Canfield, R. J. McQueeney, and A. I. Goldman, "Antiferromagnetic ordering in the absence of structural distortion in $Ba(Fe_{1-x}Mn_x)_2As_2$," *Phys. Rev. B*, vol. 82, p. 220503(R), Dec. 2010.

[69] E. Hassinger, G. Gredat, F. Valade, S. R. de Cotret, A. Juneau-Fecteau, J.-P. Reid, H. Kim, M. A. Tanatar, R. Prozorov, B. Shen, H.-H. Wen, N. Doiron-Leyraud, and L. Taillefer, "Pressure-induced Fermi-surface reconstruction in the iron-arsenide superconductor $Ba_{1-x}K_xFe_2As_2$: Evidence of a phase transition inside the antiferromagnetic phase," *Physical Review B*, vol. 86, Oct. 2012.

[70] S. Avci, O. Chmaissem, J. M. Allred, S. Rosenkranz, I. Eremin, A. V. Chubukov, D. E. Bugaris, D. Y. Chung, M. G. Kanatzidis, J.-P. Castellan, J. A. Schlueter, H. Claus, D. D. Khalyavin, P. Manuel, A. Daoud-Aladine, and R. Osborn, "Magnetically driven suppression of nematic order in an iron-based superconductor," *Nature Communications*, vol. 5, p. 3845, May 2014.

[71] J. M. Allred, K. M. Taddei, D. E. Bugaris, M. J. Krogstad, S. H. Lapidus, D. Y. Chung, H. Claus, M. G. Kanatzidis, D. E. Brown, J. Kang, R. M. Fernandes, I. Eremin, S. Rosenkranz, O. Chmaissem, and R. Osborn, "Double-Q spin-density wave in iron arsenide superconductors," *Nature Physics*, vol. 12, pp. 493–498, May 2016.

[72] J. M. Allred, S. Avci, D. Y. Chung, H. Claus, D. D. Khalyavin, P. Manuel, K. M. Taddei, M. G. Kanatzidis, S. Rosenkranz, R. Osborn, and O. Chmaissem, "Tetragonal magnetic phase in $Ba_{1-x}K_xFe_2As_2$ from x-ray and neutron diffraction," *Phys. Rev. B*, vol. 92, p. 094515, Sept. 2015.

[73] A. E. Böhmer, F. Hardy, L. Wang, T. Wolf, P. Schweiss, and C. Meingast, "Superconductivity-induced re-entrance of the orthorhombic distortion in $Ba_{1-x}K_xFe_2As_2$," *Nature Communications*, vol. 6, p. 7911, July 2015.

[74] D. F. Agterberg, T. Shishidou, J. O'Halloran, P. M. R. Brydon, and M. Weinert, "Resilient Nodeless d-Wave Superconductivity in Monolayer FeSe," *Phys. Rev. Lett.*, vol. 119, p. 267001, Dec. 2017.

[75] L. Elcoro, B. Bradlyn, Z. Wang, M. G. Vergniory, J. Cano, C. Felser, B. A. Bernevig, D. Orobengoa, G. de la Flor, and M. I. Aroyo, "Double crystallographic groups and their representations on the Bilbao Crystallographic Server," *Journal of Applied Crystallography*, vol. 50, pp. 1457–1477, Oct. 2017.

[76] B.-J. Yang and N. Nagaosa, "Classification of stable three-dimensional Dirac semimetals with nontrivial topology," *Nature Communications*, vol. 5, p. 4898, Sept. 2014.

[77] R. P. Day, G. Levy, M. Michiardi, B. Zwartsenberg, M. Zonno, F. Ji, E. Razzoli, F. Boschini, S. Chi, R. Liang, P. K. Das, I. Vobornik, J. Fujii, W. N. Hardy, D. A. Bonn, I. S. Elfimov, and A. Damascelli, "Influence of Spin-Orbit Coupling in Iron-Based Superconductors," *Phys. Rev. Lett.*, vol. 121, p. 076401, Aug. 2018.

[78] D. D. Scherer and B. M. Andersen, "Spin-Orbit Coupling and Magnetic Anisotropy in Iron-Based Superconductors," *Phys. Rev. Lett.*, vol. 121, p. 037205, July 2018.

[79] Q.-Y. Wang, Z. Li, W.-H. Zhang, Z.-C. Zhang, J.-S. Zhang, W. Li, H. Ding, Y.-B. Ou, P. Deng, K. Chang, J. Wen, C.-L. Song, K. He, J.-F. Jia, S.-H. Ji, Y.-Y. Wang, L.-L. Wang, X. Chen, X.-C. Ma, and Q.-K. Xue, "Interface-Induced High-Temperature Superconductivity in Single Unit-Cell FeSe Films on $SrTiO_3$," *Chin. Phys. Lett.*, vol. 29, no. 3, p. 037402, 2012.

[80] B. Rosenstein and B. Y. Shapiro, "High-temperature superconductivity in single unit cell layer FeSe due to soft phonons in the interface layer of the $SrTiO_3$ substrate," *Phys. Rev. B*, vol. 100, p. 054514, Aug. 2019.

[81] I. A. Nekrasov, N. S. Pavlov, and M. V. Sadovskii, "On the origin of the shallow and "replica" bands in FeSe monolayer superconductors," *Jetp Lett.*, vol. 105, pp. 370–374, Mar. 2017.

[82] J. Jandke, F. Yang, P. Hlobil, T. Engelhardt, D. Rau, K. Zakeri, C. Gao, J. Schmalian, and W. Wulfhekel, "Unconventional pairing in single FeSe layers," *Phys. Rev. B*, vol. 100, p. 020503, July 2019.

[83] A. V. Chubukov, D. V. Efremov, and I. Eremin, "Magnetism, superconductivity, and pairing symmetry in iron-based superconductors," *Physical Review B*, vol. 78, Oct. 2008.

[84] A. V. Chubukov, M. Khodas, and R. M. Fernandes, "Magnetism, Superconductivity, and Spontaneous Orbital Order in Iron-Based Superconductors: Which Comes First and Why?," *Phys. Rev. X*, vol. 6, p. 041045, Dec. 2016.

[85] A. K. C. Cheung and D. F. Agterberg, "Superconductivity in the presence of spin-orbit interactions stabilized by Hund coupling," *Phys. Rev. B*, vol. 99, p. 024516, Jan. 2019.

[86] H. Kotegawa, S. Masaki, Y. Awai, H. Tou, Y. Mizuguchi, and Y. Takano, "Evidence for Unconventional Superconductivity in Arsenic-Free Iron-Based Superconductor FeSe: A ^{77}Se-NMR Study," *Journal of the Physical Society of Japan*, vol. 77, pp. 113703–113703, Nov. 2008.

[87] Y. Sun, S. Kittaka, S. Nakamura, T. Sakakibara, K. Irie, T. Nomoto, K. Machida, J. Chen, and T. Tamegai, "Gap structure of FeSe determined by angle-resolved specific heat measurements in applied rotating magnetic field," *Physical Review B*, vol. 96, Dec. 2017.

[88] Y. Sun, S. Kittaka, S. Nakamura, T. Sakakibara, P. Zhang, S. Shin, K. Irie, T. Nomoto, K. Machida, J. Chen, and T. Tamegai, "Disorder-sensitive nodelike small gap in FeSe," *Physical Review B*, vol. 98, Aug. 2018.

[89] P. K. Biswas, A. Kreisel, Q. Wang, D. T. Adroja, A. D. Hillier, J. Zhao, R. Khasanov, J.-C. Orain, A. Amato, and E. Morenzoni, "Evidence of nodal gap structure in the basal plane of the FeSe superconductor," *Phys. Rev. B*, vol. 98, p. 180501, Nov. 2018.

[90] F. Hardy, M. He, L. Wang, T. Wolf, P. Schweiss, M. Merz, M. Barth, P. Adelmann, R. Eder, A.-A. Haghighirad, and C. Meingast, "Calorimetric evidence of nodal gaps in the nematic superconductor FeSe," *Phys. Rev. B*, vol. 99, p. 035157, Jan. 2019.

[91] M. Chen, Q. Tang, X. Chen, Q. Gu, H. Yang, Z. Du, X. Zhu, E. Wang, Q.-H. Wang, and H.-H. Wen, "Direct visualization of sign-reversal $s^{\pm}$ superconducting gaps in $FeTe_{0.55}Se_{0.45}$," *Phys. Rev. B*, vol. 99, p. 014507, Jan. 2019.

[92] Z. Ge, C. Yan, H. Zhang, D. Agterberg, M. Weinert, and L. Li, "Evidence for d-Wave Superconductivity in Single Layer FeSe/$SrTiO_3$ Probed by Quasiparticle Scattering Off Step Edges," *Nano Lett.*, vol. 19, pp. 2497–2502, Apr. 2019.

[93] A. Hinojosa and A. V. Chubukov, "Gap structure in Fe-based superconductors with accidental nodes: The role of hybridization," *Physical Review B*, vol. 91, no. 22, p. 224502, 2015.

[94] A. V. Chubukov, O. Vafek, and R. M. Fernandes, "Displacement and annihilation of Dirac gap nodes in d-wave iron-based superconductors," *Phys. Rev. B*, vol. 94, p. 174518, Nov. 2016.

[95] T. Nakayama, T. Shishidou, and D. F. Agterberg, "Nodal topology in d-wave superconducting monolayer FeSe," *Phys. Rev. B*, vol. 98, p. 214503, Dec. 2018.

[96] Z.-X. Li, F. Wang, H. Yao, and D.-H. Lee, "What makes the Tc of monolayer FeSe on $SrTiO_3$ so high: a sign-problem-free quantum Monte Carlo study," *Sci. Bull.*, vol. 61, pp. 925–930, June 2016.

[97] P. M. Eugenio and O. Vafek, "Classification of symmetry derived pairing at the M point in FeSe," *Physical Review B*, vol. 98, July 2018.

[98] J. Böker, P. A. Volkov, P. J. Hirschfeld, and I. Eremin, "Quasiparticle interference and symmetry of superconducting order parameter in strongly electron-doped iron-based superconductors," *New J. Phys.*, vol. 21, p. 083021, Aug. 2019.

[99] C. J. Bradley and A. P. Cracknell, *The mathematical theory of symmetry in solids: representation theory for point groups and space groups*. Oxford classic texts in the physical sciences, Oxford: Clarendon Press, 2010.

[100] C. Herring, "Character tables for two space groups," *Journal of the Franklin Institute*, vol. 233, pp. 525–543, June 1942.

Appendix A

FINITE GROUPS

In this appendix, we give a brief introduction to the study of groups and representations of groups, which plays a central role in the developments of the main text. Group theory is the abstraction of algebra, built upon set theory. In addition to a set of objects, we introduce some notion of combining two members of the set, the binary operation.

The majority of the results that we use from group theory come from the study of finite groups. We begin by introducing finite groups and then work towards determining the character table for D_{4h}. However, as this is not meant to be a textbook on group theory, we are presenting definitions and some theorems, but do not offer proofs.

A.1 FINITE GROUPS

The study of finite groups begins with finite sets. In this appendix, we generally consider abstract sets, but we will also consider D_{4h}, the symmetries of a square—more technically, the symmetries of a square cuboid.

Definition. A **group** $\langle G, * \rangle$ is a mathematical structure defined by a set G, and a binary operation, $*$, which acts on elements of that set, which satisfies the group axioms of closure, associativity, identity, and invertibility.

> **Closure**: A set G is **closed** under an operation $*$ if, and only if, for every $a, b \in G$, $a * b \in G$ as well.
>
> **Associativity**: An operation $*$ is **associative** in a set G if, and only if, for any $a, b, c \in G$, $a * (b * c) = (a * b) * c$.
>
> **Identity**: A set G contains an **identity** under the operation $*$ if, and only if, there exists some $e \in G$ such that for every $a \in G$, $a * e = e * a = a$.
>
> **Invertibility**: A set G is **invertible** under an operation $*$ if, and only if, G contains an identity under $*$, denoted e, and for every $a \in G$ there is some $b \in G$ such that $a * b = b * a = e$.

While a group is defined in terms of a set and a binary operation defined on that set, it is common practice to suppress the operation either when it is clear from context, or in the abstract when the particular label for the operation is not important. When this is done, we would refer to a group $\langle G, * \rangle$ as simply "the group G" and use element-wise juxtaposition to indicate the operation—that is, $a * b$ would be written as simply ab.

Note that a group G is not generally commutative—that is, given two elements $a, b \in G$, it is not generally true that $ab = ba$. Groups which have this property are known as **abelian**. For example, consider the two groups C_4 and D_2; C_4 is known as the cyclic group of order four, and can

C_4	E	C_4^+	C_2	C_4^-
E	E	C_4^+	C_2	C_4^-
C_4^+	C_4^+	C_2	C_4^-	E
C_2	C_2	C_4^-	E	C_4^+
C_4^-	C_4^-	E	C_4^+	C_2

D_2	E	σ_x	C_2	σ_y
E	E	σ_x	C_2	σ_y
σ_x	σ_x	E	σ_y	C_2
C_2	C_2	σ_y	E	σ_x
σ_y	σ_y	C_2	σ_x	E

Table A.1: Multiplication tables for C_4 and D_2.

be visualized as the (proper) rotations of a square. There are four elements: a rotation through 90° counter-clockwise (C_4^+), a rotation through 180° counter-clockwise (C_2), a rotation through 270° counter-clockwise (C_4^-), and a rotation through 360°, corresponding to no rotation or the identity (E). On the other hand, D_2 is a dihedral group, and can be observed as the symmetry group of a rectangle. There are again four elements: reflection across a mirror plane perpendicular to the vertical (σ_v), reflection across a mirror plane perpendicular to the horizontal (σ_h), rotation through 180° (C_2), and the identity (E). As both of these groups have four elements, they have **order** four, written $|G| = 4$.

The operation for these groups is composition. Performing the symmetry operation h followed by the operation g results in the operation gh. For finite groups, we can display the results of the operation between any pair of elements with the group table, as shown in table A.1, from which we observe that C_4 and D_2 are both abelian.

It is often useful to describe a group in terms of its generators and what are known as generating relations, which are expressions of the orders of the generators and products of the generators. A group can be identified uniquely by the group table, or instead by the generators and generating relations, with the latter being more economical to write down. Furthermore, by expressing a group in terms of its generators, we can for example verify that a Hamiltonian is invariant under all group operations if we can show it is invariant under only the generators. C_4 is an example of a **cyclic** group; the group can be generated by a single element, such as C_4^+, which has the generating relation $(C_4^+)^4 = E$. Meanwhile, D_2 is generated by two elements, such as σ_x, σ_y, with the generating relations $\sigma_x^2 = \sigma_y^2 = (\sigma_x\sigma_y)^2 = E$.

Upon inspection, it is clear that D_2 and C_4 should be different groups, but in order to make this notion rigorous, we need a way to compare two groups. This is done by considering certain "well-behaved" functions which preserve the structure of the group in some sense. We shall call such well-behaved functions **homomorphisms**.

Definition. Given groups G and H, the function $f : G \to H$ is a **homomorphism** if, and only if, $f(a)f(b) = f(ab)$.

To be explicit with the operation in each group, let $\langle G, * \rangle$ and $\langle H, \times \rangle$ be groups, and $f : G \to H$ be a homomorphism. Then f has the property that $f(a) \times f(b) = f(a * b)$; since $a, b \in G$, $a * b \in G$, while $f(a), f(b) \in H$ so $f(a) \times f(b) \in H$. When a homomorphism $f : G \to H$ is bijective, we say that f is an **isomorphism**, and the groups G and H are said to be isomorphic, written $G \simeq H$.

Theorem A.1. *Any finite abelian group G is isomorphic to a direct product of cyclic groups.*

Using $\mathbb{Z}_n$ to refer to the set of integers modulo n, we see that all cyclic groups of order n are isomorphic to $\mathbb{Z}_n$. Since C_4 is cyclic and of order 4, $C_4 \simeq \mathbb{Z}_4$. Meanwhile, D_2 is abelian but not cyclic. Because D_2 has two generators which are both of order 2, we find that $D_2 \simeq \mathbb{Z}_2 \otimes \mathbb{Z}_2$.

With particular eye toward representation theory, it is useful to study smaller aspects of a group, when possible. For some groups, we can find a subset which itself acts as a group. Predictably, these are known as subgroups.

Definition. A **subgroup** of a group G is a subset $H \subseteq G$ which is closed and invertible. We write $H \leq G$.

Continuing our example, D_2 and C_4 are themselves subgroups of D_{4h}. D_{4h} has sixteen elements, which we can recognize as eight proper rotations and eight improper rotations. The proper rotations are the four elements of C_4, as well as four additional rotations through 180° about the x-axis, y-axis, and the two main diagonals X and Y. These are identified as C_{2x}, C_{2y}, C_{2X} and C_{2Y}. The improper rotations are given by a proper rotation followed by inversion through the center; the inversion alone is I, and then there are five mirror planes perpendicular to the C_2 axes, $\sigma_z = IC_2$, $\sigma_x = IC_{2x}$, etc., and two four-fold improper rotations which we take to be $S_4^{\pm} = IC_4^{\pm}$[a]. We can generate D_{4h} from I, σ_y and σ_Y, which obey the generating relations

$$I^2 = \sigma_y^2 = \sigma_Y^2 = (I\sigma_y)^2 = (I\sigma_Y)^2 = (\sigma_y\sigma_Y)^4 .$$

Notice that $|C_4| = 4$ while $|D_{4h}| = 16$; this is an instance of a general fact about finite groups which is known as Lagrange's Theorem:

Theorem A.2. *For any finite group G, if $H \leq G$, then $|H|$ is a divisor of $|G|$.*

As a corollary, we can define the **index** of a subgroup $H \leq G$, denoted $[G : H]$, by $|G| = [G : H]|H|$. We can see, therefore, that G can be partitioned into $[G : H]$ subsets of size $|H|$ when $H \leq G$. One way to effect such a partition is to use cosets as equivalence classes:

Definition. Let $H \leq G$, and let $g \in G$. The **left coset** of g given H is $gH \equiv \{gh | h \in H\}$; similarly, the **right coset** is $Hg \equiv \{hg | h \in H\}$.

Because cosets partition the group G, we can say $a \sim_H b$ if, and only if, $b \in aH$; it follows that $a \in bH$ as well. We can define a type of coset multiplication in the natural way; if $H \leq G$ and $a, b \in G$, then $(aH)(bH) = abH \equiv \{abh | h \in H\}$, where abh is the product using the operation in G. For coset multiplication to truly be considered an operation, it must be true that if $a \sim_H c$ and $b \sim_H d$, then $ab \sim_H cd$; unfortunately, this is not generally the case. However, if $gH = Hg$ for every $g \in G$, then coset multiplication is an operation on the set of cosets.

Definition. Let $H \leq G$. We say H is a **normal** subgroup of G—written $H \triangleleft G$—if, and only if, $gH = Hg$ for all $g \in G$.

Given a normal subgroup $H \triangleleft G$, the partition of G into cosets of H is a group under coset multiplication; this group is called a **quotient group**, often denoted G/H. Because H is a subgroup of G, $e \in H$ is the identity of G, and for any $h \in H$ we have $h \sim_H e$. Therefore, H is the identity element of G/H.

If $H \triangleleft G$, then $gH = Hg$ for any $g \in G$, by definition. This is equivalent to stating that $g^{-1}Hg = H$ for any $g \in G$, where of course $g^{-1}Hg = \{g^{-1}hg | h \in H\}$. The element $g^{-1}hg$ is known as the **conjugate** of h under g. Any group G can be partitioned into **conjugacy classes**, denoted $\mathrm{Cl}(h) \equiv \{g^{-1}hg | g \in G\}$, such that $a \sim b$ under conjugation if there is some $g \in G$ such that $a = g^{-1}bg$. We shall see later that the conjugacy classes are useful in determining the character table of a group.

Continuing our example, we explore the conjugacy classes of D_{4h}. First, we identify that any element $c \in G$ which commutes with every element of G is the only element of its class, so we can identify four single element classes, $\{E\}$, $\{I\}$, $\{C_2\}$, and $\{\sigma_z\}$. The remaining conjugacy classes are

[a] Some authors will instead take $S_4^{\pm} = IC_4^{\mp}$.

all two element classes, $\{\sigma_x, \sigma_y\}$, $\{\sigma_X, \sigma_Y\}$, $\{C_{2x}, C_{2y}\}$, $\{C_{2X}, C_{2Y}\}$, $\{C_4^+, C_4^-\}$, and $\{S_4^+, S_4^-\}$. In total, there are ten conjugacy classes. Because D_{4h} has some conjugacy classes with more than one element, there must be some elements which do not commute with every element of D_{4h}; the extent to which a group fails to be commutative is captured by the commutator.

Given two elements $g, h \in G$, the **commutator** of g and h is defined as $[g, h] \equiv g^{-1}h^{-1}gh$. Using this, we can define the commutator subgroup, $[G, G] \triangleleft G$, which is a normal subgroup of G generated by the commutators $[g, h]$ for every $g, h \in G$. As the commutator subgroup is a normal subgroup, we can form the quotient group $G/[G, G]$; the quotient group so formed is abelian, and is the largest abelian quotient of G, called the **abelianization** of G. For D_{4h}, the commutator subgroup is $[D_{4h}, D_{4h}] = \{E, C_2\}$, and the abelianization is

$$\{\{E, C_2\}, \{I, \sigma_z\}, \{\sigma_x, \sigma_y\}, \{\sigma_X, \sigma_Y\}, \{C_{2x}, C_{2y}\}, \{C_{2X}, C_{2Y}\}, \{C_4^+, C_4^-\}, \{S_4^+, S_4^-\}\}.$$

It is not surprising that the cosets in the abelianization are related to the conjugacy classes, after all $h^{-1}gh = g[g, h]$.

Related to the commutator is the **centralizer** $C_G(h) = \{g | [g, h] = e\}$, the subgroup of G of all the elements which commute with a given element h. In the example of D_{4h}, we observe that $C_{D_{4h}}(E) = D_{4h}$, whereas $C_{D_{4h}}(\sigma_X) = \{E, C_2, I, \sigma_z, \sigma_X, \sigma_Y, C_{2X}, C_{2Y}\}$.

A.2 REPRESENTATIONS OF FINITE GROUPS

We now move on to the representation theory of finite groups. The central idea is to take an abstract group with an abstract operation, and to attempt to find a set of (usually) matrices which, under matrix multiplication, respects the abstract group's structure. Not surprisingly, the tools for the job are homomorphisms. In this section we present some of the main results from representation theory which will allow us to develop and understand the character table for D_{4h}.

Definition. Given a group G and a vector space V over a scalar field F, $\langle \pi, V \rangle$ forms a **representation** if, and only if, $\pi : G \to \mathrm{GL}(V)$ is a homomorphism.

For us, the scalar field is the complex numbers $\mathbb{C}$ and the vector space is $\mathbb{C}^n$, so $\mathrm{GL}(\mathbb{C}^n)$ is the group of $n \times n$ invertible matrices; the dimension of the vector space V, n in our case, is the dimension (or degree) of the representation. Representation theory typically studies "fundamental" representations of groups; this notion is captured as irreducible representations. Let G be a group and π be a representation of G on a vector space V of dimension n. We want to consider how subspaces $W \subseteq V$ are transformed under the action of G via the representation π. Since $\pi : G \to \mathrm{GL}(V)$, then given any $g \in G$, $\pi_g : V \to V$. Then, if we take any $|w\rangle \in W \subseteq V$ and if $\pi_g |w\rangle \in W$ for every $g \in G$, then W is an **invariant subspace** of V, and $\langle \pi, W \rangle$, the representation restricted to W, is a **subrepresentation**.

Any vector space V has two subspaces which are trivially invariant for any representation—these are V itself, and $\{0\}$. A representation π is therefore **irreducible** if V contains no non-trivial invariant subspaces under π; otherwise, the representation is **reducible**. As a consequence, if V is a one-dimensional vector space it cannot contain any proper subspaces, so any one-dimensional representations are irreducible. For finite groups, representations are completely reducible; that is, the space V can be written $V = \bigoplus_i W_i$, where each W_i is an invariant subspace.

Definition. Let $\langle \pi, V \rangle$ and $\langle \pi', V' \rangle$ be representations on G. We define $L : V \to V'$ to be an **intertwining operator** (sometimes called a G-map or G-linear map, instead) if, and only if, L is linear and $L[\pi_g |v\rangle] = \pi'_g L[|v\rangle]$.

Much like homomorphisms allow us to define an idea of equivalence between groups—the bijective homomorphism, or isomorphism—intertwining operators allow us to define an idea of equivalence between representations on groups. Two representations are considered equivalent if they are related by a bijective intertwining operator. Of particular interest are the intertwining operators that relate irreducible representations, which are the purview of Schur's lemma:

Theorem A.3. *If $\langle \pi, V \rangle$ and $\langle \pi', V' \rangle$ are irreducible representations of G, and $L : V \to V'$ is an intertwining operator, then either $L = 0$ or L is bijective.*

Schur's lemma allows us to show the Great Orthogonality Theorem: given two irreducible representations $\pi^{(r)}$ and $\pi^{(s)}$ of a group G, we observe that

$$\sum_g [\pi_{ij}^{(r)}]^\dagger \pi_{kl}^{(s)} = \frac{|G|}{d} \delta_{il} \delta_{jk} \delta_{rs} \,,$$

where d is the dimension of the representation $\pi^{(r)}$. This result can be used to prove additionally that the number of irreducible representations of a group G is equal to the number of conjugacy classes in G, and further more, if d_r is the dimension of each irreducible representation, that

$$\sum_r d_r^2 = |G| \,.$$

We can also find that the number of one-dimensional irreducible representations is equal to $|G/[G,G]|$, the order of the abelianization of G. These three facts in particular will be used to determine the character table for D_{4h}. A **character** is a basis independent description of a representation.

Definition. Let $\langle \pi, V \rangle$ be a representation on G. The **character**, χ, of the representation is given by $\chi = \{\chi(g) | g \in G\}$ where $\chi(g) = \mathrm{Tr}(\pi(g))$.

We can then write the orthogonality relations for characters by taking the trace of the Great Orthogonality Theorem. Given a group G and for the irreducible representations $\pi^{(r)}$ and $\pi^{(s)}$,

$$\sum_g [\chi^{(r)}]^*(g) \chi^{(s)}(g) = |G| \delta_{rs} \,,$$

where $\chi^{(a)}$ is the character of the irreducible representation $\pi^{(a)}$. If we have a representation ρ which is reducible, the character orthogonality relation instead returns $n_r |G|$, where n_r is the number of times the irreducible representation $\pi^{(r)}$ is present in the decomposition of ρ into a sum of irreducible representations. This also implies that for an abelian group, the number of irreducible representations equals the order of the group, as each element is its own conjugacy class.

Going back to our example with D_{4h}, which has $|D_{4h}| = 16$, and ten conjugacy classes; therefore, there are ten inequivalent irreducible representations. The commutator subgroup is $[D_{4h}, D_{4h}] = \{E, C_2\}$, so the order of the abelianization is eight, and there are therefore eight one-dimensional irreducible representations. Since the sum of the squares of the dimensions of the representations is equal to the order of the group, we have $8(1^2) + n^2 + m^2 = 16$, or $n^2 + m^2 = 8$; the only integer solutions to this has $n = m = 2$. Thus, D_{4h} has ten irreducible representations; eight one-dimensional representations and two two-dimensional representations.

To determine the characters for the one dimensional representations, we start by considering cyclic groups. Suppose G is a cyclic group of order n, generated by a. Since cyclic groups are abelian, there are n conjugacy classes, and therefore n irreducible representations, which must all be one dimensional. These can be determined by assigning to $\chi_n(a)$ one of the n n^{th} roots of unity, and

$\mathbb{Z}_2 \otimes \mathbb{Z}_2 \otimes \mathbb{Z}_2$	$(0,0,0)$	$(1,0,0)$	$(0,1,0)$	$(1,1,0)$	$(0,0,1)$	$(1,0,1)$	$(0,1,1)$	$(1,1,1)$
D^{+++}	1	1	1	1	1	1	1	1
D^{++-}	1	1	1	1	-1	-1	-1	-1
D^{+-+}	1	1	-1	-1	1	1	-1	-1
D^{+--}	1	1	-1	-1	-1	-1	1	1
D^{-++}	1	-1	1	-1	1	-1	1	-1
D^{-+-}	1	-1	1	-1	-1	1	-1	1
D^{--+}	1	-1	-1	1	1	-1	-1	1
D^{---}	1	-1	-1	1	-1	1	1	-1

Table A.2: Eight one-dimensional representations of $\mathbb{Z}_2 \otimes \mathbb{Z}_2 \otimes \mathbb{Z}_2 \simeq D_{4h}/[D_{4h}, D_{4h}]$

applying the homomorphism property. For a general abelian group, then, since $G \simeq \mathbb{Z}_{n_1} \otimes \mathbb{Z}_{n_2} \otimes \ldots$, the representations are given by products of the $n_1, n_2, \ldots$ roots of unity.

The one-dimensional representations of D_{4h} are taken from the abelianization of D_{4h}. We have $D_{4h}/[D_{4h}, D_{4h}] \simeq \mathbb{Z}_2 \otimes \mathbb{Z}_2 \otimes \mathbb{Z}_2$ where the isomorphism is defined by $I[D_{4h}, D_{4h}] \mapsto (1,0,0)$, $\sigma_x[D_{4h}, D_{4h}] \mapsto (0,1,0)$, and $\sigma_X[D_{4h}, D_{4h}] \mapsto (0,0,1)$. The representations are given by the two square roots of unity, ± 1, and we find eight representations which we write $D^{\alpha\beta\gamma}(i,j,k) = \alpha^i \beta^j \gamma^k$, where α, β, $\gamma \in \{\pm 1\}$ and i, j, $k \in \mathbb{Z}_2$; these are displayed in table A.2. We can then extend this to a representation on D_{4h} by mapping members of the same coset in the abelianization to the same value, *e.g.*, $D^{-++}(\sigma_z) = D^{-++}(I) = -1$.

In order to determine the characters for the two-dimensional representations of D_{4h}, we will introduce the method of induced representations. An irreducible representation π of degree $n > 1$ on a group G may become reducible when restricted to a subgroup $H < G$—in fact, if H is abelian, π must necessarily become reducible. The method of induced representations attempts to reverse this process by finding irreducible representations on the subgroup H, and determining representations of G which reduce to the irreducible representations on H; some of the representations constructed in this manner will be irreducible representations of G. We should note that this method, as outlined, is not guaranteed to generate all the irreducible representations of degree $n > 1$, but does in the cases we consider.

Let G be a group and let $H < G$ with index $[G : H] = n$. We can partition G into cosets $g_i H$, where $g_1, \ldots, g_n$ are fixed coset representatives; typically we choose $g_1 = e$ for convenience. For this construction, it is not necessary for $H \triangleleft G$; any subgroup H allows us to partition G into cosets. Suppose $\langle \pi, V \rangle$ is some known representation on H of degree m. For each g_i among the coset representatives, we can associate a vector space V_i isomorphic to V and construct the space $W = \bigoplus_i V_i$; the induced representation is $\langle \pi_\uparrow, W \rangle$. The character of the induced representation, ψ, is given in terms of the character, χ, of the known representation by the **Frobenius formula**:

$$\psi(h) = \sum_{g_i} \hat{\chi}(g_i^{-1} h g_i) \tag{A.1}$$

where $\hat{\chi}(h) = \chi(h)$ for $h \in H$, and $\hat{\chi}(h) = 0$ otherwise.

In the example of D_{4h}, we will take the centralizer $C(\sigma_X)$ to be the subgroup of D_{4h} which we induce representations from. The centralizer is abelian by construction; we see that $C(\sigma_X) \simeq \mathbb{Z}_2 \otimes \mathbb{Z}_2 \otimes \mathbb{Z}_2$, by the isomorphism $I \mapsto (1,0,0)$, $\sigma_X \mapsto (0,1,0)$, and $\sigma_Y \mapsto (0,0,1)$. Since $[D_{4h} : C(\sigma_X)] = 2$, we can write $D_{4h} = C(\sigma_X) \oplus \sigma_x C(\sigma_X)$. Then, using eq. (A.1), we get the induced representations shown in table A.3

Table A.3 has eight induced representations generated from the eight irreducible representations

$C_G(\sigma_X) \uparrow D_{4h}$	E	C_2	I	σ_h	$2\sigma_d$	$2C_2''$	$2\sigma_v$	$2C_2'$	$2C_4$	$2S_4$
$D^{+++} \uparrow D_{4h}$	2	2	2	2	2	2	0	0	0	0
$D^{++-} \uparrow D_{4h}$	2	−2	2	−2	0	0	0	0	0	0
$D^{+-+} \uparrow D_{4h}$	2	−2	2	−2	0	0	0	0	0	0
$D^{+--} \uparrow D_{4h}$	2	2	2	2	−2	−2	0	0	0	0
$D^{-++} \uparrow D_{4h}$	2	2	−2	−2	2	−2	0	0	0	0
$D^{-+-} \uparrow D_{4h}$	2	−2	−2	2	0	0	0	0	0	0
$D^{--+} \uparrow D_{4h}$	2	−2	−2	2	0	0	0	0	0	0
$D^{---} \uparrow D_{4h}$	2	2	−2	−2	−2	2	0	0	0	0

Table A.3: The induced representations from the centralizer $C_G(\sigma_X)$ induced on the group $G = D_{4h}$.

D_{4h}	E	C_2	I	σ_h	$2\sigma_v$	$2C_2'$	$2\sigma_d$	$2C_2''$	$2C_4$	$2S_4$
A_{1g}	1	1	1	1	1	1	1	1	1	1
A_{2g}	1	1	1	1	−1	−1	−1	−1	1	1
B_{1g}	1	1	1	1	1	1	−1	−1	−1	−1
B_{2g}	1	1	1	1	−1	−1	1	1	−1	−1
A_{1u}	1	1	−1	−1	−1	1	−1	1	1	−1
A_{2u}	1	1	−1	−1	1	−1	1	−1	1	−1
B_{1u}	1	1	−1	−1	−1	1	1	−1	−1	1
B_{2u}	1	1	−1	−1	1	−1	−1	1	−1	1
E_g	2	−2	2	−2	0	0	0	0	0	0
E_u	2	−2	−2	2	0	0	0	0	0	0

Table A.4: D_{4h} character table.

of $C_{D_{4h}}(\sigma_X)$, however, there can only be two two-dimensional irreducible representations on D_{4h}, so some of the induced representations must be reducible. To determine which representations are irreducible and which are reducible, we can use the character orthogonality relations to determine which representations are reducible, and which are irreducible.

Applying this to the induced representations in table A.3, we see that $D^{\alpha\beta\beta} \uparrow D_{4h}$are all reducible representations, while $D^{+\pm\mp} \uparrow D_{4h}$ is the E_g representation, and $D^{-\pm\mp} \uparrow D_{4h}$ is the E_u representation, which are both irreducible representations.

A.3 REPRESENTATIONS OF A FUNCTION SPACE

Given any vector space V, we'll define $\mathcal{F}(V)$ to be the set of all functions $f : V \to \mathbb{C}$; $\mathcal{F}(V)$ is itself a vector space. Then, given some representation $\langle \sigma, V \rangle$ of G, we can define a representation $\langle \pi_\sigma, \mathcal{F}(V) \rangle$ on G by

$$\pi_\sigma(g)[f(v)] = f(\sigma_{\overline{g}}[v])\,. \tag{A.2}$$

The representation $\langle \pi_\sigma, \mathcal{F}(V) \rangle$ is infinite-dimensional, but we are able to find subrepresentations equivalent to the irreducible representations of G. This is analogous to Fourier analysis, allowing us to determine basis functions which any functions $f \in \mathcal{F}(V)$ can be decomposed into.

Considering D_{4h}, we'll define the **standard representation** $\langle \Sigma, \mathbb{R}^3 \rangle$:

$$\Sigma(E) = \begin{pmatrix} 1 & 0 & 0 \\ 0 & 1 & 0 \\ 0 & 0 & 1 \end{pmatrix} \qquad \Sigma(I) = \begin{pmatrix} -1 & 0 & 0 \\ 0 & -1 & 0 \\ 0 & 0 & -1 \end{pmatrix}$$

$$\Sigma(C_4^+) = \begin{pmatrix} 0 & -1 & 0 \\ 1 & 0 & 0 \\ 0 & 0 & 1 \end{pmatrix} \qquad \Sigma(S_4^+) = \begin{pmatrix} 0 & 1 & 0 \\ -1 & 0 & 0 \\ 0 & 0 & -1 \end{pmatrix}$$

$$\Sigma(C_2) = \begin{pmatrix} -1 & 0 & 0 \\ 0 & -1 & 0 \\ 0 & 0 & 1 \end{pmatrix} \qquad \Sigma(\sigma_z) = \begin{pmatrix} 1 & 0 & 0 \\ 0 & 1 & 0 \\ 0 & 0 & -1 \end{pmatrix}$$

$$\Sigma(C_4^-) = \begin{pmatrix} 0 & 1 & 0 \\ -1 & 0 & 0 \\ 0 & 0 & 1 \end{pmatrix} \qquad \Sigma_(S_4^-) = \begin{pmatrix} 0 & -1 & 0 \\ 1 & 0 & 0 \\ 0 & 0 & -1 \end{pmatrix}$$

$$\Sigma(C_{2x}) = \begin{pmatrix} 1 & 0 & 0 \\ 0 & -1 & 0 \\ 0 & 0 & -1 \end{pmatrix} \qquad \Sigma(\sigma_x) = \begin{pmatrix} -1 & 0 & 0 \\ 0 & 1 & 0 \\ 0 & 0 & 1 \end{pmatrix}$$

$$\Sigma(C_{2y}) = \begin{pmatrix} -1 & 0 & 0 \\ 0 & 1 & 0 \\ 0 & 0 & -1 \end{pmatrix} \qquad \Sigma(\sigma_y) = \begin{pmatrix} 1 & 0 & 0 \\ 0 & -1 & 0 \\ 0 & 0 & 1 \end{pmatrix}$$

$$\Sigma(C_{2X}) = \begin{pmatrix} 0 & 1 & 0 \\ 1 & 0 & 0 \\ 0 & 0 & -1 \end{pmatrix} \qquad \Sigma(\sigma_X) = \begin{pmatrix} 0 & -1 & 0 \\ -1 & 0 & 0 \\ 0 & 0 & 1 \end{pmatrix}$$

$$\Sigma(C_{2Y}) = \begin{pmatrix} 0 & -1 & 0 \\ -1 & 0 & 0 \\ 0 & 0 & -1 \end{pmatrix} \qquad \Sigma(\sigma_Y) = \begin{pmatrix} 0 & 1 & 0 \\ 1 & 0 & 0 \\ 0 & 0 & 1 \end{pmatrix}$$

Using this representation, we can define $\langle \pi_\Sigma, \mathcal{F}(\mathbb{R}^3) \rangle$ and determine basis functions. Of particular interest are polynomials up to quadratic order in x and y, which are used in the low-energy expansion of the Hamiltonian. A trivial invariant subspace is given by $\text{span}(f(x, y, z) = c)$, which clearly transforms as the A_{1g} representation. A less trivial subspace is given by $f(k_x, k_y, k_z) = k_x^2 - k_y^2$. We observe that

$$\begin{aligned} \pi_\Sigma(I)[f(k_x, k_y, k_z)] &= f(-k_x, -k_y, -k_z) = k_x^2 - k_y^2 \\ \pi_\Sigma(\sigma_y)[f(k_x, k_y, k_z)] &= f(k_x, -k_y, k_z) = k_x^2 - k_y^2 \\ \pi_\Sigma(\sigma_Y)[f(k_x, k_y, k_z)] &= f(k_y, k_x, k_z) = -(k_x^2 - k_y^2)\,, \end{aligned}$$

which indicates that $k_x^2 - k_y^2$ transforms as the B_{1g} representation.

Appendix B

REPRESENTATION THEORY OF SPACE GROUPS

Unlike the finite groups of appendix A, space groups are infinite groups, so the tools developed in appendix A must be augmented to deal with this. Fortunately, a space group, $\mathcal{G}$, is a subgroup of $P \ltimes \mathbb{R}^3$, where P is a (finite) point group—which we can view as consisting of rotations and reflections that preserve a lattice L—and where $\mathbb{R}^3$ is an abelian group of translations leaving no fixed points. It is these translations which are responsible for the infinite size of $\mathcal{G}$. We will use for our example the space group $P4/nmm$, for which the point group P is D_{4h}. Elements of $\mathcal{G}$ are ordered pairs of the form $\{g|\boldsymbol{u}\}$. Using the standard representation from appendix A.3, we define $g\boldsymbol{v} \in \mathbb{R}^3$ for any $\boldsymbol{v} \in \mathbb{R}^3$ and $g \in P$. This then allows us to define the operation for the group $\mathcal{G}$ as $\{g|\boldsymbol{u}\}\{h|\boldsymbol{v}\} = \{gh|\boldsymbol{u} + g\boldsymbol{v}\}$[a]; it follows that $\{g|\boldsymbol{u}\}^{-1} = \{\overline{g}| - \overline{g}\boldsymbol{u}\}$.

For a crystal system, we identify a normal subgroup $T \triangleleft \mathcal{G}$ which consists of only elements of the form $\{1|\boldsymbol{t}\}$, where $E \in P$ is the identity element and $\boldsymbol{t} \in \mathbb{R}^3$ is a lattice translation—that is, a translation which maps the lattice L to itself. Since the elements of P are also lattice preserving, it is not difficult to show that T is in fact normal as $\{g|\boldsymbol{u}\}^{-1}\{1|\boldsymbol{t}\}\{g|\boldsymbol{u}\} = \{1|\overline{g}\boldsymbol{t}\}$. Because $T \triangleleft \mathcal{G}$, we can form the quotient $\mathcal{G}/T \simeq P$; the elements of $\mathcal{G}/T$ are cosets of the form $\{g|\boldsymbol{u}\}T$. These cosets also partition $\mathcal{G}$, so we can write

$$\mathcal{G} = \bigotimes_i \{g_i|\boldsymbol{w}_i\}T\,.$$

Generally, we observe that $\{g_i|\boldsymbol{w}_i\}\{g_j|\boldsymbol{w}_j\} = \{1|\boldsymbol{t}_{ijk}\}\{g_k|\boldsymbol{w}_k\}$, where $g_k = g_i g_j$ and $\boldsymbol{t}_{ij} = \boldsymbol{w}_i + g_i\boldsymbol{w}_j - \boldsymbol{w}_k$ is a lattice vector. We can therefore distinguish two categories of space group; the first are known as **symmorphic** space groups, which have the feature that we can choose the $\boldsymbol{w}_i$ such that $\boldsymbol{t}_{ijk} = 0$ for all i, j, k; this is equivalent to $\{\{g_i|\boldsymbol{w}_i\}\} \simeq P$ or, for an appropriate choice of origin, we have $\boldsymbol{w}_i = 0$ for all i. The second category of space groups, which the majority fall under, are the **non-symmorphic** space groups which fail to have this property. For non-symmorphic space groups, the set of coset representatives does not form a subgroup of $\mathcal{G}$. As this is a subtle difference, the point is worth repeating. The quotient group consists of the cosets $\{g_i|\boldsymbol{w}_i\}T$; for a symmorphic group, the coset representatives $\{\{g_i|\boldsymbol{w}_i\}\}$ themselves are a subgroup of G. For a non-symmorphic group, the quotient group remains a quotient group, but the set of coset representatives alone are not a subgroup of G.

While in appendix A, we worked to develop the basis independent characters for the irreducible representations of a group, a similar approach for developing the irreducible representations for space groups is beyond the scope of this work. Instead, we work in the context of the natural basis of Bloch functions. To begin, we note that for the abelian group of translations $\mathbb{R}^3$ alone, we can determine a set of one-dimensional representations characterized by some (reciprocal) vector

[a] Note that the vector $g\boldsymbol{v}$ is defined by the representation of $g \in P$, which must be specified. We are using $g\boldsymbol{v}$ as a shorthand for $\Sigma_g[\boldsymbol{v}]$.

$\boldsymbol{k}$; $\Delta_{\boldsymbol{k}}(\boldsymbol{r}) = e^{-i\boldsymbol{k}\cdot\boldsymbol{r}}$. When $\Delta_{\boldsymbol{k}}$ is restricted to T, it remains a representation but we observe that $\Delta_{\boldsymbol{k}+\boldsymbol{G}}(\boldsymbol{t}) = \Delta_{\boldsymbol{k}}(\boldsymbol{t})$ for vectors $\boldsymbol{G}$ which are the reciprocal lattice vectors characterized by $\boldsymbol{G}\cdot\boldsymbol{t} = 2n\pi$.

Bloch functions are basis functions for the representations $\Delta_{\boldsymbol{k}}$. Bloch functions are also parametrized by reciprocal vectors and have the form $\psi_{\boldsymbol{k}}(\boldsymbol{r}) = u_{\boldsymbol{k}}(\boldsymbol{r})e^{i\boldsymbol{k}\cdot\boldsymbol{r}}$, where $u_{\boldsymbol{k}}(\boldsymbol{r})$ has the periodicity of the lattice—that is $u_{\boldsymbol{k}}(\boldsymbol{r}+\boldsymbol{t}) = u_{\boldsymbol{k}}(\boldsymbol{r})$ for lattice vectors $\boldsymbol{t}$. Using the representation of function spaces, discussed in appendix A.3, we observe that $\psi_{\boldsymbol{k}}(\boldsymbol{r}-\boldsymbol{t}) = \Delta_{\boldsymbol{k}}(\boldsymbol{t})\psi_{\boldsymbol{k}}(\boldsymbol{r})$. Because Bloch functions serve as basis functions for lattice translations, we use them to motivate a basis-dependent description of the representations for the space group $\mathcal{G}$.

Consider the action of $\{g|\boldsymbol{u}\} \in \mathcal{G}$ on $\psi_{\boldsymbol{k}}(\boldsymbol{r})$; $\{g|\boldsymbol{u}\}\psi_{\boldsymbol{k}}(\boldsymbol{r}) = u_{\boldsymbol{k}}[\overline{g}(\boldsymbol{r}-\boldsymbol{u})]e^{i\boldsymbol{k}\cdot\overline{g}(\boldsymbol{r}-\boldsymbol{u})}$. Noting that $\boldsymbol{k}\cdot\overline{g}\boldsymbol{x} = g\boldsymbol{k}\cdot\boldsymbol{x}$, we define $u_{g\boldsymbol{k}}(\boldsymbol{x}) = u_{\boldsymbol{k}}(\overline{g}\boldsymbol{x})$, and observe that $\{g|\boldsymbol{u}\}\psi_{\boldsymbol{k}}(\boldsymbol{r}) = \psi_{g\boldsymbol{k}}(\boldsymbol{r}-\boldsymbol{u})$. In the event that $g\boldsymbol{k} = \boldsymbol{k}+\boldsymbol{G}$ for some reciprocal lattice vector $\boldsymbol{G}$, then $\psi_{g\boldsymbol{k}}(\boldsymbol{r}) = \psi_{\boldsymbol{k}}(\boldsymbol{r})$. It is convenient, therefore, to define the **little co-group** of $\boldsymbol{k}$, $P_{\boldsymbol{k}}$, to be the set of all $g \in P$ where $g\boldsymbol{k} = \boldsymbol{k}+\boldsymbol{G}$. Related to the little co-group is the **little group**; this is the set of all $\{g|\boldsymbol{u}\} \in \mathcal{G}$ such that $g \in P_{\boldsymbol{k}}$. The little group at $\boldsymbol{k}$ is denoted by $\mathcal{G}_{\boldsymbol{k}}$. We can also define the star of $\boldsymbol{k}$ to be the set of all reciprocal vectors $\boldsymbol{k}'$—up to equivalence by a reciprocal lattice vector—which $\boldsymbol{k}$ is mapped to under the action of P; this set is typically denoted $P\boldsymbol{k}$. In order to fully specify the representations for all $\boldsymbol{k}$, it suffices to specify the representations for only one element of the star of $\boldsymbol{k}$ for each $\boldsymbol{k}$.

At each point $\boldsymbol{k}$, we consider some representation $\Gamma^n_{\boldsymbol{k}}$. If this representation is restricted to $\mathcal{G}_{\boldsymbol{k}}$, then we find that $\Gamma^n_{\boldsymbol{k}}(\{g|\boldsymbol{u}\}) = A_{\boldsymbol{k}}(\boldsymbol{u})D_n(g)$, where $A_{\boldsymbol{k}}(\boldsymbol{u}) = e^{-i\boldsymbol{k}\cdot\boldsymbol{u}}$ is a representation of T at $\boldsymbol{k}$ (translations are abelian) and D_n is a representation of the point-group $P_{\boldsymbol{k}}$. Consider the product of two coset representatives (restricted to $\mathcal{G}_{\boldsymbol{k}}$):

$$\Gamma^n_{\boldsymbol{k}}(\{g_i|\boldsymbol{w}_i\})\Gamma^n_{\boldsymbol{k}}(\{g_j|\boldsymbol{w}_j\}) = e^{-i\boldsymbol{k}\cdot\boldsymbol{t}_{ijk}}\Gamma^n_{\boldsymbol{k}}(\{g_k|\boldsymbol{w}_k\})$$

or

$$D_n(g_i)D_n(g_j) = e^{-i\boldsymbol{G}_i\cdot\boldsymbol{w}_j}D_n(g_ig_j)\,,$$

where $\boldsymbol{G}_i = \overline{g_i}\boldsymbol{k} - \boldsymbol{k}$; since we have restricted ourselves to elements of $\mathcal{G}_{\boldsymbol{k}}$, $\boldsymbol{G}_i$ is a reciprocal lattice vector.

For a symmorphic space group, $\boldsymbol{w}_j = 0$ for all j, so we find that $D_n(g_i)D_n(g_j) = D_n(g_ig_j)$, which means D_n is an ordinary representation of the finite group $P_{\boldsymbol{k}}$. Additionally, for $\boldsymbol{k}$ in the interior of the Brillouin zone, we have $\boldsymbol{G}_i = 0$ for all i because for $g_i \in P_{\boldsymbol{k}}$ for interior points $\boldsymbol{k}$ we have $g_i\boldsymbol{k} = \boldsymbol{k}+0$, so again D_n is an ordinary representation. However, in a non-symmorphic group, which can have $\boldsymbol{w}_j \neq 0$, at the Brillouin zone boundary, which can have $\boldsymbol{G}_i \neq 0$, D_n no longer satisfies the homomorphism property, and as such is not a representation of $P_{\boldsymbol{k}}$. Instead, D_n is an example of a **projective representation**. Rather than satisfying the homomorphism property of a representation, projective representations satisfy $\phi(g)\phi(h) = c(g,h)\phi(gh)$; the family $c(g,h)$ of the projective representation is known as a **factor system** of the projective representation. A given projective representation can have many factor systems—the irreducible representations of the last chapter arise from a factor system where $c(g,h) = 1$ for all $g,h \in P$.

The most general approach for identifying projective representations involves identifying each possible factor system. However, because we have already determined the one factor system of interest, given by $c(g_i,g_j) = e^{-i\boldsymbol{G}_i\cdot\boldsymbol{w}_j}$, we could instead determine the representations D_n using the method described by Bradley and Cracknell [99]. For this method, a group $P_{\boldsymbol{k}} \otimes \mathbb{Z}_m$ is constructed with a product rule that considers the factor system. The constructed group has ordinary representations which become projective when reduced to $P_{\boldsymbol{k}}$, although not every representation respects the original factor system upon subduction. Those representations which respect the factor system are considered physical and the remaining representations are discarded. Once the physical representations D_n are

P_Γ	$\{1\|\boldsymbol{t}\}$	$\{2_{001}\|\frac{1}{2}\,\frac{1}{2}\}$	$\{\bar{1}\|0\,0\}$	$\{m_{001}\|\frac{1}{2}\,\frac{1}{2}\}$	$\{m_{010}\|0\,\frac{1}{2}\}$ $\{m_{100}\|\frac{1}{2}\,0\}$	$\{m_{1\bar{1}0}\|0\,0\}$ $\{m_{110}\|\frac{1}{2}\,\frac{1}{2}\}$	$\{2_{010}\|0\,\frac{1}{2}\}$ $\{2_{100}\|\frac{1}{2}\,0\}$	$\{2_{1\bar{1}0}\|0\,0\}$ $\{2_{110}\|\frac{1}{2}\,\frac{1}{2}\}$	$\{4^+_{001}\|\frac{1}{2}\,0\}$ $\{4^-_{001}\|0\,\frac{1}{2}\}$	$\{\bar{4}^+_{001}\|\frac{1}{2}\,0\}$ $\{\bar{4}^-_{001}\|0\,\frac{1}{2}\}$
Γ_1^+	1	1	1	1	1	1	1	1	1	1
Γ_1^-	1	1	−1	−1	−1	−1	1	1	1	−1
Γ_2^+	1	1	1	1	1	−1	1	−1	−1	−1
Γ_2^-	1	1	−1	−1	−1	1	1	−1	−1	1
Γ_3^+	1	1	1	1	−1	−1	−1	−1	1	1
Γ_3^-	1	1	−1	−1	1	1	−1	−1	1	−1
Γ_4^+	1	1	1	1	−1	1	−1	1	−1	−1
Γ_4^-	1	1	−1	−1	1	−1	−1	1	−1	1
Γ_5^+	2	−2	2	−2	0	0	0	0	0	0
Γ_5^-	2	−2	−2	2	0	0	0	0	0	0

Table B.1: Character table for $\mathcal{G}_\Gamma$.

determined, $\Gamma^n_{\boldsymbol{k}}$ is obtained via the definition $\Gamma^n_{\boldsymbol{k}}(\{g|\boldsymbol{u}\}) = e^{-i\boldsymbol{k}\cdot\boldsymbol{u}}D_n(g)$.

We will not use either of the above mentioned approaches. Instead, we use the approach of Herring [100]. This approach recognizes that D_n is a projective representation but that $\Gamma^n_{\boldsymbol{k}}$ is not, because $\Gamma^n_{\boldsymbol{k}}$ is defined on $\mathcal{G}_{\boldsymbol{k}}$, rather than on $\mathcal{G}_{\boldsymbol{k}}/T$, which D_n is defined over. For $\boldsymbol{k}$ on the Brillouin zone boundary, there is some subset of $\boldsymbol{t} \in T$ such that $\Gamma^n_{\boldsymbol{k}}(\{1|\boldsymbol{t}\}) = 1$, which we shall call T_e. It is clearly the case that $T_e \triangleleft \mathcal{G}_{\boldsymbol{k}}$, so we consider the quotient group $\mathcal{G}_{\boldsymbol{k}}/T_e$—which is also a finite group—rather than $\mathcal{G}_{\boldsymbol{k}}/T$. On this quotient group, $\{g|\boldsymbol{w}\} \sim \{g|\boldsymbol{w}+\boldsymbol{t}\}$ if and only if $e^{-i\boldsymbol{k}\cdot\boldsymbol{t}} = 1$, that is, if and only if $\boldsymbol{t} \in T_e$. Therefore, $\Gamma^n_{\boldsymbol{k}}(\{g|\boldsymbol{w}+\boldsymbol{t}\}) = \Gamma^n_{\boldsymbol{k}}(\{g|\boldsymbol{w}\})$ for all members of the coset $\{g|\boldsymbol{w}\}T_e$. Having determined $\mathcal{G}_{\boldsymbol{k}}/T_e$, we can construct the irreducible representations as was done in appendix A. As with the other methods, not all of the representations for $\mathcal{G}_{\boldsymbol{k}}/T_e$ will respect the factor system for D_n; those which do not can be discarded as unphysical at $\boldsymbol{k}$. The representations found in this way are the representations $\Gamma^n_{\boldsymbol{k}}$ when induced on $\mathcal{G}_{\boldsymbol{k}}$ and do not need multiplication by an additional phase factor as in the method used by Bradley and Cracknell.

In the next few sections, we will derive the character tables for the representations of $\mathcal{G}_{\boldsymbol{k}}$ for the high-symmetry points Γ, M and X as well as for the high-symmetry lines Σ, Δ, and Y.

B.1 Γ-POINT

The little co-group P_Γ is isomorphic to D_{4h}, the parent point group for $P4/nmm$. As Γ is in the interior of the Brillouin zone, the ordinary representations of D_{4h} form the irreducible representations Γ^n_Γ. Note that the phase factor associated with translations is $e^{-i\Gamma\cdot\boldsymbol{w}} = 1$. For the point group D_{4h} in table A.4 we identified the representations using Mulliken symbols, here we label the representations according to their $\boldsymbol{k}$ point to differentiate space group representations from point group representations.

As table B.1 provides the representations for $\mathcal{G}_\Gamma$, the convention is to provide the representations for the lattice translations $\{1|\boldsymbol{t}\}$ in the first column and the representations for only the coset representatives from $\mathcal{G}_\Gamma/T$ in the remaining columns of the table.

B.2 M-POINT

The little co-group P_M is once again isomorphic to D_{4h}, but because $P4/nmm$ is non-symmorphic and M lies on the Brillouin zone boundary, we need to identify the elements $\{1|\boldsymbol{t}\}$ for which

$e^{iM\cdot\boldsymbol{t}} = 1$. These are all of the translations $(m\,n)$ such that $m+n$ is even; so T_e is the set of all translations of an even number of lattice vectors. For the remainder of the section, we shall take $G \equiv \mathcal{G}_M/T_e$.

We find that G can be generated by $\{\overline{1}|0\,0\}$, $\{m_{1\overline{1}0}|0\,0\}$ and $\{m_{010}|0\,\frac{1}{2}\}$, with the generating relations

$$\begin{aligned}\{\overline{1}|0\,0\}^2 = \{m_{010}|0\,\tfrac{1}{2}\}^2 = \{m_{1\overline{1}0}|0\,0\}^2 = (\{\overline{1}|0\,0\}\{m_{1\overline{1}0}|0\,0\})^2 \\ = (\{\overline{1}|0\,0\}\{m_{010}|0\,\tfrac{1}{2}\})^4 = (\{m_{1\overline{1}0}|0\,0\}\{m_{010}|0\,\tfrac{1}{2}\})^4\end{aligned}$$

The order of the group is $|G| = 32$. Notice that $|G| = 2|D_{4h}|$; this is because $\{1|0\,0\} \not\sim \{1|1\,0\}$ in the quotient $\mathcal{G}/T_e$. We identify fourteen conjugacy classes; four are single element classes:

$$\begin{aligned} e &= \{\{1|0\,0\}\} & t &= \{\{1|1\,0\}\} \\ C_2 &= \left\{\{2_{001}|\tfrac{1}{2}\,\tfrac{1}{2}\}\right\} & tC_2 &= \left\{\{2_{001}|\tfrac{\overline{1}}{2}\,\tfrac{1}{2}\}\right\}\end{aligned}$$

six are two-element classes:

$$\begin{aligned} i &= \{\{\overline{1}|0\,0\},\,\{\overline{1}|1\,0\}\} & \sigma_h &= \left\{\{m_{001}|\tfrac{1}{2}\,\tfrac{1}{2}\},\,\{m_{001}|\tfrac{\overline{1}}{2}\,\tfrac{1}{2}\}\right\} \\ \sigma_d &= \left\{\{m_{1\overline{1}0}|0\,0\},\,\{m_{110}|\tfrac{1}{2}\,\tfrac{1}{2}\}\right\} & C_2'' &= \left\{\{2_{1\overline{1}0}|0\,0\},\,\{2_{110}|\tfrac{1}{2}\,\tfrac{1}{2}\}\right\} \\ t\sigma_d &= \left\{\{m_{010}|0\,\tfrac{\overline{1}}{2}\},\,\{2_{110}|\tfrac{\overline{1}}{2}\,\tfrac{1}{2}\}\right\} & tC_2'' &= \left\{\{2_{1\overline{1}0}|1\,0\},\,\{m_{110}|\tfrac{\overline{1}}{2}\,\tfrac{1}{2}\}\right\}\end{aligned}$$

and four are four-element classes:

$$\begin{aligned} \sigma_v &= \left\{\{m_{010}|0\,\tfrac{1}{2}\},\,\{m_{100}|\tfrac{1}{2}\,0\},\,\{m_{010}|0\,\tfrac{\overline{1}}{2}\},\,\{m_{100}|\tfrac{\overline{1}}{2}\,0\}\right\} \\ C_2' &= \left\{\{2_{010}|0\,\tfrac{1}{2}\},\,\{2_{100}|\tfrac{1}{2}\,0\},\,\{2_{010}|0\,\tfrac{\overline{1}}{2}\},\,\{2_{100}|\tfrac{\overline{1}}{2}\,0\}\right\} \\ C_4 &= \left\{\{4^+_{001}|\tfrac{1}{2}\,0\},\,\{4^-_{001}|0\,\tfrac{1}{2}\},\,\{4^+_{001}|\tfrac{\overline{1}}{2}\,0\},\,\{4^-_{001}|0\,\tfrac{\overline{1}}{2}\}\right\} \\ S_4 &= \left\{\{\overline{4}^+_{001}|\tfrac{1}{2}\,0\},\,\{\overline{4}^-_{001}|0\,\tfrac{1}{2}\},\,\{\overline{4}^+_{001}|\tfrac{\overline{1}}{2}\,0\},\,\{\overline{4}^-_{001}|0\,\tfrac{\overline{1}}{2}\}\right\}\end{aligned}$$

From this, it follows that there are fourteen irreducible representations of G. We can identify the commutator to be

$$[G,G] = \left\{\{1|0\,0\},\,\{2_{001}|\tfrac{1}{2}\,\tfrac{1}{2}\},\,\{1|1\,0\},\,\{2_{001}|\tfrac{\overline{1}}{2}\,\tfrac{1}{2}\}\right\},$$

from which it follows that the abelianization is of order eight and there are eight one-dimensional irreducible representations. Because $[G,G]/G \simeq \mathbb{Z}_2 \otimes \mathbb{Z}_2 \otimes \mathbb{Z}_2$ as in the case of D_{4h}, the determination of the one-dimensional irreducible representations proceeds in the same fashion as in appendix A.

For the remaining six irreducible representations, we must have $\sum d_i^2 = 24$, which can only be satisfied by taking all the remaining $d_i = 2$, so there are six two-dimensional representations in addition to the eight one-dimensional representations.

We observe that $\{m_{1\overline{1}0}|0\,0\}$, $\{m_{110}|\frac{1}{2}\,\frac{1}{2}\}$, $\{\overline{1}|0\,0\}$ and $\{\overline{1}|1\,0\}$ are all self-inverse and all mutually commute. Therefore, the subgroup $H \leq G$ formed from these generators is $H \simeq \mathbb{Z}_2 \otimes \mathbb{Z}_2 \otimes \mathbb{Z}_2 \otimes \mathbb{Z}_2$. H is a maximal abelian subgroup of G, so $G = H \oplus \{m_{010}|0\,\frac{1}{2}\}H$. For any element $h \in H$, we can write $h = \{\overline{1}|0\,0\}^p\{\overline{1}|1\,0\}^q\{m_{1\overline{1}0}|0\,0\}^r\{m_{110}|\frac{1}{2}\,\frac{1}{2}\}^s$ for $p,q,r,s \in \{0,1\}$, and we can therefore define the character $\chi^{abcd}(h) = a^p b^q c^r d^s$, where $a,b,c,d \in \{1,-1\}$. Using the Frobenius formula

(eq. (A.1)), we observe

$$\psi^{abcd}(h) = \hat{\chi}^{abcd}(h) + \hat{\chi}^{abcd}\left(\{m_{010}|0\,\tfrac{1}{2}\}\,h\,\{m_{010}|0\,\tfrac{1}{2}\}\right),$$

where $\hat{\chi}^{abcd}(g) = \chi^{abcd}(g)$ for $g \in H$, and zero otherwise. Because $H \triangleleft G$, it follows by definition that $\overline{g}hg \in H$ for any $g \in G$, so $\psi^{abcd}(g) = 0$ for $g \notin H$. For the remaining $h \in H$, we observe that

$$\{m_{010}|0\,\tfrac{1}{2}\}h\{m_{010}|0\,\tfrac{1}{2}\} = \{\overline{1}|0\,0\}^q\{\overline{1}|1\,0\}^p\{m_{1\overline{1}0}|0\,0\}^s\{m_{110}|\tfrac{1}{2}\,\tfrac{1}{2}\}^r$$

since $\{\overline{1}|0\,0\}$ and $\{\overline{1}|1\,0\}$ are conjugates under $\{m_{010}|0\,\frac{1}{2}\}$, as are $\{m_{1\overline{1}0}|0\,0\}$ and $\{m_{110}|\frac{1}{2}\,\frac{1}{2}\}$. Therefore, we can write

$$\psi^{abcd}(h) = \chi^{abcd}(h)[1 + (ab)^{p+q}(cd)^{r+s}]\,.$$

With $\psi^{abcd}(g)$ now determined for every $g \in G$, we observe that

$$\frac{1}{|G|}\sum_g |\psi^{abcd}(g)|^2 = \frac{1}{|G|}\sum_{p,q,r,s\in\{0,1\}} [1 + (ab)^{p+q}(cd)^{r+s}]^2 = \begin{cases} 2 & \text{if } a = b \text{ and } c = d \\ 1 & \text{otherwise} \end{cases}$$

When $a = b$ and $c = d$, then $1 + (ab)^{p+q}(cd)^{r+s} = 2$ for any value of p, q, r, s. Because there are sixteen possible combinations, the sum gives $16 * (2)^2 = 2|G|$. In all other cases, $1 + (ab)^{p+q}(cd)^{r+s} = 2$ for precisely half of the $g \in H_M$, and is zero for the other half, so the sum gives $8 * (2)^2 = |G|$. The characters of the reducible representations with $a = b$ and $c = d$ are therefore seen to be $\hat{\chi}_M^{aacc}(h) = 2a^{p+q}c^{r+s}$, and we observe that

$$\psi^{++++} = A_{1g} \oplus B_{2g} \qquad \psi^{++--} = A_{2g} \oplus B_{1g}$$
$$\psi^{----} = A_{1u} \oplus B_{2u} \qquad \psi^{--++} = A_{2u} \oplus B_{1u}$$

The remaining twelve representations with $a \neq b$ or $c \neq d$ are all irreducible, but may be equivalent. Noting that $\psi^{abcd}(\{1|1\,0\}) = ab$, the representations with $a = b$ are non-physical. Dispensing of these non-physical representations first, we consider $a = b$ and take $d = -c$; then $1 + (ab)^{p+q}(cd)^{r+s} \neq 0$ only for $r + s$ even. Therefore the non-zero characters are $\psi^{aac(-c)}(h) = 2(-1)^s a^{p+q}$, which depend only on the sign of a. We find

$$\psi^{+++-} = \psi^{++-+} = E_g$$
$$\psi^{--+-} = \psi^{---+} = E_u$$

The remaining eight irreducible representations are all physical, meaning $\psi^{a(-a)cd}\left[\{1|1\,0\}\right] = -\mathbb{1}$, but only up to four of these representations can be unique. We consider the cases $cd = \pm 1$ separately again. We observe

$$\psi^{a(-a)cc}(h) = (-1)^q a^{p+q}c^{r+s}[1 + (-1)^{p+q}]$$
$$\psi^{a(-a)c(-c)}(h) = (-1)^{q+s}a^{p+q}c^{r+s}[1 + (-1)^{p+q+r+s}]$$

When $cd = 1$, the non-zero characters are given by $\psi_M^{a(-a)cc}(h) = 2(-1)^q c^{r+s}$, which depends only on the sign of c. When $cd = -1$, the non-zero characters occur when $p + q + r + s$ is even, which is divided into two cases: either $p + q$ and $r + s$ are both even, or $p + q$ and $r + s$ are both odd. When $p + q$ and $r + s$ are both even, the non-zero characters are $\psi^{a(-a)c(-c)}(h) = 2(-1)^{q+s}$, which will

$\mathcal{G}_M$	$\{1\|\boldsymbol{t}\}$	$\{\bar{1}\|0\,0\}$	$\{2_{001}\|\frac{1}{2}\,\frac{1}{2}\}$	$\{m_{001}\|\frac{1}{2}\,\frac{1}{2}\}$	$\{m_{1\bar{1}0}\|0\,0\}$ $\{m_{110}\|\frac{1}{2}\,\frac{1}{2}\}$	$\{m_{010}\|0\,\frac{1}{2}\}$ $\{m_{100}\|\frac{1}{2}\,0\}$	$\{2_{1\bar{1}0}\|0\,0\}$ $\{2_{110}\|\frac{1}{2}\,\frac{1}{2}\}$	$\{2_{010}\|0\,\frac{1}{2}\}$ $\{2_{100}\|\frac{1}{2}\,0\}$	$\{4^+_{001}\|\frac{1}{2}\,0\}$ $\{4^-_{001}\|0\,\frac{1}{2}\}$	$\{\bar{4}^+_{001}\|\frac{1}{2}\,0\}$ $\{\bar{4}^-_{001}\|0\,\frac{1}{2}\}$
M_1	2ω	0	-2	0	0	0	∓ 2	0	0	0
M_2	2ω	0	-2	0	0	0	± 2	0	0	0
M_3	2ω	0	2	0	2	0	0	0	0	0
M_4	2ω	0	2	0	-2	0	0	0	0	0

Table B.2: Character table for $\mathcal{G}_M$; the phase factor $\omega = e^{-iM\cdot\boldsymbol{t}}$ where $M = (\pi\,\pi)$ and $\boldsymbol{t} = (u, v)$.

be the same for every representation of this form. However, when $p+q$ and $r+s$ are both odd we have instead $\psi^{a(-a)c(-c)}(h) = 2(-1)^{q+s}ac$, so the sign of the product ac determines equivalent representations. Taken together, the physically irreducible representations are given by

$$\begin{aligned}\psi^{+--+} = \psi^{-++-} &\equiv M_1\\ \psi^{+-+-} = \psi^{-+-+} &\equiv M_2\\ \psi^{+-++} = \psi^{-+++} &\equiv M_3\\ \psi^{+---} = \psi^{-+--} &\equiv M_4\end{aligned}$$

The labels M_i have been chosen to match with the Bilbao Crystallographic Server. The character table for the physical representations at the M-point is shown in table B.2.

B.3 X-POINT

The little co-group P_X is isomorphic to D_{2h}, but because $P4/nmm$ is non-symmorphic and X lies on the Brillouin zone boundary, we need to identify the elements $\{1|\boldsymbol{t}\}$ for which $e^{iX\cdot\boldsymbol{t}} = 1$. These are all of the translations $(m\,n)$ such that n is even; so T_e is the set of all translations of an even number of lattice vectors along the y-axis. For the remainder of the section, we shall take $G \equiv \mathcal{G}_X/T_e$.

We find that G can be generated by $\{m_{100}|\frac{1}{2}\,0\}$, $\{\bar{1}|0\,0\}$ and $\{m_{010}|0\,\frac{1}{2}\}$, with the generating relations

$$\begin{aligned}&\{m_{100}|\tfrac{1}{2}\,0\}^2 = \{\bar{1}|0\,0\}^2 = \{m_{010}|0\,\tfrac{1}{2}\}^2\\ &= (\{m_{100}|\tfrac{1}{2}\,0\}\{\bar{1}|0\,0\})^2 = (\{m_{100}|\tfrac{1}{2}\,0\}\{m_{010}|0\,\tfrac{1}{2}\})^2 = (\{\bar{1}|0\,0\}\{m_{010}|0\,\tfrac{1}{2}\})^4\end{aligned}$$

We observe then that $G \simeq D_{4h}$ according to the isomorphism defined by $\{m_{100}|\frac{1}{2}\,0\} \to I$, $\{\bar{1}|0\,0\} \to \sigma_Y$ and $\{m_{010}|0\,\frac{1}{2}\} \to \sigma_y$, the characters for which have already been determined. To identify the physical irreducible representations, we note that

$$\{\bar{1}|0\,0\}\{m_{010}|0\,\tfrac{1}{2}\}\{\bar{1}|0\,0\}\{m_{010}|0\,\tfrac{1}{2}\} = \{1|1\,0\}$$

so we need to identify the representations in table A.4 which have $D(C_2) = -\mathbb{1}$, according to the isomorphism defined. These representations are the E_g and E_u representations of D_{4h}, which become the X_1 and X_2 representations on $\mathcal{G}_X$, as shown in table B.3.

$\mathcal{G}_X$	$\{1\|uv\}$	$\{m_{100}\|\frac{1}{2}\,0\}$	$\{m_{010}\|0\,\frac{1}{2}\}$	$\{2_{001}\|\frac{1}{2}\,\frac{1}{2}\}$	$\{\bar{1}\|0\,0\}$	$\{2_{100}\|\frac{1}{2}\,0\}$	$\{2_{010}\|0\,\frac{1}{2}\}$	$\{m_{001}\|\frac{1}{2}\,\frac{1}{2}\}$
X_1	$2e^{-i\pi v}$	2	0	0	0	0	0	0
X_2	$2e^{-i\pi v}$	-2	0	0	0	0	0	0

Table B.3: Character table for $\mathcal{G}_X$

B.4 HIGH-SYMMETRY LINES

The high-symmetry points Γ, M and X are connected by high symmetry lines; the line Σ along $k_x = k_y$ connects Γ to M, the line Δ along $k_x = 0$ connects Γ to X, and the line Y along $k_y = \pi$ connects M to X. These lines have reduced symmetry compared to the high-symmetry points which they connect, and as such we have, for example, $\mathcal{G}_\Sigma \leq \mathcal{G}_\Gamma$, $\mathcal{G}_\Delta \leq \mathcal{G}_\Gamma$, and $\mathcal{G}_Y \leq \mathcal{G}_X$. We can generate the irreducible representations along each line by considering the restriction of the high-symmetry point to the line. Because the Σ and Δ lines are in the interior of the Brillouin zone, we also have to include the additional phase factor $e^{-i\boldsymbol{k}\cdot\boldsymbol{w}}$ for the representations subduced from the Γ-point, but for the Y line, the characters already have this phase factor included.

The procedure of subduction is simple compared to the inverse process of induction. For a given subgroup $H \leq G$ and representation π on G, the subduced representation $\pi \downarrow H$ is found by restricting the domain of π from G to H. As we noted earlier, some irreducible representations on G become reducible when subduced to H, particularly any representation with dimension $d > 1$ if H is abelian. This is in fact the case on both the Σ and Δ lines.

We observe that $\mathcal{G}_\Sigma/T$ consists of only $\{1|0\,0\}$, $\{m_{001}|\frac{1}{2}\,\frac{1}{2}\}$, $\{m_{1\bar{1}0}|0\,0\}$ and $\{2_{110}|\frac{1}{2}\,\frac{1}{2}\}$. Table B.4 shows the characters of $\mathcal{G}_\Sigma$ which result when the characters in table B.1 are restricted to $\mathcal{G}_\Sigma$.

$\mathcal{G}_\Sigma$	$\{1\|uv\}$	$\{m_{001}\|\frac{1}{2}\,\frac{1}{2}\}$	$\{m_{1\bar{1}0}\|0\,0\}$	$\{2_{110}\|\frac{1}{2}\,\frac{1}{2}\}$
Σ_1	$e^{-ik(u+v)}$	e^{-ik}	1	e^{-ik}
Σ_2	$e^{-ik(u+v)}$	e^{-ik}	-1	$-e^{-ik}$
Σ_3	$e^{-ik(u+v)}$	$-e^{-ik}$	1	$-e^{-ik}$
Σ_4	$e^{-ik(u+v)}$	$-e^{-ik}$	-1	e^{-ik}

Table B.4: Character table for $\mathcal{G}_\Sigma$. A point on the Σ line has $\boldsymbol{k} = (k,\, k)$, where $k \in (0, \pi)$ when normalized to lattice units. In lattice units, $u, v \in \mathbb{Z}$.

Similarly, we observe that $\mathcal{G}_\Delta/T$ consists of only $\{1|0\,0\}$, $\{m_{001}|\frac{1}{2}\,\frac{1}{2}\}$, $\{m_{100}|\frac{1}{2}\,0\}$ and $\{2_{010}|0\,\frac{1}{2}\}$. Table B.5 shows the characters of $\mathcal{G}_\Delta$ which result when the characters in table B.1 are restricted to $\mathcal{G}_\Delta$.

$\mathcal{G}_\Delta$	$\{1\|uv\}$	$\{m_{001}\|\frac{1}{2}\,\frac{1}{2}\}$	$\{m_{100}\|\frac{1}{2}\,0\}$	$\{2_{010}\|0\,\frac{1}{2}\}$
Δ_1	e^{-ikv}	e^{-ik}	1	e^{-ik}
Δ_2	e^{-ikv}	$-e^{-ik}$	-1	e^{-ik}
Δ_3	e^{-ikv}	$-e^{-ik}$	1	$-e^{-ik}$
Δ_4	e^{-ikv}	e^{-ik}	-1	$-e^{-ik}$

Table B.5: Character table for $\mathcal{G}_\Delta$. A point on the Δ line has $\boldsymbol{k} = (0,\, k)$, where $k \in (0, \pi)$ when normalized to lattice units. In lattice units, $u, v \in \mathbb{Z}$.

$\mathcal{G}_Y$	$\{1\|uv\}$	$\{m_{001}\|\frac{1}{2}\,\frac{1}{2}\}$	$\{m_{010}\|0\,\frac{1}{2}\}$	$\{2_{100}\|\frac{1}{2}\,0\}$
X_1	$2e^{-i(ku+\pi v)}$	0	0	0
X_2	$2e^{-i(ku+\pi v)}$	0	0	0

Table B.6: Character table for $\mathcal{G}_Y$. A point on the Y line has $\boldsymbol{k} = (k, \pi)$, where $k \in (0, \pi)$ when normalized to lattice units. In lattice units, $u, v \in \mathbb{Z}$.

Finally, for the Y-line, we have $\mathcal{G}_Y/T$ given by the elements $\{1|0\,0\}$, $\{m_{001}|\frac{1}{2}\,\frac{1}{2}\}$, $\{m_{010}|0\,\frac{1}{2}\}$ and $\{2_{100}|\frac{1}{2}\,0\}$. Table B.6 shows the characters of $\mathcal{G}_Y$ which result when the characters in table B.3 are restricted to $\mathcal{G}_Y$; there is only one physical irreducible representation along the Y-line.

Joseph O'Halloran

[redacted]
0000-0001-6612-7838

Education

Bachelor of Arts, Physics & Mathematics — June 2010
Lawrence University, Appleton WI

Publications

D. F. Agterberg, T. Shishidou, P. M. R. Brydon, J. O'Halloran, M. Weinert, "Resilient nodeless d-wave superconductivity in monolayer FeSe" Phys. Rev. Lett. 119, 267001 (2017)

J. O'Halloran, D. F. Agterberg, M. X. Chen, M. Weinert, "Stabilizing the spin vortex crystal phase in two-dimensional iron-based superconductors" Phys. Rev. B **95**, 075104 (2017)

Awards

R1 Distinguished Dissertation Fellowship
David Lichtman Research Fellowship
Graduate Student Excellence Fellowship
Physics Research Excellence [multiple]
Chancellor's Graduate Student Award [multiple]

Conferences and Presentations

National High Magnetic Field Laboratory Theory Winter School — January 2019
Poster Presentation: "Annihilated Nodes and Gap Features of d-Wave Superconductivity in Monolayer FeSe"

Fine Theoretical Physics Institute Summer School — June 2016
Poster Presentation: "Effects of Broken Inversion Symmetry in Monolayer FeSe"

APS March Meeting — March 2016
Submitted Talk: "Effects of inversion symmetry breaking in monolayer FeSe"

International School in Multi-condensates Superconductivity — July 2014
Poster Presentation: "Low Energy Effective Hamiltonian in Iron Based Superconductors Lacking Inversion Symmetry"

Skills

LaTeX ●●●●
Group Theory ●●●●
Pedagogy ●●●
Public Speaking ●●●
C++ ●●
Fortran ●●
Python ●●
MATLAB ●●

Teaching Experience

The Art and Science of Teaching Physics [Lecture]
UWM–Physics 610
Participants critique lectures, videotapes of experienced teachers, each other; address conceptual problems facing beginning students; gain familiarity with demonstrations, classroom technology; discuss their own classes.

Physics for the Health Professions [Discussion Section]
UWM–Physics 110
An introductory course without laboratory for students in health-related pre-professional programs. Topics include mechanics, fluids, heat, sound, electricity, magnetism, electrical devices, optics, and radioactivity.

General Physics I (Non-Calculus Treatment) [Discussion Section]
UWM–Physics 120
Mechanics, wave motion, heat, and sound.

General Physics II (Calculus Treatment) [Discussion Section]
UWM–Physics 210
Electricity, optics, modern physics.

General Physics Laboratory II (Non-Calculus Treatment) [Lab Section]
UWM–Physics 123
Experiments on topics related to the lecture material of General Physics II (Non-Calculus Treatment)—Electricity, optics, modern physics.

Physics Tutor
General tutoring at all levels, including introductory undergraduate, advanced undergraduate, and qualifier preparatory.

Research Interests

My current research interests are in iron-based superconductors. I study tight-binding and $\boldsymbol{k} \cdot \boldsymbol{p}$-like models of iron-selenide, in particular investigating the symmetry of the superconducting order parameter. There is much debate regarding the mechanism driving superconductivity; identifying the symmetry of the order parameter would place constraints on this mechanism. I am working to identify experimental signatures which can discriminate between different symmetries. More generally, I am interested in studying the effects of multiband physics on superconductivity.

Societies and Community Engagement

Sigma Pi Sigma ($\Sigma\Pi\Sigma$)	elected 2009
University Community Orchestra	member since 2013
American Physical Society	member since 2015
St. Francis Historical Society	member since 2017